ROUGH-SURFACE GRAVITY CURRENT FLOWS

by

Wayne D. Peters

B.Sc.E., Mechanical Engineering
University of New Brunswick, 1989

A Thesis Submitted in Partial Fulfilment of the Requirements for the Degree of

Doctor of Philosophy

in the Graduate Academic Unit of Mechanical Engineering

Supervisor:	Dr. J.E.S. Venart, Mechanical Engineering
Examining Board:	Dr. A.C.M. Sousa, Mechanical Engineering Dr. J.H. Thompson, Mathematics and Statistics Dr. T. Pugsley, Chemical Engineering, Chair
External Examiner:	Dr. R.D. Rowe, Department of Mechanical and Marine Engineering, University of Plymouth, UK

THE UNIVERSITY OF NEW BRUNSWICK

April 1999

ABSTRACT

A two-dimensional, full-field, quantitative, visualization technique was developed to assess the flow dynamics and mixing behaviour associated with gravity current heads flowing over rough surfaces. Small-scale saltwater modelling, laser-induced fluorescence and digital image processing were combined in this technique to analyze the effects of surface roughness on the downstream spread and dilution rates of these flows.

This research was completed in three phases: 1) the development of the modelling, visualization and analysis techniques, 2) the validation of these techniques using published results from well-documented, smooth-surface flow studies and 3) the evaluation of how well the published smooth-surface flow theory extends to rough-surface flows in an effort to develop new rough-surface flow models. To this end, the influences of surface roughness scale and source fluid density excess on gravity current flow dynamics and head dilution were examined. The results of this work should have potential contributions to the area of heavier-than-air gas (HTAG) dispersion modelling.

ACKNOWLEDGEMENTS

I would like to formally thank my supervisor, Dr. J.E.S. Venart, for the evaluation, guidance and encouragement that he provided throughout the term of this research. Also, I would like to express my gratitude to Dr. Venart and the Fire Science Centre for the opportunities I have had to participate in other research projects during my involvement with him and the Centre.

It is with sincere appreciation that I gratefully acknowledge the assistance, advice, support and friendship of the following people: Dennis Carr, Vince Boardman, Steven Cogswell, Robert London, Susan Shea, Debbie Basque, Charles Dutcher, Marie Comeau, Ken Colpitts, Richard Heartz and Dr. Ken Sollows.

I would, also, like to acknowledge the financial support received from the following agencies: Natural Sciences and Engineering Research Council of Canada, Emergency Preparedness Canada and the Society of Fire Protection Engineers.

Finally, and most importantly, I would like to thank my best friend and wife, Glenda, for the unwavering love, patience, understanding, encouragement and support that she has given me through these past years. Without her, this thesis would most certainly not have been completed.

TABLE OF CONTENTS

LIST OF FIGURES

NOMENCLATURE

b	path length of excitation signal laser beam, cm
B	gravity current head buoyancy flux fraction, B_H/B_S, non-dimensional
B_S	gravity current source buoyancy flux, $g'_S Q$, cm^3/s^3
B_H	gravity current head buoyancy flux, $g'_H Q$, cm^3/s^3
c	molar concentration of fluorescent dye, mol/l
c_f	friction coefficient, non-dimensional
d	downstream roughness element width, cm
d_R	new characteristic length scale developed for rough-surface flows, $d'_{REF} Re_{EFF}$, cm
d_{REF}	characteristic length scale developed for smooth-surface flows, $(Q^2/g'_S)^{1/3}$, cm
d'_{REF}	characteristic length scale based on the rough-surface reduced gravity term, $(Q^2/g'')^{1/3}$, cm
Fr	Froude number, non-dimensional
g	acceleration due to gravity, cm/s^2
g'_H	reduced gravity term (Boussinesq approximation) based on the head fluid density excess quantified from images, cm/s^2
g'_S	reduced gravity term (Boussinesq approximation) based on the source fluid density excess, cm/s^2
g''	rough-surface reduced gravity term (Boussinesq approximation), cm/s^2
H	source fluid layer height at position, x, measured upwards from y=0, cm
H_S	source fluid layer height near the inlet measured upwards from y=0, cm
H'	source fluid layer height behind the head measured upwards from y=0, cm
h_1	water channel ambient fluid height measured upwards from y=0, cm
h_2	gravity current head height measured upwards from y=0, cm
h_R	roughness element height measured upwards from y=0, cm
I	emission signal strength
I_o	excitation signal strength

k	spread rate constant for the viscous-buoyant flow regime, non-dimensional
k_S	equivalent sand grain roughness, cm
n	downstream viscous-buoyant dilution rate exponent, non-dimensional
Q	continuous source volumetric injection rate per unit channel width, cm^2/s
Q'	volume flux of dense fluid into the head from the source fluid layer, cm^2/s
Re	Reynolds number, non-dimensional
Re_{EFF}	effective rough-surface Reynolds number, non-dimensional
R_1	characteristic length scale used by Chen (1980), $d_{REF}Re$, cm
S	roughness element spacing, mm
t	elapsed gravity current advance time, s
t_R	new characteristic time scale developed for rough-surface flows, $t'_{REF}Re_{EFF}$, s
t_{REF}	characteristic time scale developed for smooth-surface flows, $(Q/g'^2_S)^{1/3}$, s
t'_{REF}	characteristic time scale based on the rough-surface reduced gravity term, $(Q/g''^2)^{1/3}$, s
t_t	inertial-buoyant/viscous-buoyant regime transition time, s
t_1	characteristic time scale used by Chen (1980), $t_{REF}Re$, s
U	mean source fluid layer velocity at downstream position, x, cm/s
U_S	mean source fluid layer velocity near the inlet edge, cm/s
U'	mean source fluid layer velocity immediately behind the head, cm/s
u_2	mean head frontal velocity, cm/s
u_R	new characteristic velocity scale developed for rough-surface flows, u'_{REF}, cm/s
u_{REF}	characteristic velocity scale for smooth-surface flows, $(g'_S Q)^{1/3}$, cm/s
u'_{REF}	characteristic velocity scale based on the rough-surface reduced gravity term, $(g''Q)^{1/3}$, cm/s
w	channel width, cm
X	head frontal position measured from inlet edge, cm
$X_{50\%}$	downstream channel position at which the buoyancy flux fraction falls to 50% of its initial value, cm

$(X_{50\%})_R$	ratio of the rough/smooth-surface channel positions at which the buoyancy flux fraction falls to 50% of its initial value, non-dimensional
x	downstream channel position measured from inlet edge, cm
x_t	inertial-buoyant/viscous-buoyant regime transition position, cm
y	vertical height measured positive upwards with y=0 at smooth channel floor surface, cm
α	buoyancy flux reduction factor for rough-surface flows, non-dimensional
ρ_A	ambient fluid density, g/cm^3
ρ_B	source fluid density, g/cm^3
ρ_H	mean head fluid density, g/cm^3
ρ_L	mean layer fluid density, g/cm^3
$(\Delta\rho/\rho_A)_H$	mean head fluid density excess, $(\rho_H-\rho_A)/\rho_A$, non-dimensional
$(\Delta\rho/\rho_A)_L$	mean layer fluid density excess, $(\rho_L-\rho_A)/\rho_A$, non-dimensional
$(\Delta\rho/\rho_A)_S$	source fluid density excess, $(\rho_B-\rho_A)/\rho_A$, non-dimensional
ρ^*	density parameter used by Gröbelbauer et al (1993), non-dimensional
τ	boundary shear stress, N/m^2
θ_R	observed viscous-buoyant rough-surface mixing ratio, $\theta_R = n_{ROUGH} / n_{SMOOTH}$, non-dimensional
ν_A	ambient fluid kinematic viscosity, cm^2/s
ν_B	source fluid kinematic viscosity, cm^2/s
ν_{EFF}	effective rough-surface viscosity, cm^2/s
ε	molar absorptivity of the fluorescent dye, l/mol-cm
Φ	quantum efficiency of the fluorescent dye, non-dimensional
$(\,)^*$	non-dimensionalized, or normalized, quantity using the appropriate smooth-surface characteristic scaling parameter
$(\,)^{**}$	non-dimensionalized, or normalized, quantity using the appropriate rough-surface characteristic scaling parameter

CHAPTER 1

INTRODUCTION

1.1. Description of a Gravity Current

A gravity current is a flow of one fluid within another of a different density. The flow is driven by the horizontal pressure gradient that arises from the density difference between the two fluids. The resulting buoyancy-induced driving force can be generated by a density difference between the two fluids as little as one per cent or less. This density difference may be due to dissolved or suspended material in one of the fluids, or may be the result of a temperature difference between the two fluids. In colder climates, a common gravity current experience occurs when the door to a warm house is opened. This action allows a current of cold outside air to flow into the house along the floor while warm inside air flows out above this incoming cold layer.

The gravity current flow configuration is governed by the relative magnitudes of the fluid densities as depicted in Figure 1. A fluid discharged into a reservoir of less dense fluid, for example, will slump to the bottom and spread horizontally to produce the most common configuration known as a dense gravity current. Similarly, a free surface flow can be generated in a fluid into which a lighter fluid is released. In another configuration known as an intrusion, the current can be created at the interface between two density-stratified fluids if the current fluid density is of an intermediate value.

The primary feature of a dense gravity current flowing over a smooth surface is a well defined raised head formed at the downstream edge of a shallower flowing source layer. This is illustrated in Figure 2. The leading point of this head exhibits a slightly elevated nose which allows less dense ambient fluid to be overrun by the structure as it advances. Behind the head, a stable and quiescent interface separates the lower source layer from an adjacent layer formed above it. This upper layer consists of an intermediate density fluid formed due to the mixing between the ambient and source fluids within the head.

Very often the fluids that form gravity currents are miscible so that the head region is observed to be a zone of intense mixing. Accordingly, two mechanisms by which ambient fluid is able to penetrate into the head region are identified: 1) interfacial mixing due to shearing along the intruding head/ambient fluid boundary and 2) mixing due to the ingestion of lighter ambient fluid overrun by the head. The result of this mixing is a decrease in the head/ambient fluid density difference and, thus, in the strength of the buoyant driving force.

Natural gravity current examples are plentiful. Characterized by large-scale atmospheric movements of relatively cool air, thunderstorm outflows and sea-breeze fronts exhibit classic gravity current behaviour. Fog banks, consisting of fluidized suspensions and avalanches, created by particulate suspensions of air-borne snow, behave in a similar manner. In the oceans, gravity currents appear as turbidity currents or as salt-water intrusions that travel long distances up fresh-water rivers.

In a man-made world, discharges of waste water and power plant cooling water can significantly alter the rivers and lakes into which they are dumped, as warmer water flows across the surface in the form of a gravity current. Oil, released during an ocean spill, spreads in the form of a gravity current and can result in serious environmental damage. The transport of combustion products along the ceiling of a burning building and the spread of hazardous heavier-than-air gases (HTAG) over land are, also, governed by the gravity current flow phenomenon. The gravity currents present in each of these man-made phenomena are no less significant than nature's examples.

1.2. Brief Overview of Modelling, Visualization and Analysis Techniques

The salt-water modelling technique employed here uses a horizontal channel facility and two density-differentiated miscible fluids to generate small-scale, isothermal, adiabatic gravity current flows. The denser of the two fluids is continuously injected into a channel filled with the lighter fluid. This injection occurs through an entry box located at the bottom of one end of the channel such that the inlet flow has no initial horizontal momentum. The buoyancy-induced driving force that exists between the two fluids leads to a flow of the heavier fluid along the channel floor in the form of a gravity current.

For this work, the density differential between the two working fluids is attained by dissolving a specified amount of sodium chloride in pH-buffered tap water to produce fluids with density differentials up to a maximum of about 18%. The range of fluid density difference used in the present work is within this limit. If a larger fluid density differential is required, the experimenter can choose a more appropriate solute.

Laser-induced fluorescence (LIF) visualization is used in conjunction with the salt-water modelling method described above. This is a non-intrusive visualization technique in which a water-soluble fluorescent dye is used as a flow marker. The dye emits a specific wavelength of visible light when excited by an appropriate wavelength of energy. In this work, fluorescein sodium dye is added to the more dense source fluid and, then, made to fluoresce by passing a sheet of argon ion laser light through the homogeneously mixed dyed fluid.

A known relationship between the dye's fluorescent emission signal strength and its concentration in the fluid allows a quantitative assessment of the density field to be made. The basis of this analysis is that fluorescent intensity acts as a scalar marker for the salt concentration and, thus, the density of the fluid. It is necessary, then, to assume that the mass transport rates of the dye and of the salt are approximately the same.

Mass transport can occur by two methods - molecular diffusion and turbulent mixing. In gravity current flows, however, turbulent mixing is far more significant than any diffusion process that may occur (Steckler et al., 1986). Consequently, it equally governs the transport of both the dye and the salt throughout the gravity current structure. The time scales associated with these flows are much too small for diffusion to be of any consequence.

The resulting two-dimensional planar views of the flow are sampled using video methods to provide images for further study. Digital image processing techniques are used to enhance the images and produce quantitative representations of the flows for comparison and evaluation purposes.

1.3. Background

1.3.1 Gravity Current Flows

Some of the earliest experimental work on gravity current flows was performed by Schmidt (1911) while modelling atmospheric cold fronts. He used water flows with a temperature-induced density difference of up to 1% to create small-scale gravity currents. As viscosity is a function of temperature, Schmidt was able to demonstrate the effect of Reynolds number on the gravity current head profile by varying the temperature of the current fluid. For now, though, the gravity current Reynolds number will be defined as $Re = u_2 h_2/\nu$ where u_2 and h_2 are the gravity current head frontal velocity and head height, respectively, and ν is the kinematic viscosity of the fluid. Schmidt's experimental observations are depicted in Figure 3.

In the first view of this figure, Schmidt estimated the Reynolds number to be about 10. Consequently, viscous forces are significant and very little mixing is apparent in the resulting small current head. As the current fluid temperature and, thus, the Reynolds number, was increased, Schmidt observed that the mixing intensified until a limiting profile, seen in the final view, was reached. For this limiting case, the Reynolds number is somewhat greater than 1000.

Schmidt concluded that the profile illustrated in the last image possesses the turbulent mixing characteristics typical of all flows with a Reynolds number greater than 1000. He further concluded that the head profile and its mixing intensity are, thus, independent of Reynolds number for values greater than about 1000. This was later supported by Keulegan (1949, 1957, 1958) and Simpson and Britter (1979). Field

observations of thunderstorm outflows, with Reynolds numbers approaching 10^6, have shown that the structure and mixing intensity are very similar to those observed in small-scale flows with Reynolds numbers of the order of 1000.

The first mathematical analysis of gravity current motion was performed by von Kármán (1940). Working with a frame of reference attached to the advancing current, he assumed the head to be at rest while the ambient fluid flowed over it with an equal and opposite velocity. Applying Bernoulli's theorem along streamlines on either side of the interface between the current and ambient fluids, he was able to obtain an expression for the mean head frontal velocity given as

$$u_2 = \sqrt{2 g'_S h_2}\,. \qquad (1\text{-}1)$$

Through experiment, von Kármán confirmed the existence of a structured head formation. In his analysis, however, he did not distinguish between the height of the head and that of the upstream source fluid layer. Furthermore, he demonstrated that the current moves with a constant speed and maintains its shape throughout its progression.

To be consistent throughout the present work, the equations reported here have been changed from the original authors' representation to agree with the nomenclature used by the current author and with that depicted in Figure 4. Again, u_2 is the gravity current mean head frontal velocity and h_2 is the gravity current head height. Invoking the Boussinesq approximation, a reduced gravity term for the gravity current flow is defined

as $g'_S=g(\rho_B-\rho_A)/\rho_A$ in which ρ is the fluid density and the subscripts A and B refer to the channel ambient and source fluids, respectively. The $(\rho_B-\rho_A)/\rho_A$ term represents the maximum fluid density excess available or the source fluid density excess.

Gravity current work continued with Keulegan (1949, 1957, 1958) who extensively examined a number of saline advances in lock exchange flows. Recognizing that the advance velocity should be a function of the fluid densities and the flow geometry, he used dimensional analysis to express the head frontal velocity in a form similar to that of von Kármán. It is given as

$$u_2 = C\sqrt{g'_S h_2} \qquad (1\text{-}2)$$

in which the length scale h_2 is the gravity current head height. The constant, C, is the densimetric Froude number, defined as the ratio of inertial to buoyant forces, which can be thought of as the normalized current head frontal velocity. According to von Kármán, this constant has a value of $\sqrt{2}$.

Keulegan's lock exchange flows confirmed that the Froude number, or normalized head frontal velocity, is constant but only for Reynolds numbers above some critical value. However, the value of the Froude number was experimentally determined to be approximately half of that of von Kármán's mathematically predicted value. Based on the head characteristics, Keulegan defined the Froude number and corresponding Reynolds number criteria as

$$Fr = \frac{u_2}{\sqrt{g'_S h_2}} = 0.705 \; ; \; Re = \frac{u_2 h_2}{\nu} > 1200. \qquad (1\text{-}3)$$

This criteria for Reynolds number independence is in general agreement with Schmidt's observations. Alternatively, Equation (1-3) can be given in terms of the fluid layer height immediately behind the head, H', using the ratio h_2/H' which has a value of 2.16, according to Keulegan. In this alternative form, the Froude number and critical Reynolds number were expressed as

$$Fr = \frac{u_2}{\sqrt{g'_S H'}} = 1.04 \; ; \; Re = \frac{u_2 H'}{\nu} > 550. \qquad (1\text{-}4)$$

Benjamin (1968) believed that an energy conservation model was not appropriate for gravity current flows. Consequently, he questioned the validity of von Kármán's use of Bernoulli's theorem to determine the advance velocity of a gravity current. In his work, he observed the movement of an air cavity advancing along the upper surface of a horizontal, water-filled tube as it emptied. Assuming that the gravity current height was small compared to that of the ambient fluid, Benjamin applied an overall force balance within the flow to produce the same results as von Kármán.

He explained that the ambient flow velocity profile could not be uniform with vertical position as the flow near the current must be influenced by the zone of breaking waves behind the head. Although the energy losses in this region could not be specified, he maintained that they were essential and should not be neglected. The only energy conserving case, he pointed out, would be one in which the height of the dense current

was exactly half that of the ambient fluid. Anything less, as in the assumption of deep ambient fluid flows, must result in a dissipative interface such that the Bernoulli theorem approach would be invalid.

Using salt-water lock exchange experiments, Winant and Bratkovich (1977) identified the general flows and mixing regions within a gravity current head and made estimates of the various fluxes in and out of it as indicated in Figure 5. These flux estimates were given as fractions of the total flux, Q_t, flowing in the upstream source layer. They are 1) the regions through which a flux, Q_1, of ambient fluid is entrained into the head, approximately 20%, 2) the flux of dense fluid into the head from the upstream source layer, Q_2, approximately 15%, 3) the upstream flux of dense fluid out of the head at the floor due to the no-slip boundary condition, Q_3, approximately 5% and 4) the flux of mixed fluid out of the head that is left behind it in the region above the source layer, Q_4, approximately 30%.

The estimate of the influx of dense fluid that is supplied to the head from the source layer, Q_2, indicates that the mean velocity in this layer is approximately 15% greater than the frontal velocity of the head. This over-taking condition is necessary to ensure that dense fluid is introduced into the frontal region. Without it, the influx of ambient fluid, Q_1, would quickly dilute the gravity current head.

In addition to these estimates, Winant and Bratkovich observed large density fluctuations within the head region of the gravity current due to the influx of lighter ambient fluid. They noted that these variations seemed to be more a result of gravitational instability between discrete parcels of unmixed fluid rather than any active

turbulent fluctuations. In conclusion, they stated that definitions of the mixing sites and mechanisms are required to fully understand the processes which govern the gravity current flow.

A large amount of work on smooth-surface gravity current flows has been carried out by Simpson (1972, 1986, 1987) and Simpson and Britter (1979, 1980). They extensively studied these flows using two different salt-water modelling approaches: 1) a technique in which the gravity current head is brought to rest by an opposing flow and moving floor and 2) a modified lock exchange flow system. They reported no systematic differences in results derived from either of these methods.

These researchers identified two influx mechanisms which allow lighter ambient fluid to penetrate the head and mix with the influx of dense fluid from the source layer. They are 1) interfacial mixing due to shearing along the intruding head/ambient fluid boundary and 2) mixing due to the ingestion of lighter ambient fluid overrun by the head. Due to the shearing at the interface between the head and ambient fluids, Kelvin-Helmholtz billows are formed which roll up and over the head. The gravitational instability of the lighter overrun fluid contributes to the three-dimensionality of the smaller scale sub-structure of the head (Simpson, 1972, 1986).

These authors concluded that the first of these two mechanisms is the primary mixing process at the front for smooth-surface flows. Their measurements have shown that the height of the overrun lighter ambient fluid layer is about one tenth of the height of the nose of the head. The authors, therefore, concluded that the flux of light fluid flowing under the head is about 1% of the flux of light fluid involved in shear mixing at

the top of the head and, thus, produces only a small fraction of the total mixing. However, this fluid is essential for the generation of the three-dimensional lobe and cleft patterns described by Simpson (1972, 1986).

The apparatus used by Simpson and Britter made it possible to study a gravity current head in near steady-state conditions by bringing it to rest. In this approach, the rate at which dense fluid is mixed out of the current by the lighter ambient fluid penetrating the head was shown to be just the quantity of dense fluid supplied by the source in their experimental apparatus. This inflow of dense fluid is necessary to maintain the steady-state condition in the structure. The mean velocity at which this fluid reaches the head is, thus, the velocity excess, or overtaking velocity, as described by Winant and Bratkovich's work. In agreement, Simpson and Britter's measurements indicate that this overtaking velocity is approximately 15% greater than the head frontal velocity.

Work by authors such as Keulegan (1949, 1957, 1958) and Benjamin (1968) assumed that the head frontal velocity was constant throughout the spread. Later work by Britter (1979), Huppert and Simpson (1980), Chen (1980), Didden and Maxworthy (1982) and Huppert (1982), however, have shown that the horizontal spread of a gravity current over a smooth surface is actually governed by a balance of buoyant, inertial and viscous forces. According to the relative magnitudes of these forces, these later authors showed that two distinct flow regimes are possible.

The first of these regimes, observed to occur during the early stages of a dense gravity current spread, is governed by a balance between the driving gravitational force

of buoyancy and the inertial forces in the flow structure. This is the inertial-buoyant regime and is characterized by a constant head frontal velocity and, thus, a constant Froude number. This condition governs the flow as long as the inertial forces are large compared with the total viscous drag. This is the flow regime that was studied by Keulegan and Benjamin.

As described in the works of these later authors, characteristic smooth-surface length and time scales were established for this flow regime using dimensional analysis techniques. They were determined to be $d_{REF}=(Q^2/g'_S)^{1/3}$ and $t_{REF}=(Q/g'^2_S)^{1/3}$ for length and time, respectively. From these, the velocity scale was defined as $u_{REF}=(g'_S Q)^{1/3}$. In these scales, Q is the source volumetric injection rate per unit channel width. The product of g'_S and Q is the source buoyancy flux, B_S. For these scales, the reduced gravity term is based on the source fluid density excess, $(\Delta\rho/\rho_A)_S$.

Resulting from the balance between the buoyant and inertial forces, a constant velocity, constant Froude number, spread rate equation for the inertial-buoyant regime can be formed such that

$$X = C\,(g'_S Q)^{1/3}\,t. \qquad (1\text{-}5)$$

In this form, C is the Froude number, or normalized head frontal velocity, u_2^*, non-dimensionalized using the characteristic velocity scale, u_{REF}. Experiments by Chobotov et al. (1987) put this constant in the range 0.75 - 0.85 while Chan et al. (1993) report a value of 0.89.

Note that Equation (1-5) is a function of g'_s and Q which are experimentally controlled and accurately measured in the present work. Their product, (g'_sQ), quantifies the buoyant source strength, or buoyancy flux, which quantifies the source condition. Early authors, such as Keulegan and Benjamin, defined the spread rate as a function of a measured length scale such as the source fluid layer height or the current head height. Scaling relative to these parameters, however, can present some difficulties as they 1) are not experimentally controlled, 2) are difficult to measure and 3) can vary with downstream position and time.

Development of the relations presented by authors such as Didden and Maxworthy (1982) was based on an assumption that the net mass flux of dense fluid out of the head is negligible. In other words, mixing between the head and ambient fluids was assumed to be non-existent. Consequently, the mean fluid density excess of the head is constant throughout the spread. This may be a reasonable approximation for the smooth-surface flows for which the relations were developed but it is much less appropriate for flows over rougher surfaces where significant mixing and head dilution occurs (Peters et al., 1996, 1997).

In the second of the two identified flow regimes, the shear stress developed at the current/ambient fluid interface plus that generated at the lower solid boundary produces viscous forces that become larger than the inertial forces. Under this new condition, viscous drag becomes the dominant retarding force to the flow and a second flow regime - the viscous-buoyant regime - is established.

In this regime, the head frontal velocity and, thus, the Froude number are observed to decrease as the flow progresses down the channel. Here, the spread rate equation is given by

$$X = k\left(\frac{g'_S Q^3}{\nu}\right)^{1/5} t^{4/5} . \qquad (1\text{-}6)$$

Note the dependence on the fluid kinematic viscosity. The spread rate constant, k, was determined experimentally by Didden and Maxworthy (1982) to be 0.73. Huppert (1982) proposed a theoretical value of 0.804. As in the inertial-buoyant flow regime, Equation (1-6) was not developed for flows over rough surfaces.

The work presented, thus far, describes gravity currents that are characterized by the Boussinesq flow model in which the reduced gravity term is used. The assumption is that the density difference between the working fluids and the density fluctuations in the flow are very small compared to the density of either fluid in the system. For gravity current flows with large density differences, such as those that can be generated in the early stages of HTAG dispersions, the use of a reduced gravity term is not necessarily appropriate. The suitability of Boussinesq modelling for dense HTAG flows will be discussed in a later section.

In response to this, Gröbelbauer et al. (1993) experimentally simulated high density ratio, non-Boussinesq fronts using different density gases. They experimented in a closed channel lock-exchange apparatus and, with appropriate gas selection, were able to model fronts with large current/ambient fluid density ratios. At the upper limit of

their work, for example, a combination of R22 and Helium was used to give a density ratio of 21.6. This translates to a heavy gas density approximately 2000% greater than the light gas density. In contrast, von Kármán's Boussinesq flows had density differences of less than 1%.

To account for such large density differences, these authors used an alternative scaling technique in which the Froude number and density difference were considered separately. They used the same Froude number definition as Keulegan and Benjamin, except that the full-scale value of the gravity term is used rather than a reduced value. Their definition of a non-dimensional density parameter was based on the interpretation by Yih (1965) that the frontal velocity relation should reflect the inertia of both fluids. It was defined as

$$\rho^* = \sqrt{\frac{(\rho_B - \rho_A)}{(\rho_B + \rho_A)}}. \qquad (1\text{-}7)$$

This parameter was found to be finite over the entire range of fluid density differences found in both Boussinesq and non-Boussinesq flows. For Boussinesq flows ($\rho_A \sim \rho_B$), the value of this parameter approaches zero.

Gröbelbauer et al. correlated the Froude number, or normalized frontal advance velocity, with their normalized density parameter. Their experimental data falls on two distinct curves - one for dense gas fronts moving along a rigid floor and another for light gas fronts moving along a rigid ceiling. As expected, the curves coincide for the low density difference Boussinesq flows and diverge significantly for large density difference

non-Boussinesq flows. This divergence occurs at about $\rho^* = 0.3$ which coincides with a 20 % fluid density difference. It is also marked by a difference in frontal shape - the light fluid front is elongated and generally loss free while the dense fluid front has a blunt shape and exhibits more evidence of mixing.

1.3.2. Laser-Induced Fluorescence

Fluorescent dyes have been available for some time. The use of laser-induced fluorescence (LIF) for flow visualization, however, has only increased with the ability to easily generate thin sheets of laser light. In many instances, LIF can provide significantly more valuable information about the anatomy of a fluid flow than can be acquired with conventional dye methods. This non-intrusive dye technique provides a researcher with a simple and convenient flow marking scheme for measuring scalar quantities within a flow.

An extensive review of the theories of luminescence and fluorescence is given by Guilbault (1973) who points out that these measurement techniques, first used as early as 1565, are among the oldest and most established analytical methods available. For dilute dye solutions, he indicates that the fluorescent emission signal strength is linearly proportional to dye concentration according to

$$I = K\Phi I_o \varepsilon b c \qquad (1\text{-}8)$$

where I is the fluorescent emission signal strength, K is an experimental coefficient, Φ is the quantum efficiency, I_o is the excitation signal strength, ε is the molar absorptivity, b is the path length of the excitation signal laser beam and c is the molar concentration of the fluorescent dye.

For low dye concentrations, this linear response is typically maintained over a wide range of dye concentration until the quantity of dye is large enough to absorb significant amounts of light from the excitation signal. According to Guilbault, it is necessary that the dyed solution absorb less than 5% of the excitation signal to maintain this linear relation. In addition to linearity, Guilbault notes that the attenuation of the excitation signal as it passes through the dyed solution is, typically, observed to be negligible for low dye concentrations.

Walker (1987) performed an extensive examination of the behaviour of the fluorescent dye, fluorescein sodium, and indicates that its maximum dye concentration, below which a full-range, linear response is maintained, is typically 10^{-7} mol/l or 0.04 mg/l. In his work, he considered the variation of the emission signal strength with temperature, pH, concentration and excitation signal strength and shows that great care must be taken to achieve valid results with dyes of this type. Under controlled conditions, however, fluorescein sodium makes a good choice for LIF techniques. The use of this dye in the present work will be discussed in more detail in a later section.

In his overview of visualization techniques, Gad-el-Hak (1988) describes his use of LIF in the study of boundary layer growth. He states that any plane in the flow is readily viewed, producing a picture of the interior flow structure rather than just the outer

boundaries as with conventional dye methods. Hesselink (1988) reports that LIF is a very useful tool in combustion research, providing accurate species concentration, as well as, density and temperature information about combustion flows.

Many research applications exist in which fluorescent dyes are employed to visualize and quantify a particular flow feature. Mixing in a full-scale exhaust gas stack was studied by Peters and Venart (1992). Using LIF, small-scale stack gas flows were visualized to infer the planar temperature profile within the stack. Sollows et al. (1990) used this technique to visualize velocity profiles in transient free convective flows in cavities. Velocities were measured by tracking time-line and time-streak markers generated in the flow using laser photo-bleaching.

Mapping of species concentration, density or temperature in a planar field, or along a line, is the most frequently cited use of the LIF technique. Examples in the literature are abundant. Karasso and Mungal (1997), Houcine et al. (1996), Yoda and Fiedler (1996), Nash et al. (1995), van Cruyningen et al. (1990) and Shlien (1988) give descriptions of their uses of this method to obtain instantaneous planar concentration profiles in various flow systems. Brungart et al. (1991), Westblom and Svanberg (1985) and Koochesfahani and Dimotakis (1985) describe similar uses of LIF for one-dimensional measurements along a line.

1.3.3. Heavier-Than-Air Gas Dispersion

Understanding the behaviour of heavier-than-air gas (HTAG) dispersions is becoming increasingly more important due to the growing world use of hazardous

materials whose atmospheric releases generate such events. Accidental releases of liquefied petroleum and natural gases (LPG and LNG), for instance, can lead to catastrophic explosions and fires. In 1988, total world trade in these materials was 69 million tonnes, increasing at about 9% annually (Sumathipala et al., 1992). Other materials of concern are flammable gases such as propane, butane and cyclohexane and toxic gases such as chlorine.

Work by Britter and Griffiths (1982) outlines the relevance of research in this area and discusses, from a safety point of view, the detrimental implications of these types of dispersions. They state that the focus for hazard assessment should be in the quantification of damage potential at various locations within the release vicinity. Accordingly, the assessment of concentration levels within the HTAG cloud, and when these levels fall below the safe limits for flammability or toxicity, for instance, must be assigned high priority.

In the case of flammable gases, evaluation of the probability for ignition and explosion, if a source is encountered, demands a knowledge of the spatial and temporal variability of the cloud concentration. Mean estimates do not give a complete picture of the cloud as they can be far exceeded by localized concentration values. More importantly, it is necessary to know whether peak concentrations occur in localized pockets or in continuous regions that, perhaps, stretch back to the ignition source.

Due to the occurrence of a number of disastrous hazardous gas releases (Lenoir and Davenport, 1992), many countries have introduced legislation requiring that these hazards be assessed. In his review of dense gas dispersion research, McQuaid (1982)

addresses this topic with special emphasis on the information required to make reasonable predictions of the risks involved. He states that a thorough understanding of the consequences of these accidents depends on HTAG dispersion research.

McQuaid points out that a large number of predictive methods exist for HTAG dispersion behaviour. He emphasizes, however, that they all rely on a relatively small collection of experimental data from which empirical information can be drawn. Consequently, these models fail to provide reliable predictions when used to describe scenarios not subject to experimental validation. McQuaid concludes, therefore, that it is extremely necessary to generate a body of experimental data to facilitate model validation.

Considerable research has been, and continues to be, performed in the area of HTAG dispersion. Typically, this work follows one of three approaches: 1) wind-tunnel simulations, 2) small- and large-scale field experiments and 3) development of numerical predictive models. Accordingly, it is necessary to have a key understanding of the main features of each.

Reviewing HTAG wind-tunnel research, Meroney (1982) notes that reasonable empirical predictions for full-scale dispersions can be achieved as long as model limitations are recognized and respected. Quite often, however, rigorous similarity between the model and full-scale flows cannot be achieved for all the relevant variables. In these situations, it is concluded that partial similarity may be sufficient as long as the neglected variables have little influence on the flow.

Scaling of both the Reynolds and Froude numbers presents the most difficult similarity problem for HTAG simulations. Hoot and Meroney (1974) have shown, however, that the Froude number governs cloud characteristics such as spread rate, size and entrainment. Hence, proper scaling of this parameter, in addition to the density ratio and buoyancy flux, is most important. Scaling will be further discussed in a later section.

Results of small- and large-scale field simulations of HTAG dispersions provide a much needed reliable database for validating predictive theories. A detailed review of field releases of LNG was compiled by Puttock et al. (1982) in which comparisons were made of the scale of each test and the degree to which density effects influenced the dispersion. The primary effects of density were observed to be the gravitationally dominated spread of the flow and the suppression of vertical mixing by the sharp vertical density gradient formed.

Field test results are interpreted using one of three scaling approaches. First, field-scale flows are considered to be analogous to their full-scale counterparts such that results are transformed using the Froude number. Second, mathematical models are developed based on physical principles requiring field experiments to test their validity. In a third, but less likely, approach, the size of the field test may be on the same scale as some supposed accident such that scaling is not a concern.

Mathematical models of dense gas dispersion behaviour can be classified into two general types: K-theory models and slab models. The first of these, also known as an eddy diffusivity model, relies on a numerical integration of simplified equations of

mass, momentum and energy conservation. It assumes that mass transfer occurs by eddy diffusion and is proportional to concentration gradients. In the slab, or top-hat, model, the cloud is assumed to have a fixed shape with mass transfer occurring by entrainment across the cloud/air density interface.

Blackmore et al. (1982) evaluated fifteen such models and outlined the simplifying assumptions common to each. These include 1) the dispersion is over flat terrain or water, 2) the cloud is not obstructed, 3) no chemical reactions occur and 4) local concentration fluctuations are not predicted. In addition to these, slab models assume that concentration is uniform throughout the cloud. According to these authors, these simplifications limit the reliability of mathematical models to simple and experimentally validated dispersion scenarios. They conclude that more rigorous experimental programs are required to support model extrapolation to more complex dispersion cases.

In addition to spatial and temporal predictions of cloud width, height and concentration, these same authors (Blackmore et al., 1982) state that a useful parameter for these models is the downstream distance at which the cloud is no longer a hazard. For dispersions of flammable gases, for instance, this position is typically taken to be the distance to the lower flammability limit (LFL). Some models go even further and base this distance on the concentration associated with half of this limit, yielding distance predictions as much as 50% greater.

In the past, numerous studies of dispersions over flat terrain have broadened our knowledge of the subject. More recently, however, focus has been on the dynamics of

flows over more complicated surfaces. Specifically, consideration has been given to the behaviour of flows that encounter single obstructions with a dimensional scale on the order of that of the dispersing cloud. Few literature examples, though, were found by this author in which flows over more intermediate scale, homogeneous roughness arrays were considered.

Rottman et al. (1985), for example, considered dispersions in which surface mounted obstacles, including a solid fence, a porous fence and a cube, were encountered. They developed simple theoretical models for the dense lower layer flow in these two-layer flow systems based on shallow-water approximations. Their simple analytical models were supported experimentally with results from salt-water modelling.

They observed that reasonable predictions were made with their two-dimensional hydraulic theories for cloud impacts with a solid wall with a height similar to that of the cloud. Results were in general agreement with observations from the Thorney Island Phase II field trials (Davies and Singh, 1985). Upon impact, the bulk of the heavy fluid was seen to surmount the fence and form a gravity current on the downstream side with a hydraulic jump propagating back upstream. More recently, work by Lane-Serff et al. (1995) agreed with these results, indicating that a wall approximately twice the gravity current height would be required to completely block the flow.

Using wind tunnel techniques, Ayrault et al. (1993) considered flow interaction with solid fences placed across the dense gas flow. They noted that cloud dilution is significantly dependent on the ratio of the fence height to the undisturbed cloud height. It was observed that for large ratios, the cloud dilution downstream of the fence is due to

the intense turbulence in the fence wake. For a ratio of less than about 0.5, only a small reduction in the ground level concentrations were measured downstream.

Duijm et al. (1995) developed an integral type dispersion model which describes the effects of three-dimensional obstacles on the downwind cloud spread. When compared with wind tunnel test data, this model was shown to provide reasonable predictions of the peak concentrations that occur on the leeward side of the obstacle. Havens et al. (1995) used a wind tunnel facility to study the dispersion of a dense gas cloud released from a diked tank storage facility. Their experiments indicated that the presence of the tanks and dike promotes a strong bifurcation and enhanced dilution of the cloud downwind of the release.

Britter and Snyder (1988) assessed the influence of simple terrain on dense gas dispersion using wind tunnel experiments. They studied the behaviour of the cloud as it moved up a 14° ramp and, then, along an elevated plateau, approximately one quarter the height of the approaching cloud. They concluded that ground-level concentrations were reduced by only 30-40% due to the effects of the ramp. Little dilution at the ramp base was observed to occur as most occurred as the cloud moved up the incline. The primary effect of the ramp was to change the velocity field in which the cloud developed rather than to directly enhance mixing.

As previously noted, few literature examples of dispersion over smaller scale, homogeneous roughness arrays, similar to those used in this work, were found by this author. Work carried out for the American Petroleum Institute by Petersen (1987), however, has identified much of the progress and research need in this area. His review

of current literature outlines the available experimental databases for rough-surface flows. He cites work by Davies and Singh (1985), Krogstad and Pettersen (1986), Guldemond (1986) and Neff and Meroney (1986). These works, however, deal primarily with flows over obstructions, such as fences and buildings.

The focus of the American Petroleum Institute's work was on dispersions over the large scale roughness typical of processing, handling and storage facilities, including tank farms. Petersen concluded that entrainment relations for these types of flows are generally not available. Since the dispersion behaviour for these situations is very site specific, he stated that similarity theories would not provide appropriate models, and, thus, more research is needed in this area.

For surface roughness small in size compared to that of the cloud, Petersen reports that for the initial dispersion stages when gravitational forces dominate the flow, the effects of roughness are, typically, neglected by similarity models such as DEGADIS (Havens and Spicer, 1985) and SLAB (Ermak and Chan, 1985). Entrainment relations used by these models to describe dispersion behaviour in this negatively-buoyant region are, generally, quantified by the product of a constant and the cloud frontal velocity (Meroney, 1985, 1986). These relations have, thus far, been reasonably well tested. Petersen, however, pointed out that the constant is assumed to be independent of surface roughness - a claim which had not been substantiated.

If surface roughness effects are considered in the early negatively-buoyant dispersion phase, the effect of the generated turbulence should be to decrease the predicted time and distance at which the cloud dispersion is no longer fully governed by

buoyancy. At that point, ambient wind conditions begin to influence the flow, rapidly reducing the cloud/ambient fluid density difference to insignificant levels. Further dispersion is, then, dominated by passive diffusion due to atmospheric turbulence.

For these later flow stages, models like DEGADIS and SLAB base predictions of entrainment, and, thus, dispersion, on estimates of the friction velocity - the square root of the surface stress divided by the fluid density. This parameter can be evaluated as a function of the surface roughness scale and the atmospheric stability using boundary-layer similarity theory. The main assumption here, however, is that the roughness scale is very small compared to that of the cloud; hence, this approach would not be appropriate for larger scale surface roughness.

Petersen compared the results predicted by these two models for neutrally- and negatively-buoyant flows over surfaces of two different roughness scales, i.e., initial cloud height/roughness height ratio of approximately 2 and 30, respectively. Reasonably similar cloud heights were predicted over a downstream distance approximately one hundred times the initial cloud height. For a cloud/ambient fluid density ratio of two, the predicted cloud height increased by only 60% over this distance with the smaller roughness scale while the cloud grew by as much as 350% over the same distance for the larger roughness scale. Beyond this distance, however, the results diverged significantly for the larger scale roughness scenario.

Based on Petersen's work, as previously described, Petersen and Ratcliff (1989) completed a second phase of study for the American Petroleum Institute using wind tunnel techniques. Flows over homogeneous (uniform) and heterogeneous

(non-uniform) surface roughness patterns were modelled using initial cloud/ambient fluid density ratios of 1, 1.4 and 4. Concentrations were measured over a full-scale downwind range of 300 - 800 m for releases initiated from point, small area and large area sources.

The full-scale roughness scales simulated in the uniform roughness cases ranged from that of a grassy plain to that of an urban area with up to four story buildings. The roughness scales used in the non-uniform tests were representative of those found in typical refinery tank farms and processing facilities. This work was intended to increase the understanding of HTAG dispersions and to provide an extensive database for the testing, refinement and validation of numerical models, specifically DEGADIS and SLAB.

General results reported by Petersen and Ratcliff show that downstream cloud dilution can be greatly enhanced by increasing the surface roughness size. Using concentration values measured for a release over a grassy plain as a reference case, it was observed that downwind cloud concentrations were 2 to 6 times less over an urban area, 8 to 25 times less downwind of a processing facility in an urban area and 3 to 8 times less downwind of a tank farm located in an urban area.

Attempting to validate typical dispersion models, Roberts et al. (1990) further considered the data of Petersen and Ratcliff (1989). They concluded that available integral models for dense gas dispersion flows are limited to dispersions over grasslands, or water, and do not provide reasonable results for flows over surfaces with larger scale roughness. This further justifies experimental research aimed at providing

new databases for model development and increasing our understanding of dispersions over a wider range of roughness scales.

1.4. Objectives of this Study

Recent years have witnessed growing environmental and safety related concerns relative to accidental releases of heavier-than-air gases - flammable, toxic, or radioactive. A release of a gas whose density under normal atmospheric conditions is greater than that of the ambient air can result in a dense gas dispersion. As the released material is more dense than the surrounding air, it remains close to the ground where it is a threat to people, structures and the environment.

The catastrophic failure of a vessel used to store this type of material, for instance, can lead to a very rapid release and vapourization of its contents (Venart et al., 1992), while a continuous release from a pressurized system, such as a pipeline, will produce a momentum dominated jet (Fauske and Epstein, 1989). In either case, after the initial effects of the release diminish, the cloud of dense gas eventually slumps to the ground under the influence of gravity and spreads as a gravity current. During this subsequent spread, the effects of surrounding structures and terrain on the dispersion process become significant.

It is of interest to determine the time-dependent concentration profile of this dense cloud as it spreads away from the source so that risk to persons and/or structures can be evaluated. During the release and dispersion process, the cloud is continually diluted with ambient air, reducing its concentration. It is important, therefore, to

understand this dilution process so that accurate estimates of the cloud concentration relative to position and time can be made.

The dilution process is complex and affected by many variables. As the cloud spreads, the wind-generated turbulence of the ambient flow and the turbulence generated by the velocity gradients at the boundaries of the moving cloud induce further mixing. At this stage, also, the roughness of the surrounding terrain and its scale relative to the size of the release will have a significant influence on the process.

Considerable past effort in dense gas dispersion has been directed toward the development of empirical relations used to predict the dilution and advance of the vapour cloud. Unfortunately, this empirical approach has not addressed a description of the fundamental phenomena. This lack of detailed attention toward understanding dispersion behaviour through analysis of basic principles is evident in that the models, thus far, require significant empirical input.

Heavier-than-air gas dispersion is influenced by a multitude of parameters which limit empirical model prediction to very simple situations. Although a great number of these models exist, many of them do not accurately predict cloud behaviour over complex terrain such as forests or structures (Britter and Griffiths, 1982). The influence of terrain leads to areas of local concentration peaks that cannot be reasonably anticipated since much of the data used to develop empirical relations is obtained through large scale gas releases over flat terrain or water. Also, the natural variation of turbulent mixing and cloud meandering leads to cloud concentrations that are unpredictable by the vast majority of models (Wilson, 1991). Therefore, it is necessary

to understand spread behaviour in more detail so that more basic descriptions of the dilution processes can be developed.

Although a significant body of research has been carried out over the years with respect to two-dimensional gravity current flows, very little work has focused on the specific problem of flows over homogeneous roughness patterns. Indeed, no salt-water modelling work in this area has been found by this author. An understanding of the influence of surface roughness on the flow dynamics and mixing mechanisms associated with a gravity current is essential for accurate dispersion modelling and effective mitigation of subsequent damage potential.

Basic small-scale channel experiments will be described in an effort to quantitatively evaluate the mixing mechanisms in gravity current flows over two-dimensional beam-roughened surfaces. Based on the salt-water modelling and laser-induced fluorescence techniques described briefly in Section 1.2 and, in further detail, in Chapter 2, experiments will be described that will provide full-field quantitative information about the mixing behaviour in gravity current flows over rough surfaces.

It is anticipated that lighter ambient fluid can become trapped in the spaces between roughness elements as the current head advances over them. Packets of this buoyantly unstable fluid are then available to be entrained into the advancing current head leading to increased mixing, decreased mean head densities and reduced frontal advance rates.

Special attention, then, will be focused on the mechanism of dilution that occurs at the interface between the current and its lower boundary. It is in this region that

surface roughness can greatly increase the amount of mixing that occurs internally to the gravity current head structure. Flows over different roughness arrays, then, will be assessed in order to determine the influence of roughness element scale and spacing on the overall dilution process.

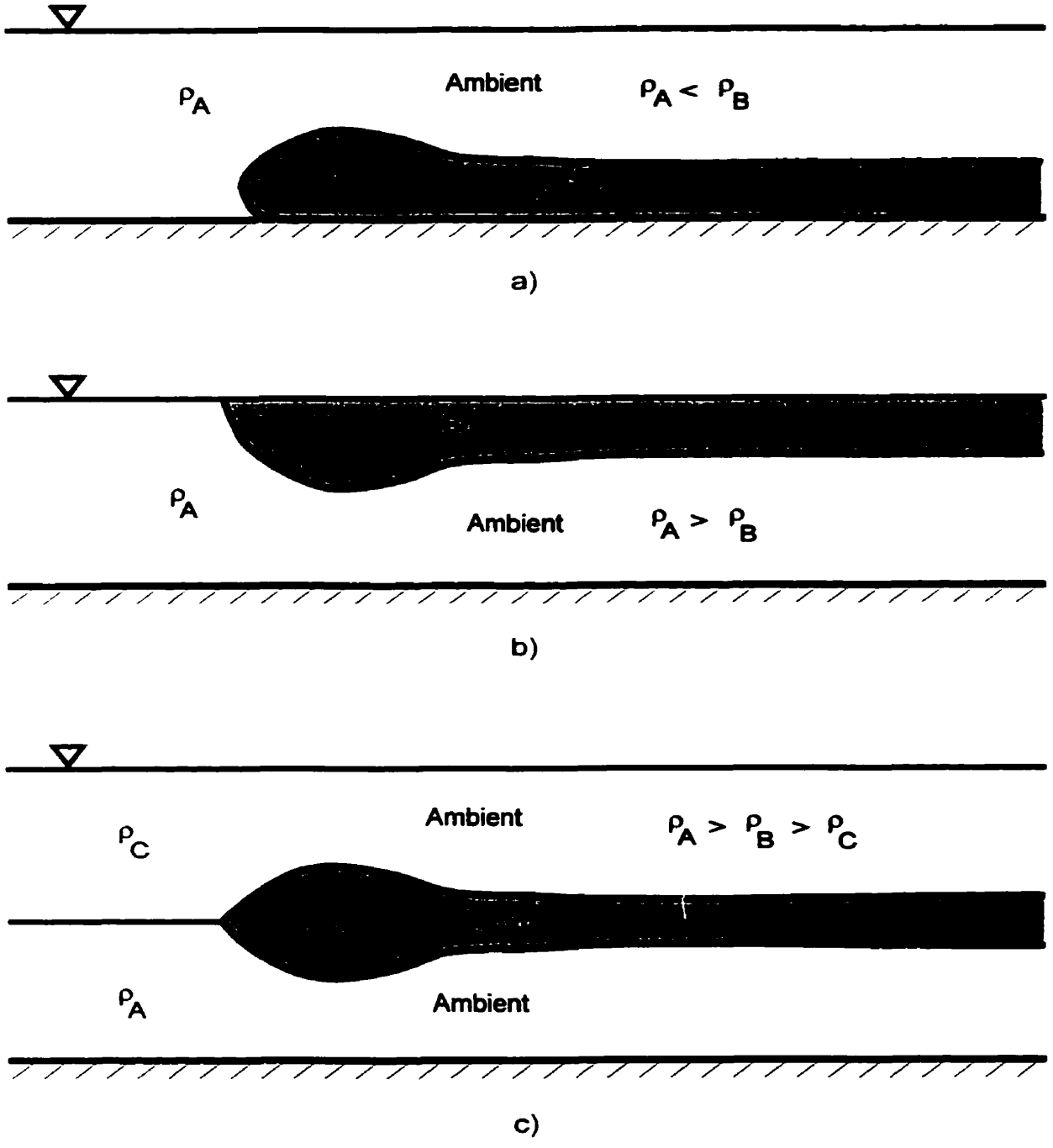

Figure 1. Gravity current flows with current source fluid density a) greater than the ambient fluid density, b) less than the ambient fluid density and c) intermediate to the stratified ambient fluid densities.

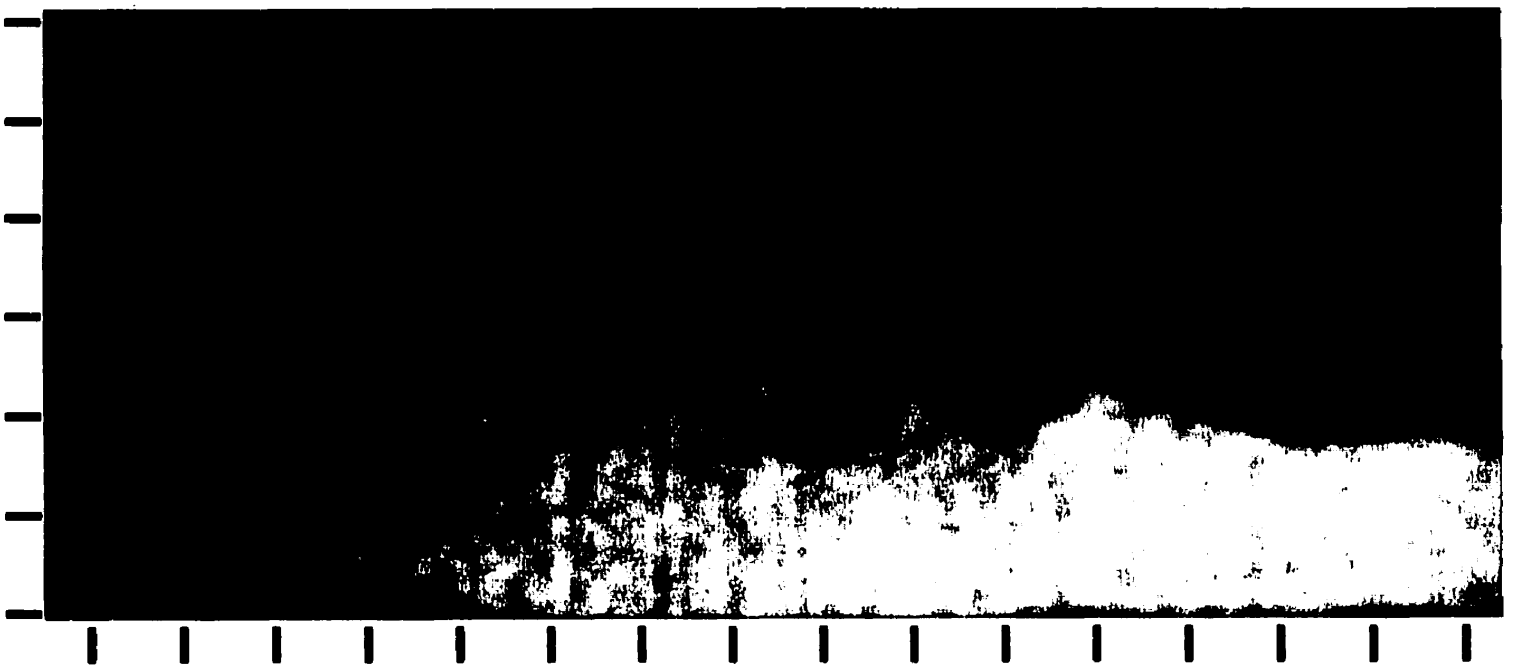

Figure 2. A typical gravity current image which shows the head advancing over a smooth surface to the left and highlights the well defined frontal structure and stable upstream source fluid layer. Source fluid density excess = 0.01. (Scales are divided in 1 cm increments.)

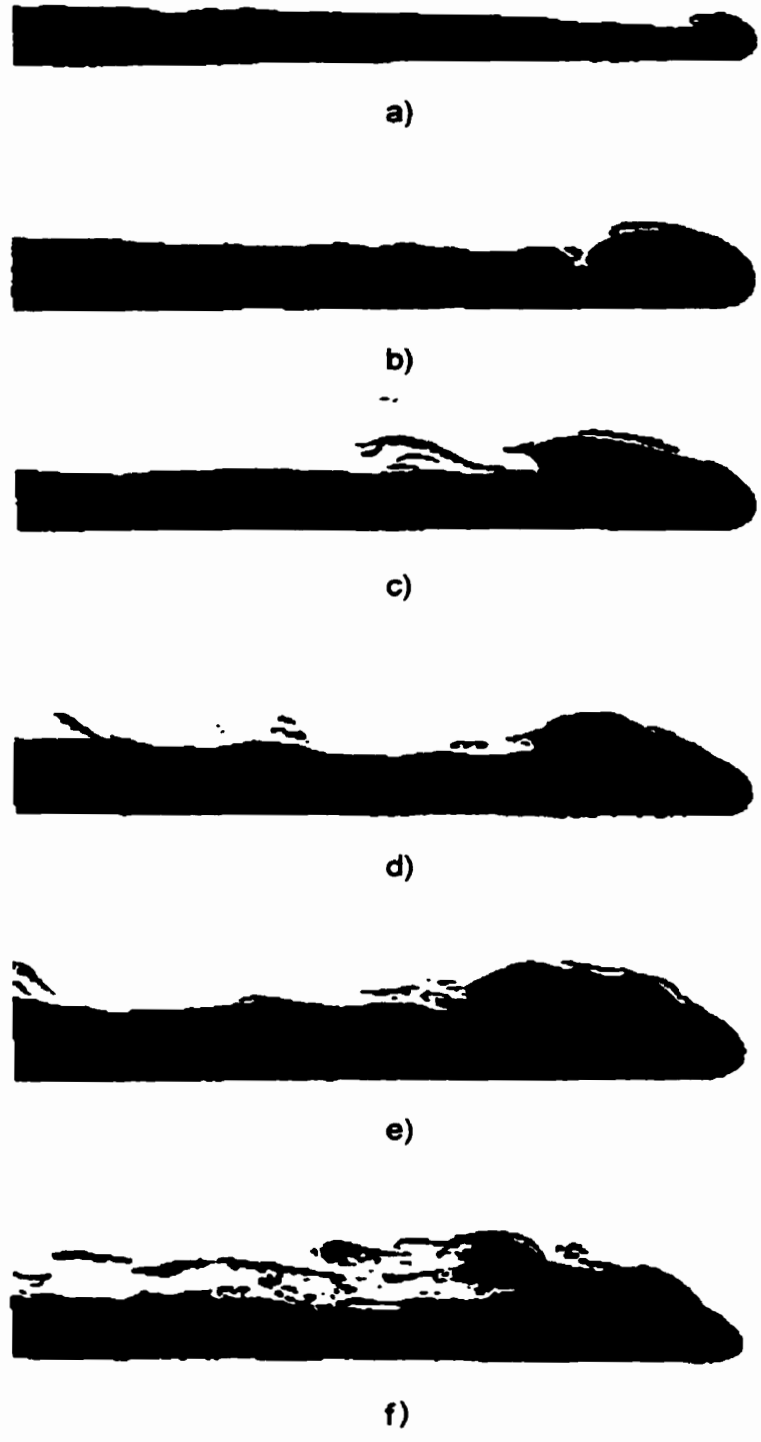

Figure 3. Gravity current head profiles as taken from Schmidt (1911) for Reynolds numbers from less than 10 in a) to somewhat more than 1000 in f).

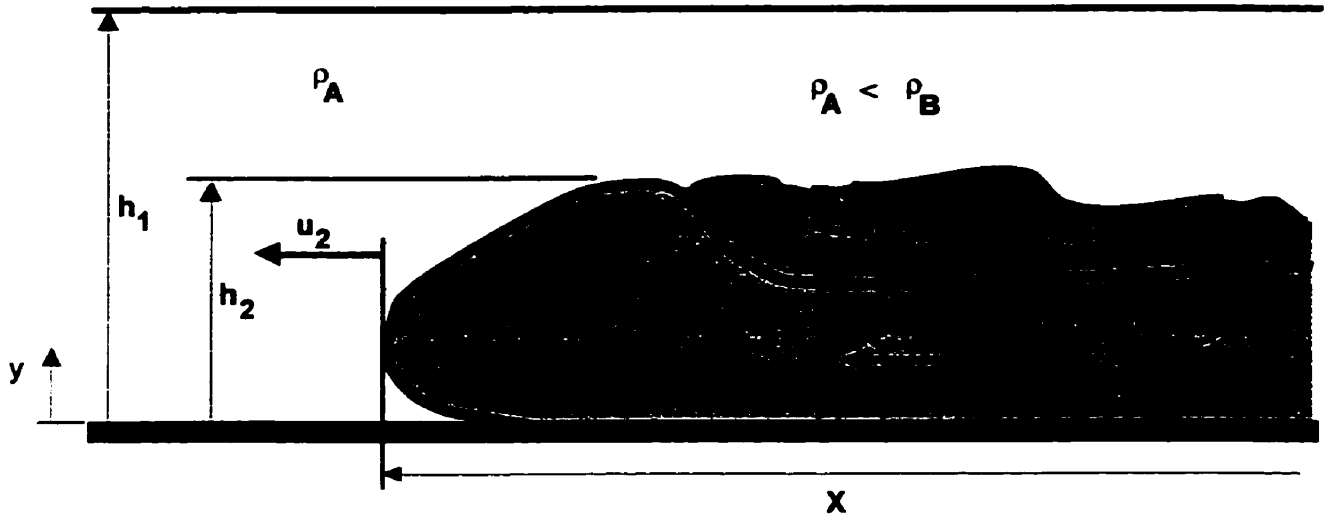

H'	source fluid layer height behind the head
h_1	water channel ambient fluid height
h_2	gravity current head height
Q	continuous source volumetric injection rate per unit channel width
U'	mean source fluid layer velocity immediately behind the head
u_2	mean head frontal velocity
X	head frontal position measured from inlet edge
ρ_A	ambient fluid density
ρ_B	source fluid density
y	vertical height coordinate

Figure 4. Gravity current flow parameters.

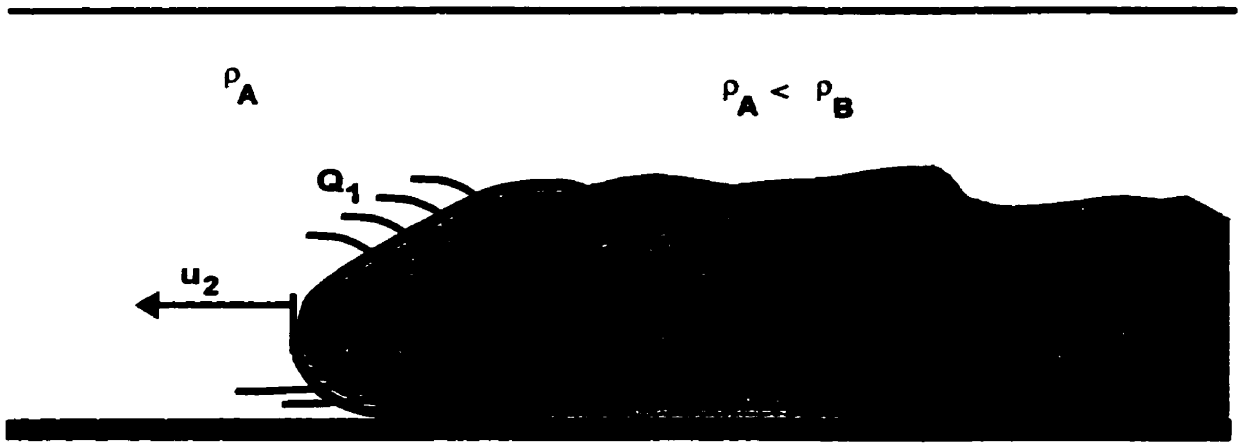

Figure 5. General flows and mixing regions within the gravity current head, as identified by Winant and Bratkovich (1977), indicating 1) the flux of ambient fluid into the head, Q_1, 2) the flux of dense fluid into the head from the upstream source layer, Q_2, 3) the upstream flux of dense fluid out of the head at the floor due to the no-slip boundary condition, Q_3, and 4) the flux of mixed fluid out of the head that is left behind it in the region above the source layer, Q_4.

CHAPTER 2

EXPERIMENTAL FACILITY

Salt-water modelling, laser-induced fluorescence and digital image processing were combined to model, visualize and analyze small-scale, two-dimensional, continuous source gravity current flows. The resulting experimental facility can provide full-field, two-dimensional, planar images of the flow structure for qualitative and quantitative study. For descriptive purposes, the facility is divided into the following six systems: 1) the flow channel system, 2) the circulation system, 3) the flow illumination system, 4) the image acquisition system, 5) the channel traversing system and 6) the image processing system.

2.1. Flow Channel System

Figure 6 schematically illustrates the flow channel system.

2.1.1. Water Channel

The water channel facility consists of an open plexiglass channel, 240 cm long and 20 cm wide with a maximum possible channel fluid height of 30 cm. Saline fluid enters the channel through an entry box section, 20 cm x 20 cm x 20 cm, located on the channel bottom at the upstream end. Before entering the entry box, the fluid passes through a large diameter inlet tube, reducing its velocity by a factor of 6. The entry box is

filled with short sections of plastic pipe designed to promote a uniform velocity profile in the vertical entry flow. The saline fluid is injected vertically into the channel in this manner to ensure that no initial streamwise momentum is imparted to the gravity current flow. Additionally, with this method, a hydraulic jump does not form near the inlet so that the subsequent sub-critical flow is free of the strong turbulent entrainment associated with hydraulic jumps.

The height of the lighter channel ambient fluid is controlled by means of an adjustable overflow weir, located at the upstream end of the channel. As the more dense saline source fluid is injected into the entry box, ambient fluid is displaced over the weir. A horizontal splitter plate is fixed to the weir door, slightly below the spill edge, to separate the region of incoming dense fluid from that of the lighter overflowing fluid.

The channel floor and end wall are painted with a flat black paint to eliminate reflections from these surfaces. The side walls are transparent to allow optical access to the channel. Except for three cross-braces, full optical access is maintained through the top of the open channel.

2.1.2. Surface Roughness

Square cross-section beams, fabricated from acrylic sheet and painted with flat black paint, are used for the roughness elements. A surface roughness configuration consists of a two-dimensional array of these beams positioned on the channel floor, normal to the flow direction. The beams span the full channel width while the array extends over the full channel length. The first roughness element is positioned flush with

the channel inlet edge. A two-dimensional configuration was chosen to minimize any three-dimensional, bulk motions in the flow.

Roughness elements are pinned to acrylic base plates which are, then, positioned on the channel floor. The downstream roughness element width can be varied by positioning elements adjacent to each other; the roughness element height can be changed by stacking them. In addition to these parameters, the downstream spacing between roughness elements can be varied.

For the present work, however, square elements with nominal side dimensions of 6, 13, 19 and 25 mm were used. These roughness element scales were chosen based on gravity current head heights and source fluid layer heights observed in preliminary smooth-surface flow tests over the range of source fluid density excesses tested. These were found to be approximately 50 mm and 25 mm, respectively, yielding a head height/source fluid layer height ratio of approximately 2. This is in close agreement with the value of 2.16 proposed by Keulegan (1949, 1957, 1958). The roughness element heights, then, represent fractional values of the source fluid layer height of approximately 1, 3/4, 1/2 and 1/4.

Figure 7 illustrates the placement pattern for these elements and defines the parameters of roughness element height, h_R, width, d, and spacing, S. In all tests, single beams were positioned with a downstream pitch, S/d, of 2. Including a smooth floor, five surface roughness patterns were examined.

2.2. Circulation System

Figure 6 schematically illustrates the circulation system.

2.2.1. Working Fluids

Typically, a two-fluid system of fresh/saline or saline/saline fluids is prepared using tap water. The less dense of the two fluids is used as the channel ambient fluid while the more dense fluid forms the gravity current fluid. A commercial water softener salt (sodium chloride) is dissolved in one or both of the fluids to provide the required salinity difference. For the present experiments, source fluid density excesses of 0.01, 0.03 and 0.05 (1%, 3% and 5%) were used. Over this range of fluid density excess, the increase in the kinematic viscosity of the fluid is assumed to be negligible. To facilitate the laser-induced fluorescence technique, it was necessary to buffer both fluids to a pH above 8. This requirement will be discussed in more detail in a later section.

2.2.2. Fluid Preparation and Injection System

Saline solutions are prepared in 200 litre mixing/storage tanks by continuous circulation through a closed loop system which is isolated from the channel apparatus as depicted in Figure 6. Salt, in pellet form, is dissolved in a perforated bucket suspended in the solution. Circulation continues until the desired salinity is achieved and the solution is homogeneously mixed. If required, the pH buffering agent and/or the fluorescent dye are added during this circulation. An in-line filter removes any particles from the fluid.

The less dense channel ambient fluid is prepared first and pumped into the channel to the level set by the overflow weir. The channel is, then, isolated from the circulating system so that the more dense saline source fluid containing the fluorescent dye can be prepared as described above. When this is complete and the channel ambient fluid has become quiescent, the heavier fluid is slowly injected into the entry box, displacing the lighter fluid over the weir. This is done slowly enough to minimize mixing between the two fluids. When the saline source fluid level reaches the level of the channel floor, the injection is stopped and the fluids are allowed to become quiescent.

Two variable area flow meters (low range, 2-19 l/s and high range, 17-65 l/s), arranged in a parallel configuration, are used to control the source fluid injection rate, Q, for the experiment. Saline injection is started by simultaneously opening the injection valve to the channel entry box and closing the system recirculation valve.

2.3. Flow Illumination System

The flow illumination system is shown schematically in Figure 8.

2.3.1. Laser and Fibre Optics

The laser beam used in the flow visualization system is generated by a Coherent Innova 70-4 argon ion laser. It has a rated power output of 4 W in the multi-line mode. In the single-line mode, the rated power output is 1.7 W for the green-line wavelength (515nm) and 1.3 W for the blue-line wavelength (488nm). For the laser-induced

fluorescence method used in these experiments, the laser is operated in the single-line mode with the blue-line wavelength (488nm).

The argon ion laser is combined with a fibre optic cable and probe assembly which conveys the laser beam to the flow illumination system. Dantec 60X FibreFlow series of fibre optics is used for this purpose. As a stand-alone system, it represents a very compact, stable and efficient method of beam transmission with the advantage of speed of installation and alignment. Typically, once the fibre optic system has been mounted on the laser table and aligned, further adjustment is not required.

2.3.2. Laser Sheet Generating System

The laser sheet generating system is located above the flow channel. The single blue line beam provided by the fibre optic cable and probe is reflected off a rotating front-surface mirror which rotates at a speed of 30,000 rpm. Consequently, the beam sweeps through the visualization section at a frequency of 500 Hz appearing to the naked eye as a two-dimensional sheet of laser light.

Next, the resulting radially diverging laser sheet is passed through a large plano-cylindrical lens (162 mm radius and 74 mm centre thickness) to generate a vertically collimated light sheet. Ideally, this light sheet would have a uniform horizontal intensity profile but, due to imperfections in the collimating lens, the actual profile contains vertical bands of reduced intensity. A correction routine, which will be described later, is applied to images during digital image processing to compensate for this condition.

Before the laser sheet is passed through the longitudinal vertical mid-plane of the channel visualization section, it is passed through two vertically separated thin slits to block out any unwanted reflections and scattered light from the excitation sheet. The final vertical light sheet is approximately 20 cm wide in the streamwise direction and 1.5 mm thick. Due to losses incurred at the rotating mirror and the collimating lens, the power of the scanning beam in the sheet is significantly less than that of the blue line beam provided by the probe.

2.3.3. Fluorescent Dye

Fluorescein sodium was selected for use in the LIF visualization technique used here to provide quantitative measurements of the planar concentration profile in the gravity current head structure. With a quantum efficiency of approximately 90% (Guibault, 1973), this dye's peak absorption wavelength of about 490 nm is well matched to the 488 nm excitation wavelength provided by the argon ion laser blue line. There is a sufficiently large separation between this absorption peak and that of the emission spectrum (515 nm) so that much of the excitation signal can be filtered out by the image sampling optics without significantly reducing the emission signal.

In addition to these important characteristics, fluorescein sodium has other advantages over other commercially available dyes such as the rhodamines. It is highly soluble in water and has a very weak dependence on temperature, shown by Walker (1987) to be approximately 0.3% per °C. For the rhodamine dyes, which are known carcinogens, this dependence can be as much as 5% per °C (Guilbault, 1973).

To facilitate quantitative interpretation of fluid density excess profiles, it is necessary that the fluorescent dye concentration and excitation signal strength be low enough to produce the desired dye behaviour. For proper interpretation of results, it is essential that 1) the dye emission signal strength be linearly proportional to both the dye concentration and the excitation signal strength and 2) the attenuation of the excitation signal be negligible as it passes through the dyed solution. According to Walker (1987), these conditions are typically satisfied if the maximum dye concentration used is below approximately 10^{-7} mol/l or 0.04 mg/l for an excitation signal laser beam path length of approximately 10 cm.

Using the visualization technique described in this work, a series of tests were performed to determine the optimum dye concentration and excitation signal strength required to satisfy the above conditions. The strength of the dye emission signal for a homogeneously mixed dyed solution was measured over a range of dye concentrations and excitation signal strengths. The results are summarized in the following two graphs.

In the first of these, Figure 9, the measured dye emission signal strength is given as a function of dye concentration for a range of excitation signal strengths. In the second one, Figure 10, the emission signal strength is shown as a function of the excitation signal strength for a range of dye concentrations. Based on the results of these two figures, the first of the conditions described above was satisfied by using a maximum fluorescein sodium dye concentration of 5×10^{-8} mol/l or 0.020 mg/l and a normalized excitation signal strength of 0.6 for all visualization experiments.

It is also necessary that the choice of dye concentration and excitation signal strength satisfy the second of the two conditions noted. For the values chosen, Figure 11 shows a typical single-line, vertical profile of the dye emission signal measured in a homogeneously dyed solution with a layer height of 10 cm. This figure indicates that attenuation is negligible along the excitation signal path. As further assurance that attenuation will be minimized, the excitation signal path length in the gravity current visualization experiments is typically much less than 10 cm.

The emission signal strength of fluorescein sodium is strongly dependent on solution pH in the range from about 3 to 8. Walker (1987) shows that a 50% decrease in emission signal strength is observed for a drop in pH from about 8 to 6.5. Above a pH of 8, however, the emission signal strength is observed to be maximized and independent of solution pH. Hence, all working fluids were buffered with sodium hydroxide to a pH above 8.

In addition to each of the previous influences, fluorescein sodium is subject to two effects that can produce a gradual decrease in the strength of the emission signal with time - oxidation and photo-decomposition (Guilbault, 1973). Oxidation is a chemical reaction fuelled by oxygen dissolved in the working fluids while photo-decomposition results from exposure of the dyed solutions to the excitation signal, as well as, other light sources. It is necessary, therefore, to address these effects before quantitative concentration measurements can be made.

During these experiments, no direct attempt was made to remove dissolved oxygen from the working fluids but it was observed that some oxygen would leave the

solution as it warmed to room temperature. Additionally, exposure to the excitation signal is a necessary part of the measurement technique that cannot be avoided. Consequently, experiments were performed to quantify the reduction in emission signal strength caused by each of these effects. These experiments were performed in the water channel with a 10 cm layer of solution buffered to a pH above 8 and homogeneously dyed at a concentration of 0.02 mg/l.

Figure 12 shows the results of tracking the emission signal strength over a six hour period during which the solution was not exposed to any light except during one minute periods when measurements of the emission signal strength were taken. Under these conditions, reduction in the emission signal strength is primarily due to oxidation. After about 200 minutes, the signal is observed to stabilize at a level about 77% of the initial emission signal strength. Based on these results, it was concluded that aged dye solutions should be used to ensure that the time-dependent effect of oxidation is avoided.

Following the six-hour oxidation experiment just described, the same aged solution was, then, used in a second experiment to quantify the effects of photo-decomposition. The solution was continuously exposed to a sheet of laser light at a fixed position in the water channel for a period of 25 minutes. Note that this time period is significantly longer that the one minute or less duration of a typical gravity current visualization experiment. Figure 13 shows that photo-decomposition is negligible for this time period and the measured signal is found to be stable at the level observed at the end of the previous oxidation experiment.

It is concluded that residual motion in the solution during this second test continuously replaces the dye in the laser sheet excitation region with fresh unexposed dye. Within the gravity current structure, the turbulent nature of the flow will amplify this effect such that dye particles have very short exposure times and photo-decomposition becomes insignificant. To further eliminate the chance of photo-decomposition, dyed solutions are protected from light at all times and experiments are performed in a dark room.

2.4. Image Acquisition System

The image acquisition system is depicted in Figure 8.

2.4.1. Image Filtering and Intensification

As the video recording system is sensitive to light over a wide bandwidth, it is necessary to ensure that only the wavelength associated with the dye emission spectrum is measured. Firstly, experiments are performed in a dark room to eliminate all background light, leaving only those wavelengths associated with the dye excitation and emission spectrums. Secondly, a sharp cut-off, high-pass, Schott colour filter (Ealing OG-515) with 0% transmission at the excitation wavelength (490 nm) and 63% transmission at the emission wavelength (515 nm) is used to eliminate the excitation signal from the sampled signal.

Since dye emission signal strengths are relatively low, a low-light level image intensifier (Astrolight 9100) is used to amplify the signal about four orders of magnitude.

The intensifier is equipped with a fixed 25 mm TV lens (F2.8 aperture) which samples with a resolution of 32 line-pairs per mm on average over the 25 mm intensifier array. The amplified image is displayed on a phosphor screen where it can be viewed with the naked eye or recorded with a video camera.

2.4.2. Video Camera and Recorder

Experiments are sampled in real-time at a rate of 30 images/second using a B/W CCD video camera (Panasonic WV BD-400) coupled to the phosphor display of the image intensifier. The camera has a pixel resolution of 768 x 493 and is equipped with an 18 mm lens set at full-open aperture. Since the excitation laser beam is scanned through the visualization section at a rate (500 Hz) much greater than that of sampling (30 Hz), it appears as a two-dimensional light sheet to the camera. A S-VHS video cassette recorder (Panasonic AG-6720) is used to record the images for future processing and analysis. An external time signal encoder (For-A VTG-22) is used to superimpose a reference time signal on the recorded video signal.

2.5. Channel Traversing System

2.5.1. Traversing Carriage

The flow illumination and image acquisition systems are mounted on a traversing carriage that can be moved along the channel length. The carriage is mounted on four linear bearings that slide along two 13 mm diameter shafts located above each side of

the channel, extending the full channel length. A computer-controlled stepper motor is mounted on the carriage to provide drive power to the traversing system.

Drive power is transmitted by a no-slip, notched belt to a 250 mm long, 25 mm diameter shaft mounted below the carriage. A continuous spiral groove is machined on this shaft from one end to the other in which a 1.0 mm diameter plastic-coated stainless steel cable is wound. The free ends of this cable are fixed to the tank ends. As the shaft is turned by the motor, the cable winds on one end of the shaft and off at the other end to move the carriage. With this system, carriage position and speed can be measured to an accuracy of ±0.5%.

The rotating mirror system used to scan the laser beam through the visualization section of the channel is mounted on a two-dimensional positioning mechanism fixed to the carriage. The image intensifier and video camera hang from rails mounted on the carriage that extend out over the side of the channel. The vertical position of the intensifier/camera combination and its distance from the flow channel can be adjusted. The carriage is counter-weighted on the back side of the channel to balance the weight of the intensifier/camera apparatus.

2.5.2. Carriage Control

Visualization of the gravity current head structure as it moves down the channel requires that the current head be closely tracked by the traversing system at all times. This is facilitated by the use of a computer program developed to provide accurate control of the carriage acceleration, deceleration, speed and direction. While tracking

the motion of the gravity current head, the user monitors the position of the head with the video system and interactively alters the carriage speed to keep the head steady within the visualization region. Although the feedback path for this control system is through the user, accurate tracking of the gravity current head is effectively maintained. Carriage position, speed and time data are stored in a file that is time-synchronized with the video record.

2.6. Image Processing System

The image processing system is composed of 1) a playback and a record video cassette recorder, 2) a frame grabbing board for image processing, 3) a video/VGA overlay board and 4) a VGA-to-video converter. A 486-based computer is used to support the system and control the video cassette recorders via RS-232 serial ports. A schematic of this system is given in Figure 14. Custom and commercial software packages are used for system control and acquisition of video images that are stored for later processing and analysis.

2.6.1. Hardware, Software and Image Analysis

The playback VCR (NEC PC-VCR PV-S98A) is used to feed composite video directly from the video camera, or from previously recorded video, into the frame grabbing board (Matrox MVP-AT/NP) in real time. This is the first level of image processing, referred to as on-line processing. At this time, the video signal is digitized at 30 frames per second at a resolution of 512 x 480 pixels. In this process, image intensity

is mapped to 256 discrete grey-levels ranging from black to white whereby each pixel is assigned an intensity value based on its relative intensity in the image.

The digitized image is then passed through an input look-up-table, or video mask, so that two mathematical operations can be applied. Firstly, low-level noise is removed by rejecting, or setting to black, all pixels with an intensity less than an established value. Secondly, image offset and gain are optimized using a linear scaling technique to spread the available image intensity range over as much of the 256 level range as possible. The resulting image has a reduced noise level and much greater contrast. If desired, pseudo-colour can be added to the grey-scale image at this time by assigning a colour to a particular pixel intensity or intensity range.

The output of the frame grabbing board can be viewed on an RGB monitor or passed to the video/VGA overlay board (IEV ProMotion VGA Digital Video Windows). This board works in conjunction with the computer's resident super-VGA video board to allow VGA graphics or text to be overlaid on the RGB video signal provided by the frame grabbing board. At this point, any video output that can be generated in a 640 x 480 resolution graphics mode can be added to the video recording and output as a VGA signal.

This VGA signal is passed to a VGA-to-video converter that outputs the signal in various formats; VGA, RGB, S-video and composite video. The VGA output goes to the system's VGA monitor where it can be displayed in a standard Windows environment. The composite video signal is fed to the record VCR (NEC PC-VCR PV-S98A) for S-VHS recording and archiving for the post-processing to follow.

The video record that results from the on-line processing just described is, then, input back into the system via the playback VCR for the second level of image enhancement. This is referred to as post-processing and does not occur in real time. At this level, individual frames are captured from the video and stored to disk. This capture can be performed in one of two ways; 1) as an instantaneous snap-shot of the flow with a 1/30 of a second sampling interval or 2) as a single image representing the time-average of a series of consecutive video frames. Frame averaging will be further discussed later.

During post-processing, more extensive processing techniques can be applied to enhance the images. As mentioned in Section 2.3.2, the excitation sheet does not possess a uniform horizontal intensity profile as desired. It was necessary, therefore, to develop a software routine that could be used to correct for this condition.

First, an image of the uncorrected intensity profile across the sheet is grabbed by sampling a reference image of homogeneously mixed and dyed fluid from the visualization section. A mathematical transformation is, then, generated by horizontally scanning this image to determine the maximum pixel intensity in each column. Each of these maxima are compared to the overall maximum pixel intensity in the image to produce a correction factor for each column. The resulting column correction factors are applied to subsequent images in a horizontal scan so that column intensity is increased in a manner that preserves the ratio of maximum to minimum intensity for that column. Figure 15 shows horizontal profiles before and after correction.

After the previously described image correction is applied, a 3x3 neighbourhood averaging technique can be performed to smooth the signal and eliminate some of the noise inherent in the image recording system. In this routine, the intensity of each pixel is set to average value of the intensities of each of its eight neighbours. Figure 16 shows images of a gravity current before and after each of these image enhancement techniques have been applied.

If not already performed in the on-line processing stage, pseudo-colour can be added to the images at this point. One further step in the post-processing scheme is to extract contours of constant intensity, or density, from the image. In this technique, the number and intensity of the desired contours are specified for the image intensity range. Contours are extracted and can be plotted as 2-D contour maps or 3-D density surfaces.

A spatial mean head fluid density excess can be estimated from this spatial density information. This is achieved by first calculating the volume under the 3-D gravity current head density excess surface using discretized sampling with a resolution of approximately 0.5x0.5 cm. Then, the mean head fluid density excess is determined by dividing this volume by the area of the head that is projected onto the concentration map. In a sense, this is the density excess that the head would possess if it was fully mixed. In addition to mean head density excess values, peak values and spatial standard deviation about the mean can be determined.

As previously mentioned, time-averaged images can be acquired during the post-processing process. In this step, consecutive frames are sampled at a rate of 30

frames/second to produce a single representative averaged image for that sampling period. The effect of increasing the time-averaging period is illustrated in Figure 17.

The relatively small time-scale features of the flow, such as the billows and eddies seen in Figure 17(a), can not be appreciated when the averaging period is increased as seen in Figure 17(c). The results presented in Figure 18, however, indicate that an increased sampling period significantly reduces the spatial standard deviation in the signal emission strength measurements of a homogeneously mixed dyed solution without reducing the overall mean image intensity level. Based on these results, a one second time-averaging period (30 frames) is used for acquisition of time-averaged images.

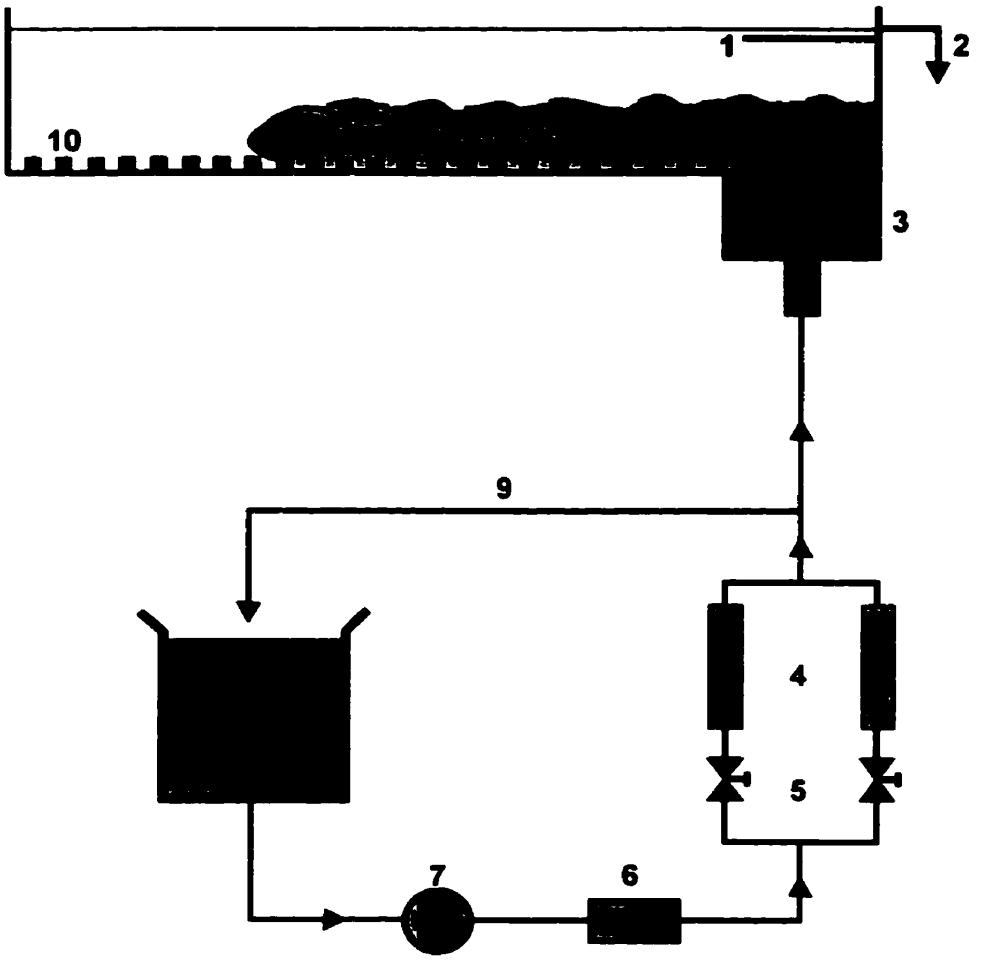

1. splitter plate
2. overflow weir
3. inlet entry box
4. flow meters
5. flow control valves
6. filter
7. circulating pump
8. saline storage reservoir
9. recirculation line
10. roughness array

Figure 6. Schematic diagram of the flow channel and circulation systems used to generate small-scale gravity current flows.

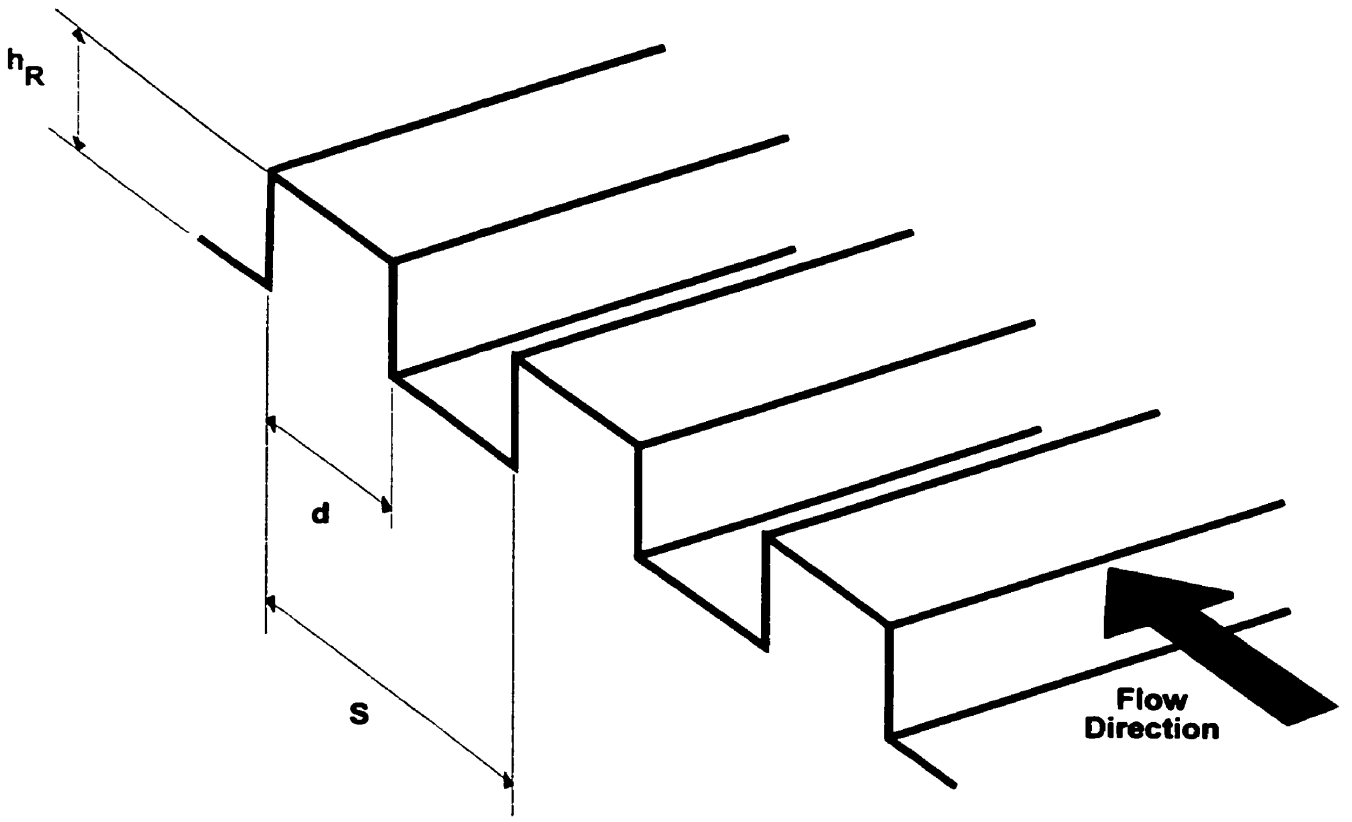

Figure 7. Schematic diagram of the roughness element array configuration showing the roughness element height, h_R, width, d, and spacing, S.

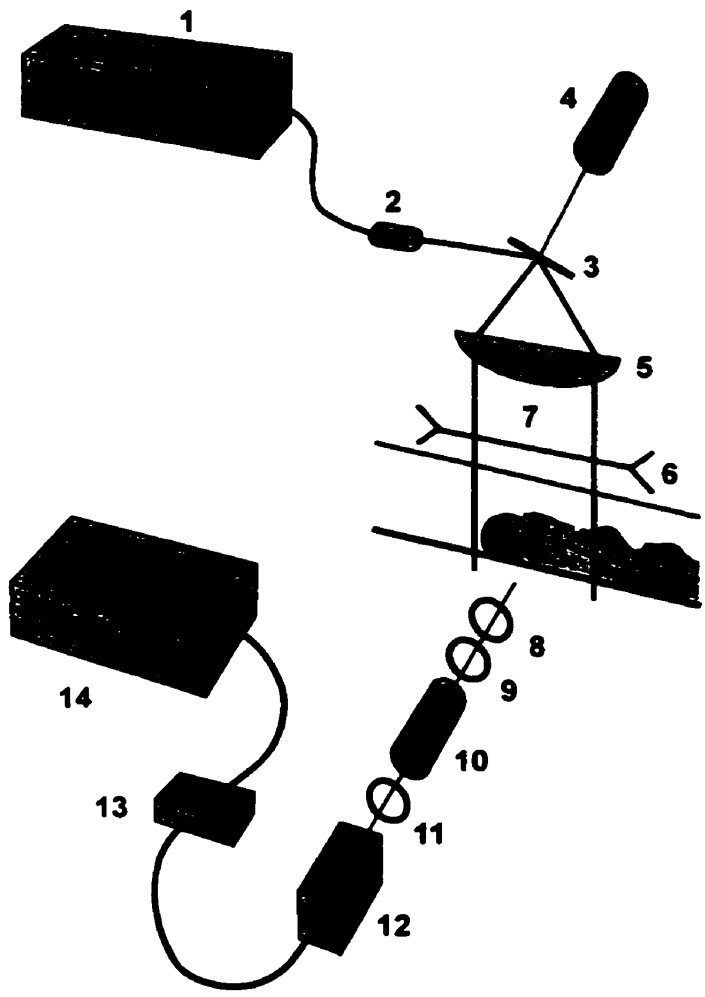

1. argon ion laser
2. fibre optics
3. scanning mirror
4. drive motor
5. collimating lens
6. slit assembly
7. excitation sheet
8. high-pass colour filter
9. 25 mm lens
10. image intensifier
11. 18 mm lens
12. video camera
13. time signal encoder
14. video recorder

Figure 8. Schematic diagram of the flow illumination and image acquisition systems used to visualize the small-scale gravity current flows.

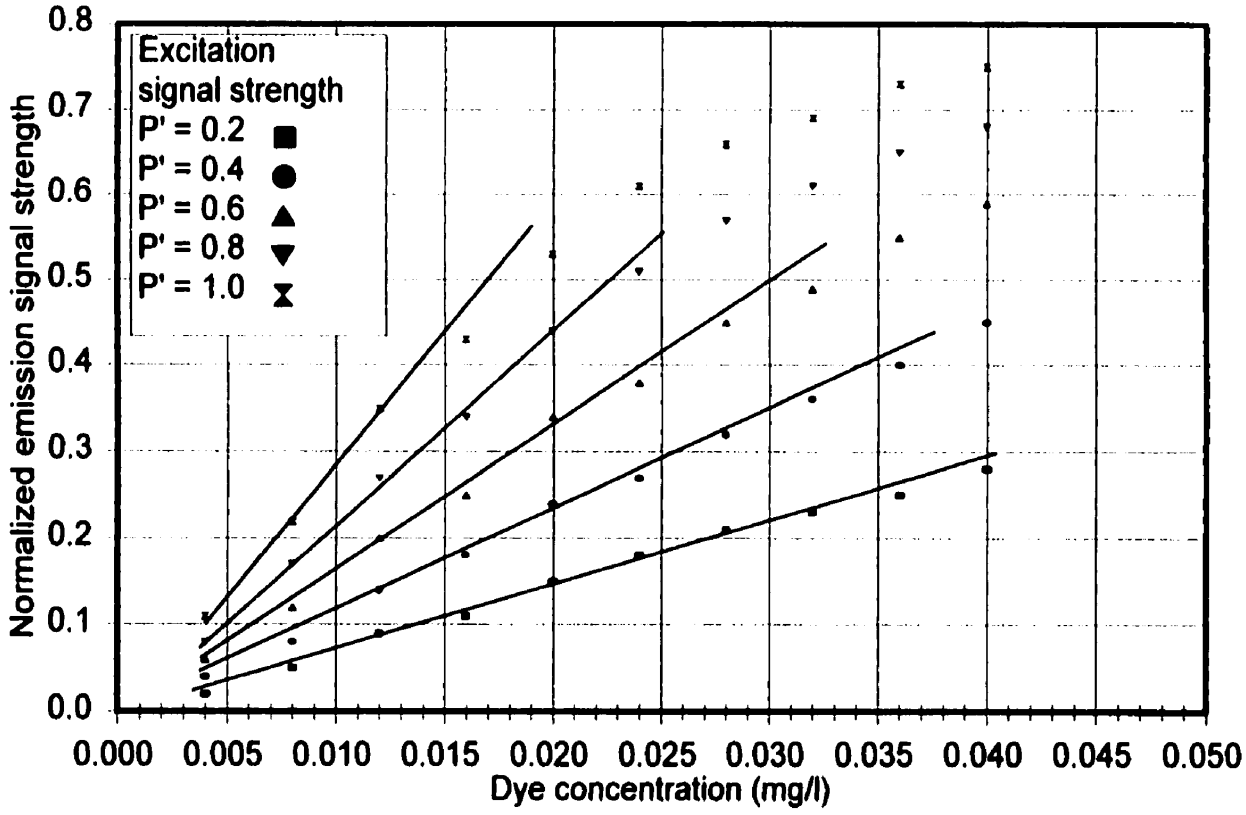

Figure 9. Behaviour of dye emission signal strength with dye concentration for various excitation signal strengths.

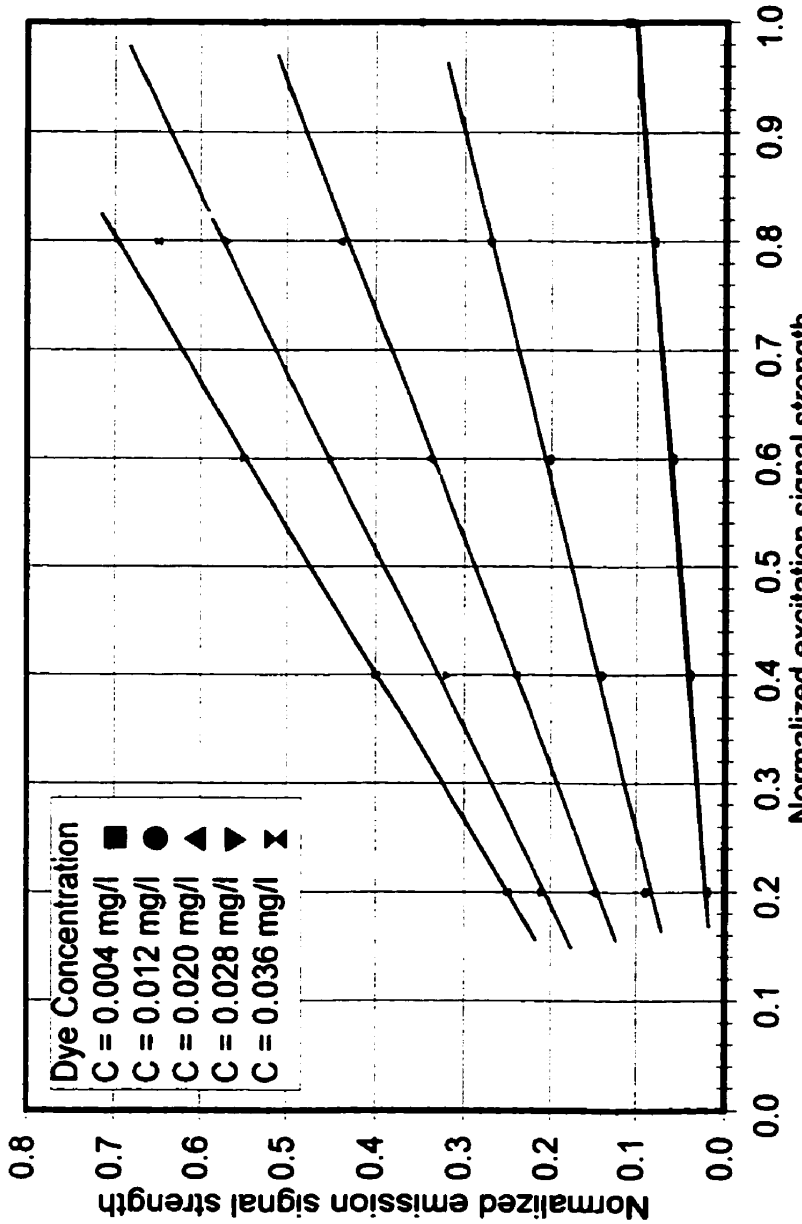

Figure 10. Behaviour of dye emission signal strength with excitation signal strength for various dye concentrations.

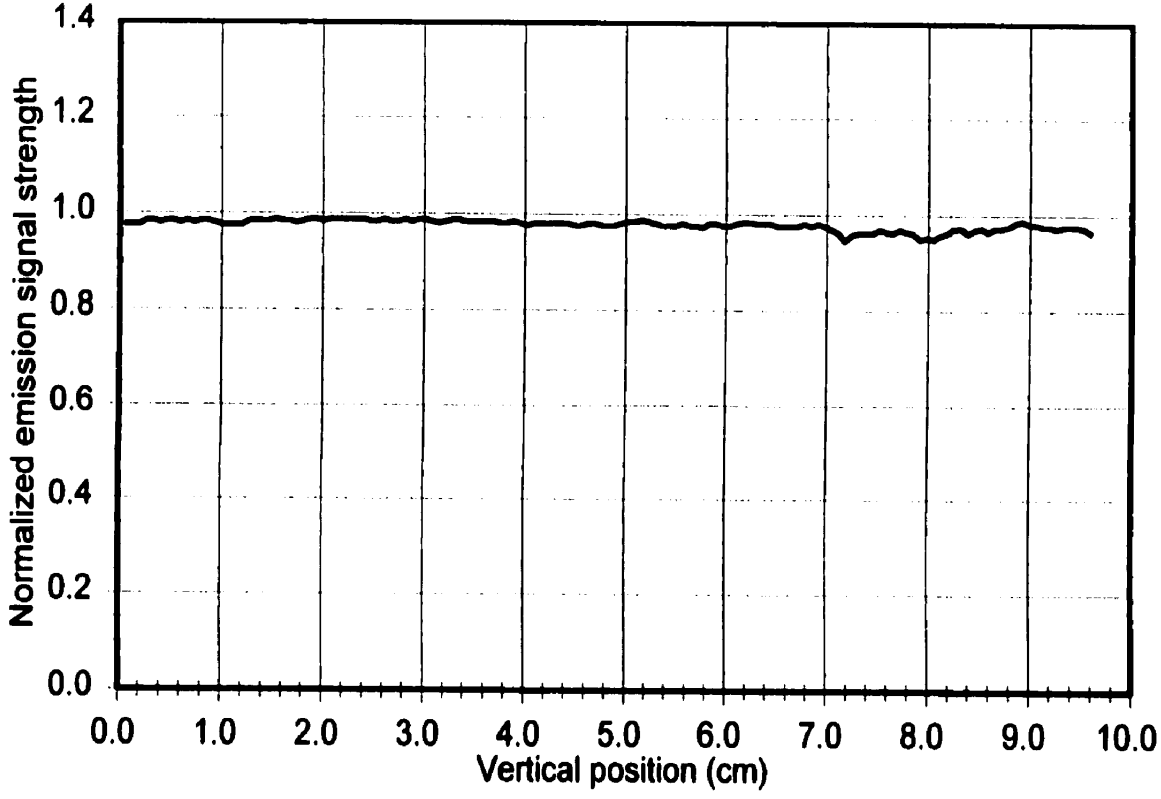

Figure 11. Single-line, vertical profile of the emission signal measured in a 10 cm layer of homogeneously mixed and dyed solution indicating that excitation signal attenuation is negligible under test conditions.

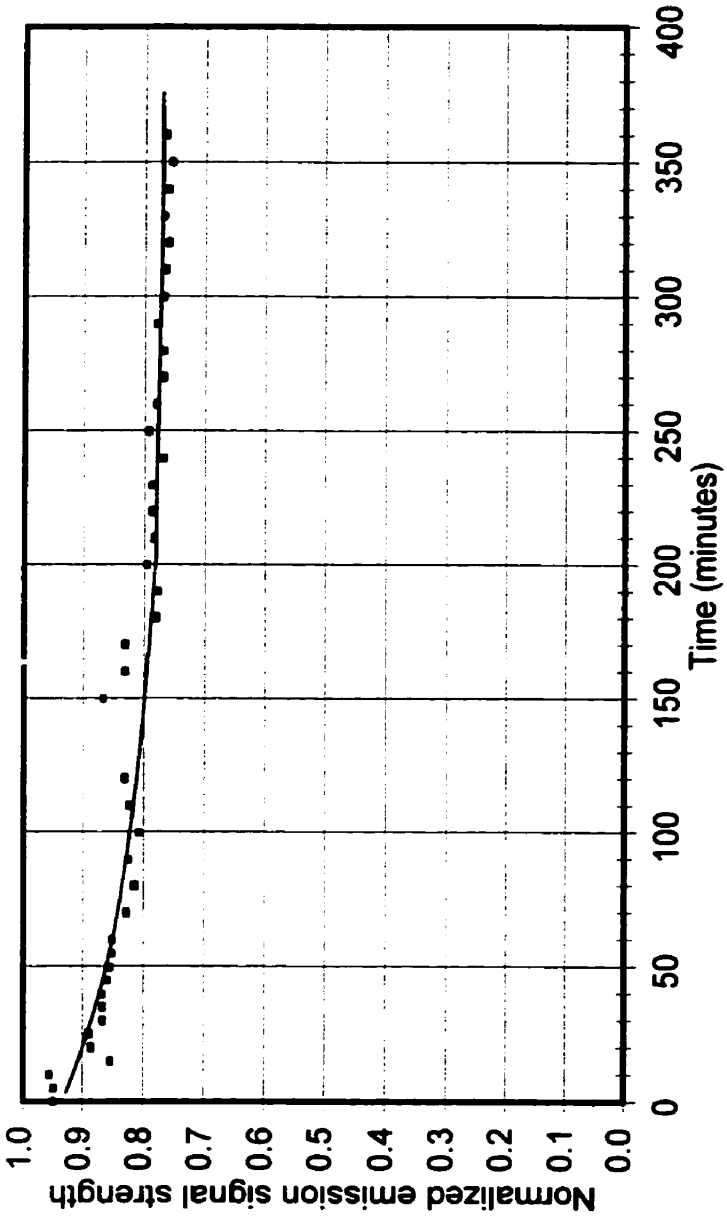

Figure 12. Time-dependent effect of chemical oxidation on the emission signal strength indicating that it is preferable to use aged dye solutions.

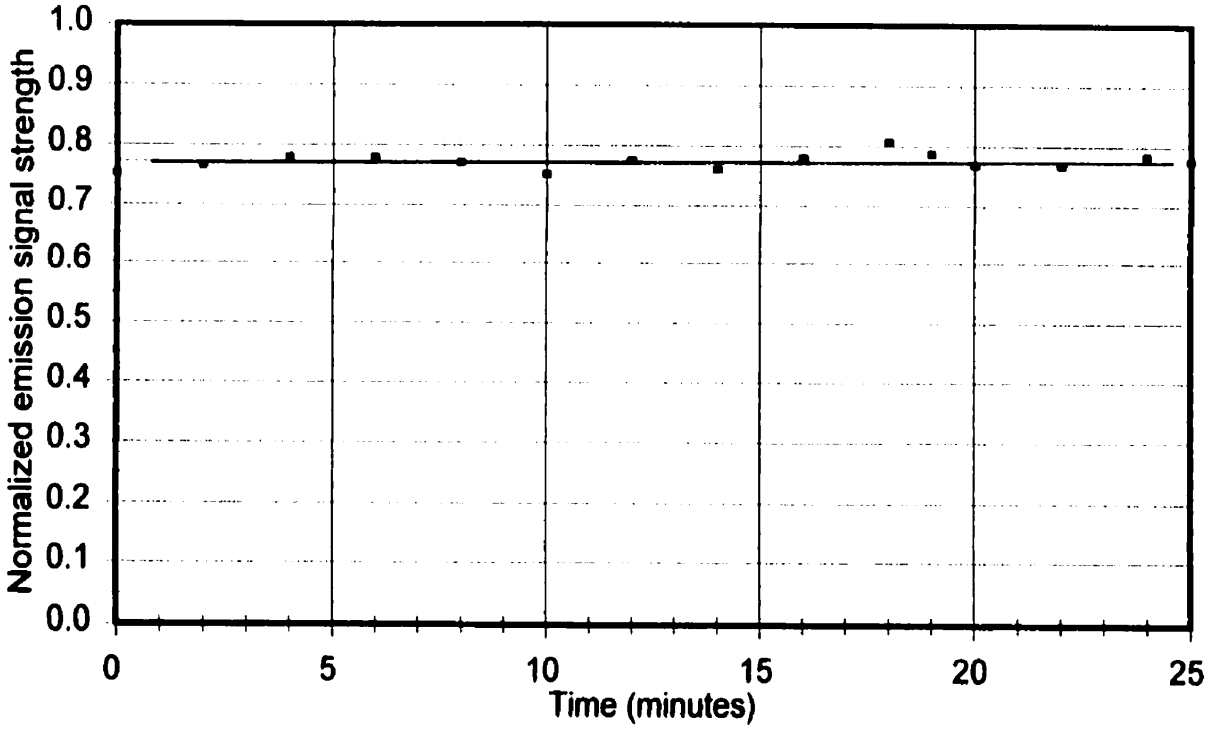

Figure 13. Time-dependent effect of photo-decomposition on the emission signal strength measured in an aged dye solution.

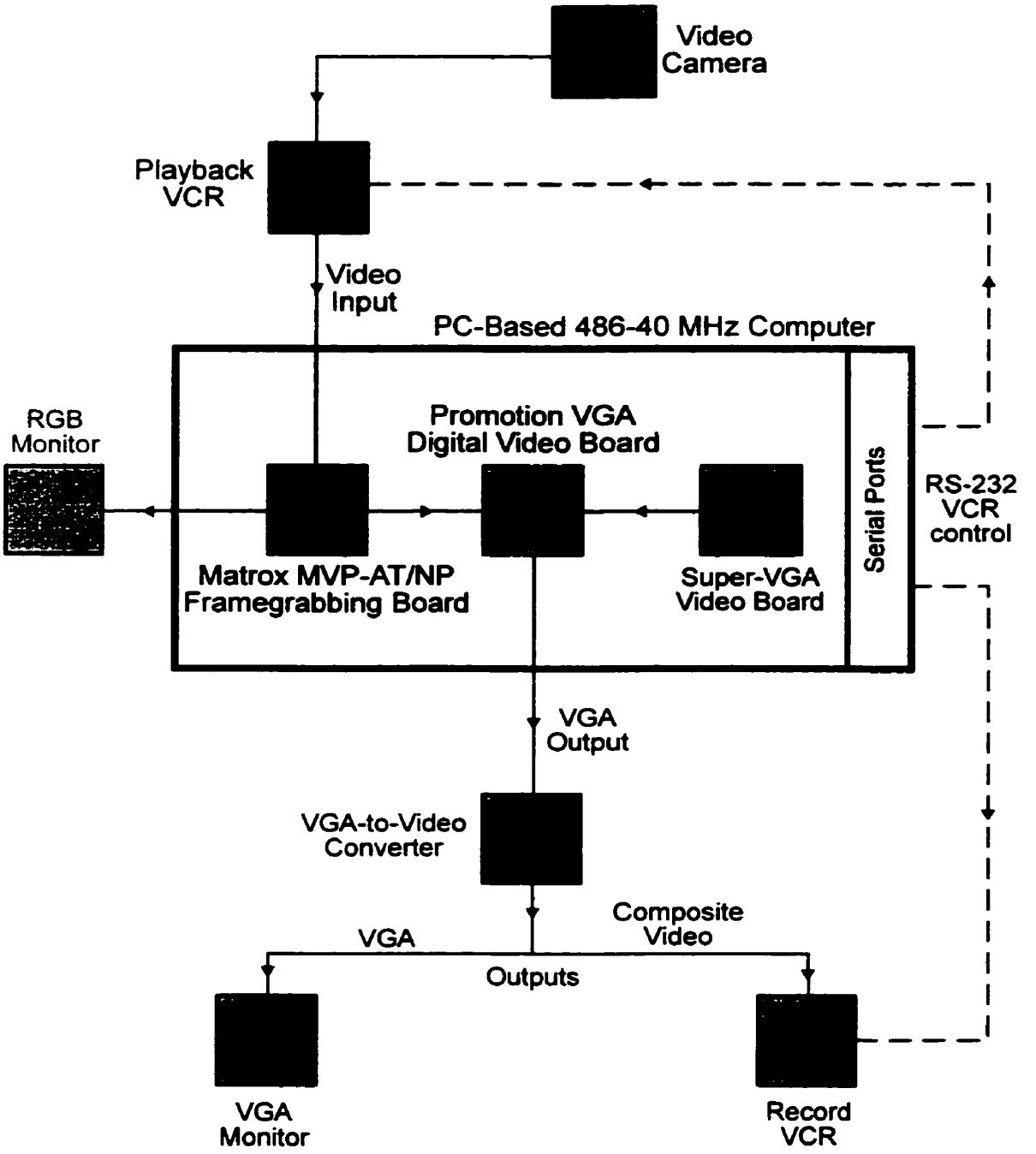

Figure 14. Schematic diagram of the image processing system.

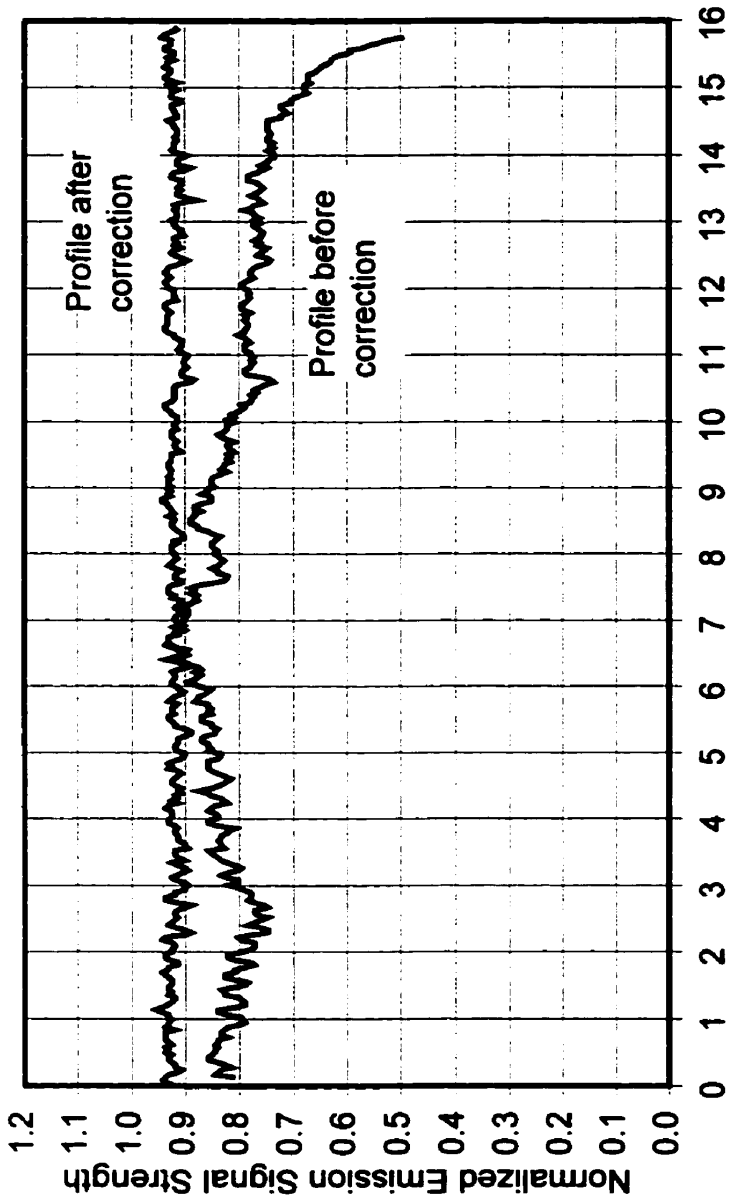

Figure 15. Horizontal emission signal profiles before and after the applicaton of the image correction routine.

a)

b)

Figure 16. Gravity current images a) before and b) after enhancement with image processing techniques.

a)

b)

c)

Figure 17. Gravity current images illustrating the effect of time-averaging when frame grabbing for a) a single snapshot, b) a 10 frame average and c) a 30 frame average.

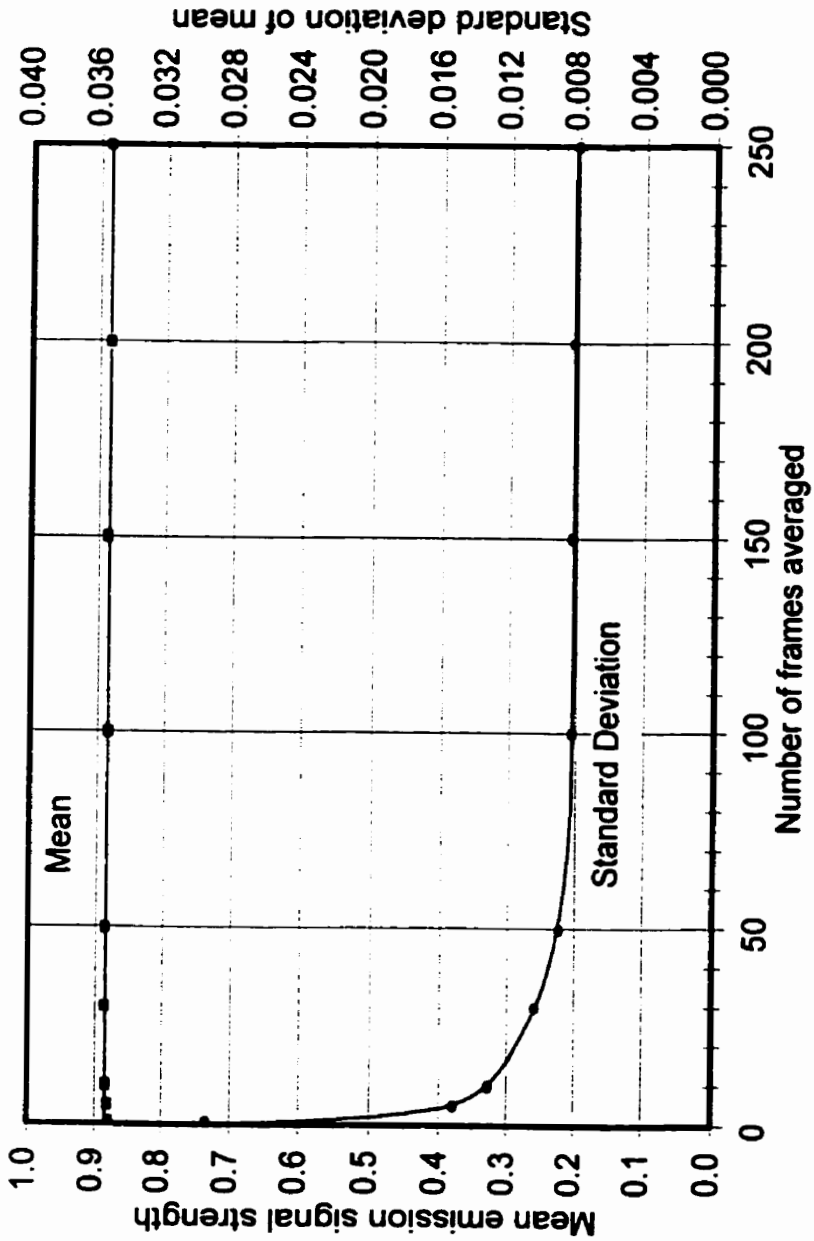

Figure 18. The effect of the frame averaging time period on the measured mean emission signal strength and the spatial standard deviation of the mean.

CHAPTER 3

SCALING

3.1. Limitations of Salt-water Modelling

The salt-water modelling technique used in the current work has two basic restrictions. The first is that modelling extends only to Boussinesq flows in which the fluid density excess is less than approximately 20% as described by Gröbelbauer et al. (1993). The second is that only isothermal, adiabatic flows can be generated in the experimental channel. Notwithstanding these restrictions, useful qualitative and quantitative information about the mixing dynamics in a gravity current can be gained and applied to larger scale problems.

The Boussinesq flow constraint is a result of the choice of working fluids used by the modelling technique itself. The maximum fluid density excess attainable with typical liquids such as saline and fresh water is approximately 20%. As previously mentioned, work by Gröbelbauer et al. shows that this density excess is at the upper extreme for Boussinesq flows. Modelling much higher density differences common to non-Boussinesq flows requires the use of gas flows as used by Gröbelbauer et al.

The Boussinesq approximation assumes that $\rho_A \sim \rho_B$ whereby density variations between the fluids are small enough to assume incompressible flow conditions. The contribution of these density variations, while important in the buoyant terms, can be neglected in so far as they affect inertia (Turner, 1973). Their effect appears solely in the

source reduced gravity term, $g'_s = g(\Delta\rho/\rho_A)$. Note that since the fluids have similar densities, it is not critical which fluid density is used in the denominator of this expression. The form stated above is adopted here, however.

Isothermal conditions exist in the experimental modelling method used for this work. Consequently, heat transfer effects within the flow and between the flow and its boundaries cannot be modelled. Implications of this restriction arise, for example, when results from such an experiment are extended to a full-scale cold pressure liquefied gas release. During the subsequent spread, appreciable heat transfer occurs from the surroundings to the gas so that it is warmed. Consequently, the buoyant driving force decreases and the cloud eventually decelerates.

In the full-scale, far-field scenario, however, it is reasonable to assume that cloud dilution results in a system that approaches near-isothermal equilibrium with its boundary and surroundings. Under these conditions, the small-scale, isothermal, adiabatic modelling method currently being used is acceptable so long as the initial density excess for the small- and full-scale flows is the same (Meroney, 1982). Validation of far-field modelling will be discussed in a later section.

3.2. Scaling Concerns and Relations

Mitigation of the consequences of heavier-than-air gas dispersion is one of the primary objectives of research such as the current work. Exact modelling of HTAG flows, however, requires simultaneous scaling of all the appropriate processes taking place over a wide range of length and time scales. Necessarily, this difficult task

demands an understanding of the interaction of the flow dynamics with many other processes such as material condensation and chemical reaction.

The problem, then, becomes one of developing a manageable system of scaling laws that will allow confident application of small-scale results to larger scale situations. Typically, a large number of scaling parameters are required to fully describe the complex flows found in HTAG dispersions. Unfortunately, exact scaling of each is not always possible and it becomes necessary to choose which laws must be obeyed and which may be neglected.

Much of the scaling difficulty arises in the near-field region where the flow is greatly complicated by the influence of the source. For example, the flow of material escaping from a ruptured pipeline is dominated by the momentum of the issuing jet in the region close to the rupture. At some distance from the source, however, the influence of the jet diminishes and the gas cloud becomes negatively-buoyant, slumps to the ground and spreads laterally.

Consequently, adherence to the source scaling requirements is not as critical in the far-field region where the influence of the source mechanism is less prevalent. For the negatively-buoyant gas cloud in this region, the description of its horizontal spread is found to be greatly simplified. Its motion is known to be governed primarily by the densimetric Froude number, the initial fluid density excess and, to a much lesser extent, the Reynolds number.

It turns out, though, that it is not practically possible to match both the Froude and Reynolds numbers when scaling between small- and large-scale flows. However,

further simplification can be made since, for buoyancy-dominated flows, the Froude number is found to be the more important scaling criteria (Hoot and Meroney, 1974). Fortunately, then, the Reynolds number scaling criteria can be relaxed as long as the flows exhibit highly turbulent characteristics and the shear layer turbulence is similar to that of the full-scale flow (Snyder, 1981).

In the case of gravity currents, fully developed turbulent flows are known to exist for Reynolds numbers down to about 1000 based on the head characteristics. Recalling Figure 3, the experimental work of Schmidt (1911) was the first to support this observation. Agreeing with Schmidt, later work by Keulegan (1949, 1957, 1958) and Simpson and Britter (1979) suggests that the dynamics of a gravity current display a Reynolds number independence for Reynolds numbers above 1000. Hence, full-scale Reynolds numbers need not be attained in small-scale flows.

Although the Reynolds number is not the important scaling criteria, its definition is still described here. Various forms of it have been reported in past literature. Typically, though, it is based on one of the following combinations of variables: 1) the layer height behind the head, H', and the head frontal velocity, u_2, (Simpson and Britter, 1979), 2) the layer height behind the head, H', and velocity of that layer, U', (Zukoski and Kubota, 1988) or 3) the head height, h_2, and its velocity, u_2 (Simpson and Britter, 1979).

Fundamentally, use of the second combination of variables, U' and H', is more suitable since their product can be shown to be the volumetric injection rate per unit channel width, Q, where $Q=UH=U'H'=U_SH_S$. Note that U' and H' refer to values in the layer immediately behind the head while U_S and H_S refer to values near the inlet edge.

This rationale defines a Reynolds number that is based on the undisturbed upstream source characteristics and is not a function of the shape of the gravity current head. These variables are, thus, used to define the Reynolds number as

$$Re = \frac{U H}{\nu_B} = \frac{Q}{\nu_B} \tag{3-1}$$

where ν_B is the source fluid kinematic viscosity.

As the Froude number is typically based on some characteristic velocity and length scale, it could be based on these same parameters such that

$$Fr = \frac{U}{\sqrt{g'_S H}} = \frac{Q}{\sqrt{g'_S H^3}}. \tag{3-2}$$

Here, U and H represent some characteristic velocity and height. The choice of the proper form of this Froude number equation will be discussed later.

Consequently, as Reynolds number scaling is not critical in the far-field region, it is only necessary to scale the buoyant source driving force using the densimetric Froude number and the source fluid density excess regardless of how the density difference between the fluids is generated. When these scaling criteria are adopted for small-scale, salt-water modelling experiments, however, they are subject to some basic assumptions summarized as follows: 1) the far-field region of a gravity current flow is modelled, 2) the gravity current flow is essentially two-dimensional although, within its structure, three-dimensional patterns exist, 3) the gravity current flow is isothermal and adiabatic,

4) only Boussinesq flows with relatively small density excesses can be modelled, 5) the flow is non-reacting and 6) no ambient wind conditions are considered.

3.3. Justification of the Modelling Technique

Gas concentrations in the near-field source region of a HTAG dispersion can be very high. Since these large concentrations lead to large density excesses between the cloud and ambient air, models based on the Boussinesq approximation may not be valid. This is not necessarily true, however, in the far-field region where gas concentrations and, thus, densities are much lower due to dilution of the cloud with ambient air. Accordingly, this downstream far-field region is the one considered in the present gravity current modelling research.

From a safety point of view, the regions of concern are those in the far-field where component gas concentrations are within the flammability limits of a flammable gas or above the safe human exposure level for a toxic gas. For flammable gases such as propane, butane and cyclohexane, the fluid density excesses that correspond with the flammability limits are 1-5%, 2-10% and 2-19%, respectively. For the toxic gas chlorine, for example, concentrations yielding fluid density excesses far below these levels are still considered hazardous for human exposure. Consequently, the initial fluid density excesses used in the present experiments are in the range of 1-5%. Tracking of flows continues until the mean fluid density of the structure falls to levels as low as 0.1% greater than that of the ambient fluid.

CHAPTER 4

GRAVITY CURRENT EXPERIMENTS

4.1. Experimental Matrix

Three series of tests were performed in the water channel facility using the techniques previously described. These tests were designed to examine gravity current flows in which the value of the source fluid density excess, $(\Delta\rho/\rho_A)_S$, was 0.01, 0.03 and 0.05. Injection flowrates, Q, of 10.3, 10.6 and 10.8 cm^2/s, corresponding to the above fluid density excesses, were used to generate source buoyancy fluxes of 101, 312 and 530 cm^3/s^3, respectively. The height of the ambient fluid, h_1, was set to 30.0 cm for each test. Each test was recorded on video tape for further analysis.

Based on these conditions and the definition of the Reynolds number adopted for this work, $Re = Q/\nu$, each of these flows had a Reynolds number of approximately 1000. It will be shown that the corresponding Reynolds number based on the current head height and velocity, $Re = u_2h_2/\nu$, was approximately 2000. This ensured that turbulent characteristics existed in each flow and that the dynamics of the head were independent of the Reynolds number, as described by Schmidt (1911).

Five surface roughness conditions were examined for each of the three values of fluid density excess considered, yielding a total of fifteen tests. These included a smooth-surface condition for each test series which provides a base case against which the rough-surface flow results can be compared. Results from these smooth-surface

tests are, also, compared to those found in the existing literature and serve to validate the modelling and visualization techniques presented here. The rough-surface configurations consist of arrays of two-dimensional, square-beam roughness elements with h_R=d= 6, 13, 19 and 25 mm and a downstream pitch of S/d=2 as described in Section 2.1.2 and illustrated in Figure 7.

4.2. Quantification of Results

Recall Figure 4 from Section 1.3.1 in which the gravity current flow parameters are illustrated. The ambient fluid height, h_1, and the fluid densities, ρ_A and ρ_B, are established prior to an experiment. The fluid densities set the source fluid density excess, $(\Delta\rho/\rho_A)_S$, of the system which is combined with the source volumetric injection rate per unit channel width, Q, and the acceleration of gravity, g, to define the buoyancy flux, $B_S=g'_SQ$, of the gravity current source.

The height of the current head, h_2, can be scaled directly from processed images as the highest extent to which shear-generated billows reach before they break away from the head structure. The downstream frontal position, X, of the gravity current head, measured from the inlet edge, can be determined from a frame-by-frame analysis of the video record. Correlating this frontal position with the time record of the gravity current spread yields the mean gravity current head frontal velocity, u_2, where $u_2=dX/dt$.

The source injection rate, Q, in the gravity current layer at any downstream position, x, can be expressed as the product of the layer height, H, and velocity, U, at that position. By continuity, this relation is valid for any section along the gravity current

source layer. The significant assumption here, though, is that there is negligible fluid transport, or mixing, across the horizontal interface between the gravity current source fluid and the mixed fluid layer above it. Work by Ellison and Turner (1959) has shown that an interface of this type is gravitationally very stable and, consequently, the entrainment across it is negligible.

The measurement of H from processed images at any downstream position allows the layer velocity, U, to be determined at that downstream section. The measurement of these parameters at a section immediately behind the head, however, is of primary interest as it allows an estimate to be made of the volume flux of source fluid feeding the head. At such a section, these parameters are expressed as H' and U'. H_S and U_S are used to refer to the layer height and velocity near the source at the inlet edge.

Quantification of the velocities and vertical scales of a gravity current flow is necessary to determine the densimetric Froude number. Various definitions of this non-dimensional parameter have been previously described in Section 1.3.1. The results of each definition will be considered in later sections. Image analysis allows determination of the mean, peak and spatial standard deviation of the fluid density excess of the gravity current head for various downstream positions. From this, the buoyancy flux of the gravity current head, B_H, can be quantified. This information is then used to quantify the downstream dilution for the various surface conditions.

Lengths, times and velocities for the smooth-surface flows will be non-dimensionalized, or normalized, using the reference scales defined in Section 1.3.1.

Repeated here, they are: $d_{REF}=(Q^2/g'_S)^{1/3}$ for lengths; $t_{REF}=(Q/g'^2_S)^{1/3}$ for times and $u_{REF}=(g'_SQ)^{1/3}$ for velocities. As pointed out, these scales are functions of the parameters that completely define the source strength, $B_S=g'_SQ$, but were developed for smooth-surface flows only. The buoyancy flux of the head, B_H, is normalized as a fraction of the source buoyancy flux, B_S, to define the head buoyancy flux fraction, B, where $B=B_H/B_S$. An alternate approach for normalizing rough-surface flow data will be discussed in a later section.

CHAPTER 5

SMOOTH-SURFACE FLOW RESULTS AND DISCUSSION

5.1 Gravity Current Spread Rates

Figure 19 shows a typical time history of the gravity current head frontal position resulting from a frame-by-frame analysis of the video record. In this case, the flow is over a smooth surface (h_R=0) with $(\Delta\rho/\rho_A)_S$ = 0.03 and a source buoyancy flux, B_S, of 312 cm^3/s^3. The figure shows the head frontal position plotted against the elapsed advance time. The data points indicate that there are three distinct flow regimes as described by Didden and Maxworthy (1982), Chobotov et al. (1987), Chan et al. (1993) and others.

The first regime lasts for a short time at the beginning of the flow. During this period, the gravity current is observed to accelerate to some constant frontal velocity which is the primary feature of the second flow regime. As described in Section 1.3.1, this constant velocity flow is governed by a balance between the inertial and buoyant forces. The characteristic linear relationship which defines the advance rate for this inertial-buoyant regime is indicated on Figure 19.

At some downstream point, it is observed that the data points begin to diverge from the linear, constant velocity trend. Downstream of this point, viscous forces become increasingly more significant and replace the inertial forces in the balance with

buoyancy. This is known as the viscous-buoyant regime in which the flow is observed to decelerate as it advances further down the channel.

The spread rate equation for the inertial-buoyant flow regime, Equation 1-5, indicates that X=f(t) with X=0 at t=0. Due to the initial acceleration experienced by the flow, however, the linear relation indicated by the data in the inertial-buoyant regime of Figure 19 does not satisfy this initial condition. It becomes necessary, then, to extrapolate this linear relation back to the X=0 axis to yield a time offset which can be subtracted from the original video time record. This time axis shift corrects for the initial acceleration period and forces the initial condition of X=0 at t=0. Accordingly, the X-t data for each test was treated in this manner to compensate for the initial flow acceleration regime.

Figure 20 shows the results of this procedure for the three smooth-surface tests in which $(\Delta\rho/\rho_A)_S$ = 0.01, 0.03 and 0.05. In this figure, the data for the initial flow acceleration is not shown. Lines are fitted to the data to highlight the inertial-buoyant regimes of each flow and to emphasize the degree of divergence in the data for the viscous-buoyant flow regime. The inertial-buoyant/viscous-buoyant transition position is indicated for each flow.

The first thing to note from this data is that, in the inertial-buoyant flow regime, the slope of the X-t line, dX/dt, is the constant head frontal velocity, $u_2=C(g'_SQ)^{1/3}$. This spread rate is observed to increase with increasing fluid density excess, $(\Delta\rho/\rho_A)_S$. This trend is expected since the driving buoyancy flux is directly proportional to the fluid density excess. Mean head frontal velocities of 4.3, 6.3 and 7.2 cm/s were observed in

the inertial-buoyant flow regime for smooth-surface gravity current flows with initial density excesses of 0.01, 0.03 and 0.05, respectively.

Figure 21 shows this same data normalized using the characteristic length and time scales, d_{REF} and t_{REF}, described in Section 1.3.1. In this representation, the smooth-surface spread rate data collapses onto a single line with relatively little scatter. The slope of this line is, therefore, the normalized frontal velocity, u_2^*, which is the constant, C, in the dimensional spread rate equation (Equation 1-5) previously presented. It has a value of 0.91+/-0.02 for the inertial-buoyant regime and appears to be independent of the fluid density excess over the range tested. In another presentation, Figure 22 shows u_2^*, as calculated from the spread rate equation, plotted against X^*. This data highlights the constant velocity, inertial-buoyant flow regime.

As noted in Section 1.3.1, this normalized frontal velocity is the densimetric Froude number based on the head velocity and the source conditions, g'_S and Q. The results of the smooth-surface tests presented here agree reasonably well with those of other authors. Chobotov et al. (1987) concluded that, over a range of Reynolds numbers of 1000-3000, this Froude number varied from 0.75-0.85. Chan et al. (1993) proposed a value of 0.89 for this constant for the Reynolds number used in the present work. Zukoski and Kubota (1988) proposed a value of 0.9.

Figures 21 and 22, also, indicate that the normalized downstream position, X_t^*, at which the inertial-buoyant/viscous-buoyant transition is observed to occur is 82+/-6. This agrees very well with Chan et al. (1993) who concluded that this transition occurs at a value about 88+/-11 for Reynolds numbers, Re=Q/v, greater than approximately 1000.

For Reynolds numbers of approximately 1000 and less, their data exhibits slightly more scatter. This transition, however, does not occur abruptly but gradually over a region.

By plotting the X^* versus t^* data on a log-log scale, the functional relationships between position and time can be shown for the inertial-buoyant and viscous-buoyant smooth-surface flow regimes. Figure 23 shows that, as expected, the inertial-buoyant regime is described by a line with a slope of 1.0 indicating that X is a linear function of t. Beyond the transition region, theory and experiment on viscous spreads (Didden and Maxworthy, 1982, Huppert, 1982) have shown that the trend of the data points should tend towards a slope of 0.8. The present data indicates a value of approximately 0.85. However, as transition does not occur abruptly, it is concluded that insufficient channel length precludes a value of 0.8 from being reached.

5.2 Head and Layer Thicknesses

The turbulent shear mixing at the current/ambient fluid interface generates waves and billows at the upper boundary surface of the head. Despite the downstream variability of the gravity current head height, h_2, due to these disturbances, an attempt was made at measuring it to quantity the head's characteristic shape. The head height is an important parameter commonly used in the literature, as has already been described, to define the Reynolds and Froude numbers of the flow.

Figure 24 shows the normalized gravity current head height, h_2^*, as a function of the normalized downstream position, X^*, for the three smooth-surface flows. The data collapses reasonably well indicating that the normalized head height is independent of

the fluid density excess over the range investigated. In addition to this, the normalized head height appears to be independent of X^* over the length of the channel and has a value of approximately 2.20+/-0.14. Data for the gravity current head height, normalized in the manner used here, is not often reported in the literature. Chan et al. (1993), however, reported a value of 1.59 for this characteristic parameter.

It is not clear, at this point, exactly how the difference between these values should be accounted for except that interpretation of the measurement of h_2 can vary significantly due to the billowing action at the upper surface of the gravity current's head. As will be shown, the current layer height immediately behind the head is approximately equal to the characteristic length scale, d_{REF}. Observations by Keulegan (1958), Wilkinson and Wood (1972) and Chobotov et al. (1987) suggest that the height of the head is about twice that of the layer behind it. A value of approximately 2 for h_2^* when normalized using d_{REF} is, therefore, not unreasonable.

The height of the ambient fluid, h_1, has been observed to play a role in gravity current flow dynamics. It has been shown by Chobotov et al. (1987) and Wilkinson and Wood (1972), however, that for fractional current head depths, h_2/h_1, of the order of 0.1, the influence of the free surface of the ambient fluid is negligible. In the smooth-surface tests reported here, this fractional height is less than 0.1. For flows over the roughest surfaces, the fractional height, in this work, is of the order of 0.2. Consequently, it is believed that the free surface has a minimal effect on the flow dynamics over the range of flows studied here.

In addition to the head height, the source layer height immediately behind the head, H', was measured for each smooth-surface test. In Figure 25, a plot of H'^* versus X^* shows that this normalized height is independent of downstream position and has a value of 0.93 ± 0.02. As was the case with measurements of h_2, however, variation in this data can be attributed to the wavy action of the layer immediately behind the head.

In addition, Figure 25 indicates that the normalized source layer height here is very close to the characteristic length scale, d_{REF}, and that it is independent of the source fluid density excess, $(\Delta\rho/\rho_A)_S$. Chan et al. (1993) reported that H'^* decreases with increasing X^* in a linear fashion by approximately 20% over a normalized distance of 140. No such trend was observed in the present smooth-surface tests. It is interesting to note, however, that the value of H'^* reported here is very close to the initial value of 0.85 reported by Chan et al.

Consequently, the ratio of the head height to the height of the layer immediately behind the head, $(h_2/H')^*$, is found to be 2.38 ± 0.21 for the smooth-surface tests. Keulegan (1958) reported this value to be 2.16. Other authors such as Wilkinson and Wood (1972) and Chobotov et al. (1987) reported this ratio to be approximately 2. Considering the variability in the measurements of these heights, the present data agrees reasonably well with the literature. The primary conclusion, however, is that for smooth-surface flows the general shape of the gravity current head remains unchanged as it progresses down the channel.

Figure 26 shows the height of the source layer, H_S^* measured at a fixed position near the channel inlet edge (x=30 cm, x^*=14, 19, 22 for $(\Delta\rho/\rho_A)_S$ = 0.01, 0.03, 0.05,

respectively) as the gravity current flow progressed down the channel. Measurement started immediately after the head passed the fixed measuring position. The initial data point, therefore, represents the height of the source layer immediately behind the head, H'^*. It can be seen that this initial measurement agrees well with that of Figure 25. Unlike the layer height, H'^*, immediately behind the head, however, Figure 26 shows that the layer height at a fixed position near the inlet edge grows as the current progresses down the channel such that $H_s^* = f(X^{*\,1/6})$.

This layer growth near the inlet edge is expected, however, and can be explained as follows. The total viscous retarding force between the gravity current and its surroundings is a function of contact area and, therefore, increases as the current gets longer. It can, thus, be reasoned that the growth in the source layer near the inlet edge is necessary to produce the additional hydrostatic pressure head required to drive the flow against the increasing friction at the lower solid boundary. This conclusion was also presented in the work of Chan et al. (1993).

Didden and Maxworthy (1982) and Huppert (1982) have shown that this viscous force is primarily due to the shear stress at the solid boundary and that the shear stress at the current/ambient fluid interface is negligible for a bottom flowing current. Further, their results showed that the viscous stress due to contact with the sidewalls can be safely neglected for ratios of channel width to layer height, w/H, greater than about 5. This ratio was found to be at least 10 for the tests performed here.

If the growth of the source layer is recorded for various downstream positions, a profile of the gravity current source layer can be obtained for a fixed point in time. Figure

27 illustrates this shape for a gravity current with a 1% source fluid density excess flowing over a smooth surface. The profile represents a snapshot of the source layer at a normalized time, t^*, of 113. At this time, the head frontal position, X^*, is approximately 100 so that this particular current stretches over approximately 90% of the channel length.

As expected, the interface between the gravity current and ambient fluids is sloped slightly downward toward the head. For the particular test shown, the slope is approximately 0.4%. The first point measured is near the inlet edge where the source layer height agrees with H_S^*, as shown in Figure 26. It is observed that there is good agreement between this data point and that of Figure 26 for $X^* = 100$. The last point measured represents a position just behind the gravity current head where the layer height is that indicated by H'^* in Figure 25. This point agrees well with the source layer height measured just behind the head as indicated in that figure.

5.3 Gravity Current Reynolds and Froude Numbers

In the previous two sections, the frontal velocity and characteristic heights of the smooth-surface gravity current were examined. With this information and that of the source strength, values of the various forms of the Reynolds and Froude numbers previously discussed can be determined.

In Section 3.2, it was suggested that, fundamentally, it would be better to base the gravity current Reynolds number on some combination of the source layer velocity and the source layer height where $Q=UH=U'H'=U_SH_S$. Since the source injection rate, Q,

is measured independently of the gravity current flow, direct measurement of the source layer velocity and its height is, therefore, not required to establish the Reynolds number. For this reason, as previously noted, the definition of the Reynolds number used here is $Re = Q/\nu$.

When the data for u_2^* and h_2^* from Figures 22 and 24 is used to calculate the gravity current Reynolds number according to the definition used by Simpson and Britter (1979), it can be shown, that

$$Re = \frac{u_2 h_2}{\nu_B} = \frac{(u_2^* u_{REF})(h_2^* d_{REF})}{\nu_B} = u_2^* h_2^* \frac{Q}{\nu_B} \approx 2\frac{Q}{\nu_B} \qquad (5\text{-}1)$$

where $u_{REF}d_{REF}=Q$. This suggests that the Reynolds number definition based on the head frontal velocity and height yields a value twice that given by the definition based on the source injection rate, Q.

Consequently, a Reynolds number of 1000, as defined in the present experiments ($Re=Q/\nu$), is equivalent to a Reynolds number about 2000, as defined in terms of the characteristic shape of the head ($Re=u_2h_2/\nu$). Hence, as described in Sections 1.3.1 and 3.2, turbulent characteristics will exist within the head structure and a Reynolds number independence will be observed (Schmidt, 1911, Keulegan, 1949, 1957, 1958, Simpson and Britter, 1979). This is confirmed by observation of the flow structures.

Based on the gravity current head height and frontal velocity, the Froude number is given by Equation 1-3. Using the characteristic length and velocity scales and recognizing that $u_{REF}/(g'_S d_{REF})^{1/2} = 1$, it can be expressed in a normalized form as

$$Fr = \frac{u_2}{\sqrt{g'_S h_2}} = \frac{u_2^* u_{REF}}{\sqrt{g'_S h_2^* d_{REF}}} = \frac{u_2^*}{\sqrt{h_2^*}}. \qquad (5\text{-}2)$$

The present data for u_2^* and h_2^*, as indicated in Figures 22 and 24, yield a value of 0.61 for this definition of the Froude number which is in good agreement with reported values in the literature. Keulegan (1958) proposed a value of 0.705 for this form of the parameter while Middleton (1966) and Winant and Bratkovich (1977) concluded that the value was closer to 0.66 and 0.62, respectively.

With reasoning as before, the Froude number can also be expressed in terms of u_2 and H' such that, in normalized form,

$$Fr = \frac{u_2}{\sqrt{g'_S H'}} = \frac{u_2^*}{\sqrt{H'^*}}. \qquad (5\text{-}3)$$

With the value of H'^* indicated in Figure 25, this definition yields a value of 0.94 for the present work which is in good agreement with the value of 1.04 reported by Keulegan (1958). Simpson and Britter (1979) reported a value of approximately 1.1.

As with the Reynolds number, the Froude number could be based on some combination of the source layer velocity and its height such that

$$Fr = \frac{U}{\sqrt{g'_S H}} = \frac{Q}{\sqrt{g'_S H^3}}. \qquad (5\text{-}4)$$

It becomes necessary, however, to have information about both U and H or, since U cannot be measured directly, about Q and H. By continuity, any U and H combination would suffice such as U_S and H_S or U' and H'.

As was shown in Figure 26, however, the layer height, H_S, at a fixed position near the inlet, grows as the gravity current progresses down the channel. Consequently, the corresponding velocity, U_S, decreases to maintain a constant Q, implying that the source Froude number decreases as the head progresses down the channel. In fact, the Froude number measured at any fixed downstream position would be observed to decrease with time as the source layer fluid passes by and the layer height grows at that point. It appears, therefore, that U_S and H_S may not be a very practical choice for the definition of the Froude number.

If, however, the definition is based on the source layer height and its velocity measured immediately behind the head, the Froude number would be observed to be constant. Recall from Figure 25 that H'^* was observed to be constant with downstream position. In this case, the Froude number is measured with respect to a section that moves with the gravity current head rather than one that is located at a fixed downstream position.

Based on U' and H', then, the Froude number, when normalized, would be given as

$$Fr = \frac{U'^{*}}{\sqrt{H'^{*}}} = \frac{1}{(H'^{*})^{3/2}} \qquad (5\text{-}5)$$

recognizing, again, that $u_{REF}/(g'_S d_{REF})^{1/2}=1$ and that $U'^{*}H'^{*}=U'H'/u_{REF}d_{REF}=1$. Using the constant value of H'^{*} shown in Figure 25 as 0.93, this Froude number definition yields a value of 1.12. No reported values based on this definition were found in the literature.

As previously noted in Section 5.1, a Froude number can be formed by normalizing the frontal velocity u_2 with the characteristic velocity scale, u_{REF}, such that

$$Fr = u_2^{*} = \frac{u_2}{(g'_S Q)^{1/3}}. \qquad (5\text{-}6)$$

The advantage of this form is that it is based on the measured frontal velocity, the controlled volumetric injection rate and the source fluid density excess. It is not a function of the geometry of the gravity current structure. This is the Froude number form adopted for this study. Recalling Figure 22, the Froude number, based on this definition, is found to be constant with a value of 0.91+/-0.02 for the smooth flow, inertial-buoyant regime. As previously indicated, this agrees well with the findings of Chobotov et al. (1987), Chan et al. (1993) and Zukoski and Kubota (1988).

5.4 Downstream Mixing in Smooth-Surface Flows

The gravity current head can be thought of as a mixing machine attached to the leading edge of the dense source fluid layer that flows under a deeper ambient layer of lighter fluid. Any mixing between these two fluids, then, is assumed to originate within this "machine". Necessarily, this mixing process results in the production of an intermediate density mixture of fluid that is transported out of the head and left behind it as the flow advances down the channel.

Recalling the work of Winant and Bratkovich (1977) and referring to Figure 5, conservation of the buoyancy flux of the head, B_H, and, thus, the mean fluid density excess of the head, $(\Delta\rho/\rho_A)_H$, requires that the net mass flux out of the head be zero as the current progresses down the channel. Consequently, the sum of the mass fluxes of the dense fluid into the head from the source layer and the lighter fluid entrained into the head from the ambient layer must equal that of the mixed fluid leaving the head. If perfect mixing is assumed to occur in this machine, the density of the mixed fluid leaving the head would be the mean density of the fluid within the head.

The variation of the gravity current head buoyancy flux fraction, B, with downstream frontal position is shown in Figure 28 for the three smooth-surface tests. The head buoyancy flux fraction represents the buoyancy flux strength of the head as a fraction of the source buoyancy flux strength. This is the same as the mean head fluid density excess fraction. The data shows that there is weak dependence on the source buoyancy flux and, thus, the source fluid density excess. In the initial constant velocity, inertial-buoyant stage of the flows, however, a pseudo steady-state is observed to exist

and the mean fluid density excess in the head is nearly conserved. For this condition, the mean head buoyancy flux fraction has a value of approximately 0.45+/-0.04. This indicates that the mean head fluid density excess is approximately one half that of the source fluid and, thus, the mass fluxes of the source and ambient fluids into the head are closely balanced.

An estimate of mean velocity in the layer immediately behind the head, U'^*, can be made using the estimate of H'^* determined from Figure 25. In doing this, inviscid slip conditions are assumed to exist at the current/ambient fluid interface and at the bottom wall such that the velocity profile in the source layer is uniform. It was noted in Section 5.2 that the shear stress at the fluid interface is negligible for a bottom flowing current when compared to that at the wall. Additionally, for the inertial-buoyant regime, viscous effects at the wall are not yet significant.

Recalling that $Q=U'H'$ and that $U'^*H'^*=1$, it follows that $U'^*=1.08$ when $H'^*=0.93$. Hence, the mean velocity ratio, U'/u_2, for the present smooth-surface experiments is observed to be approximately 1.19. This confirms that the velocity in the source layer just behind the head is greater than that of the head itself. This relationship is necessary to provide the dense fluid required to fuel the mixing process within the head. Without it, the head structure would be quickly diluted by the ambient fluid entrained into the head. Measurements made by Simpson and Britter (1979) show this velocity ratio to be 1.16+/-0.04.

The mean overtaking velocity at which this dense fluid enters the head, $(U'-u_2)$, can be used to estimate the volume flux of dense fluid entering the head from the

source layer, Q' (this is Q_2 as described by Winant and Bratkovich and Figure 5). When normalized as a fraction of the total volumetric source flux, Q, it follows that

$$Q'^{*} = \frac{Q'}{Q} = \frac{(U' - u_2) H'}{u_{REF}\, d_{REF}} = (U'^{*} - u_2^{*}) H'^{*}. \qquad (5\text{-}7)$$

Equation (5-7) shows that approximately 16% of the total source flux, Q, enters the head region from the source layer immediately behind it. Since the density of the fluid entering the head is assumed to be the same as that of the source fluid, this result is in very good agreement with measurements of Winant and Bratkovich (1977). They reported that the mass flux of dense fluid flowing into the head from the source layer is approximately 15% of the total source flux, Q.

In these smooth-surface flows, ambient fluid is entrained into the head structure almost entirely by shearing at the upper surface of the head (Simpson and Britter, 1979). This action is associated with Kelvin-Helmholtz waves and billows, initiated by the velocity and density gradients at the intruding head/ambient fluid interface. Simpson and Britter (1979), also, pointed out that a volume of lighter ambient fluid can be entrained into the head by being overrun by the structure. The effect of this influx of lighter fluid on the mixing, however, was reported to be negligible. In later sections, it will be shown that this volume of lighter fluid plays a much greater role in the overall mixing and dynamics of flows over rougher surfaces.

As the smooth-surface flows represented in Figure 28 move into the viscous-buoyant regime beyond about X*=82, the head buoyancy flux fraction is

observed to drop off in close proportion to $(X^*)^{-0.40}$ with very little dependence on the source fluid density excess. This decrease indicates that the flux of dense fluid into the head from the heavier flowing source layer becomes increasingly less than that of the lighter ambient fluid into the head. Steady state no longer exists. This is consistent with the increase in viscous shear effects that characterize this flow regime. More dense fluid is turned back in the growing no-slip boundary layer and, consequently, less heavy source fluid is available to feed the head and balance the influx of lighter ambient fluid.

The amount of dilution reported in Figure 28 over the full channel length, however, is still relatively small when compared to that observed in the rough-surface flows to be considered in later sections. Comparatively speaking, the viscous shear at the smooth wall does not have a very significant effect on the overall head dilution. Consequently, models that assume that the buoyancy flux of the head is conserved, as proposed by Didden and Maxworthy (1982) and many others, provide reasonable approximations of flows over smooth surfaces.

Thus far, mixing in the head was assumed to occur perfectly such that the head fluid density profile is spatially uniform and equivalent to the mean for all positions and times. This is not typical of real flows, however. Large spatial and temporal fluctuations in the head density are observed to occur within the gravity current throughout its advance. The locations and times of these fluctuations are nearly impossible to predict but an understanding of the variability of the mean head fluid density excess is extremely useful.

Figure 29 shows a typical five-contour buoyancy flux fraction profile for the head of a gravity current flowing over a smooth surface with $(\Delta\rho/\rho_A)_S$ = 0.01 and X*=40. As expected, strong density gradients exist near the current/ambient fluid interface and billowing waves flow over the head. Note the strong penetration of the dense source fluid layer into the central head region. For the same test and position, the fraction of the total head area occupied by a given buoyancy flux fraction is given in the histogram of Figure 30. The distribution is relatively uniform over the head section with a slight depression about the mean of 0.49.

For downstream, smooth-surface flows, the spatial variation of the buoyancy flux fraction within the gravity current head is quantified in Figure 31 in terms of the peak/mean and standard deviation/mean ratios. This figure indicates that, within the head, localized values of the buoyancy flux fraction reach levels two to three times greater than the overall mean values for the head. Over the region of the gravity current head, the spatial standard deviation of the buoyancy flux fraction is observed to be as much as 65-95% of the mean values.

As the flow moves into the viscous-buoyant regime, these ratios for the 0.03 and 0.05 fluid density excess tests appear to increase in proportion with the square root of X* as flow deceleration and mixing increase with further downstream position. There is insufficient data in the viscous-buoyant regime, however, to support this conclusion for the 0.01 fluid density excess test.

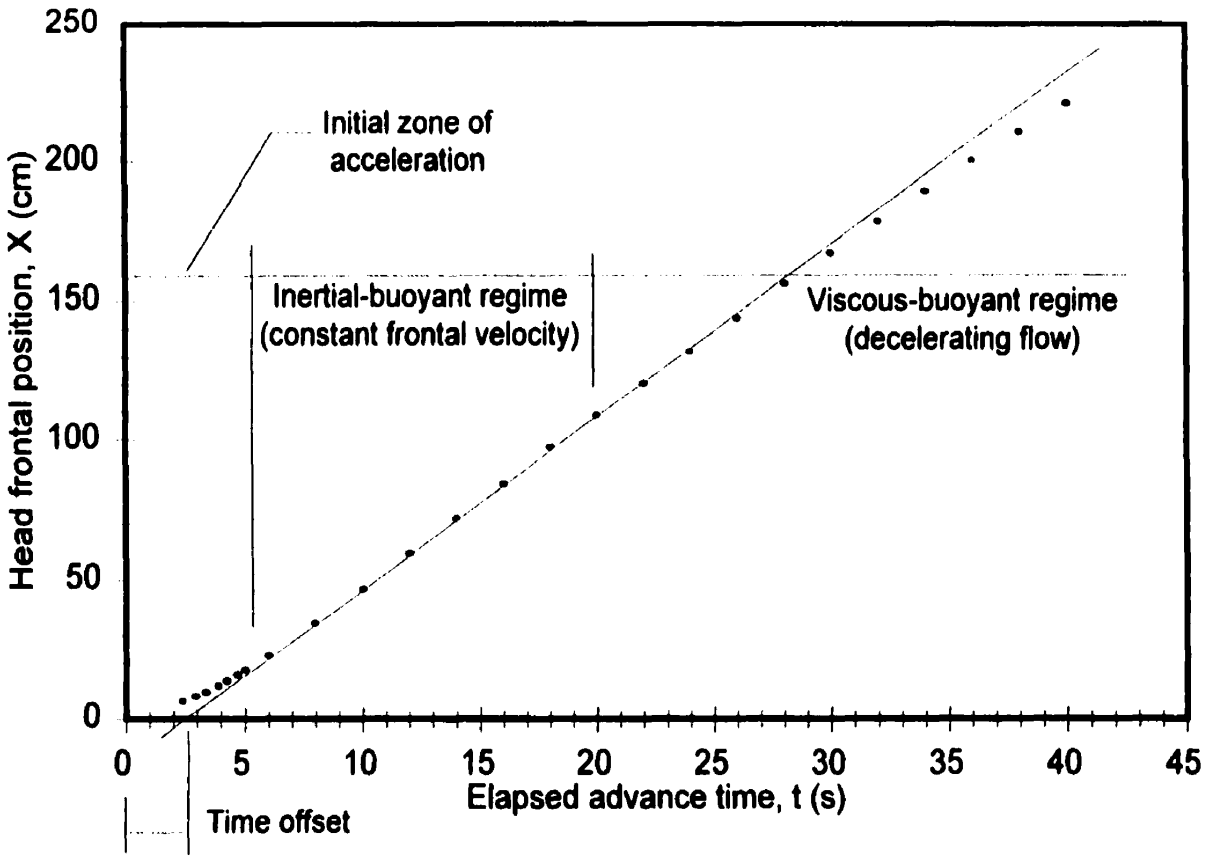

Figure 19. Typical time history of the gravity current head frontal position resulting from a frame-by-frame analysis of the video record. The data represents a smooth-surface flow with a source fluid density excess of 0.03.

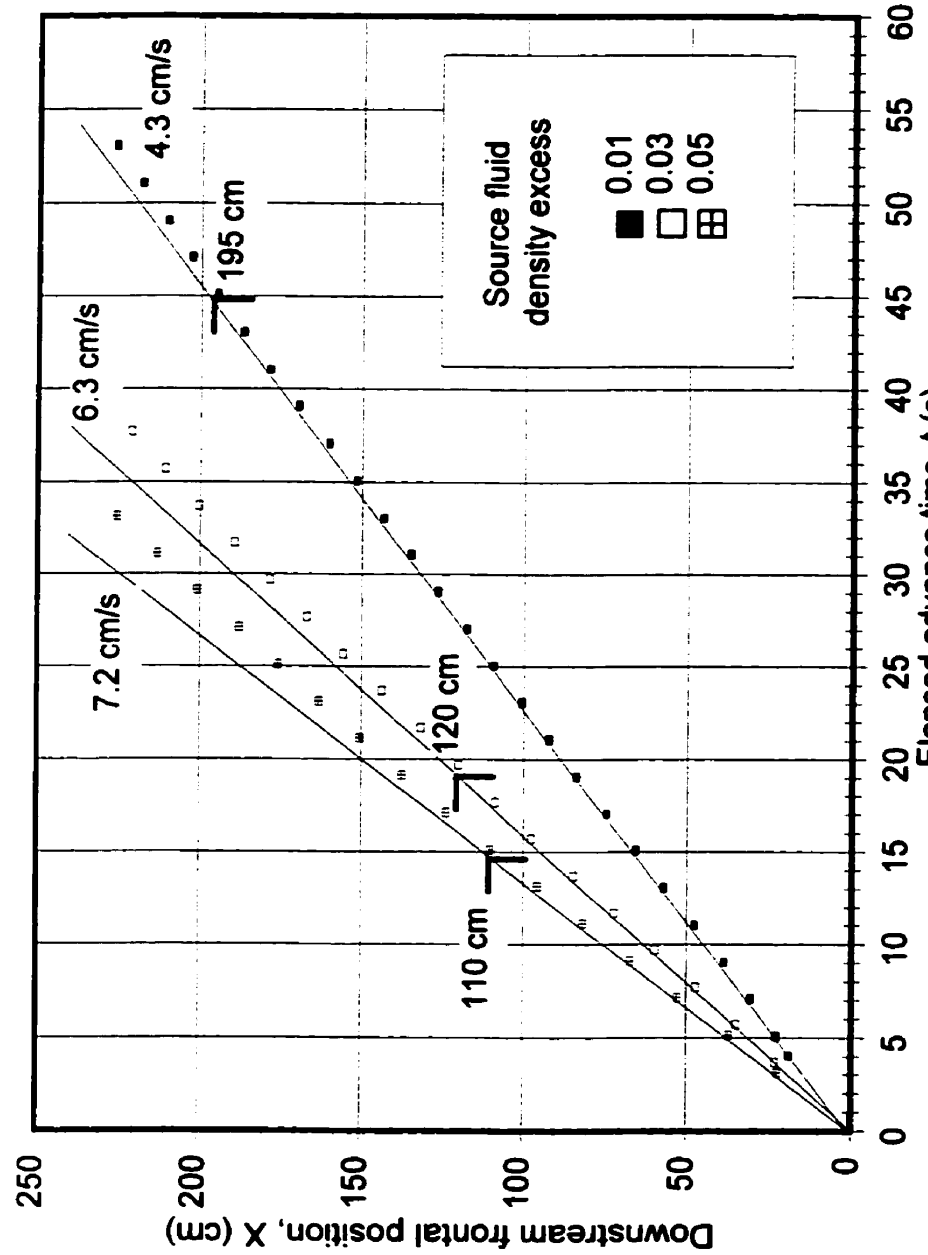

Figure 20. Time axis correction applied to the spread rate data for smooth-surface flows with source fluid density excesses of 0.01, 0.03 and 0.05.

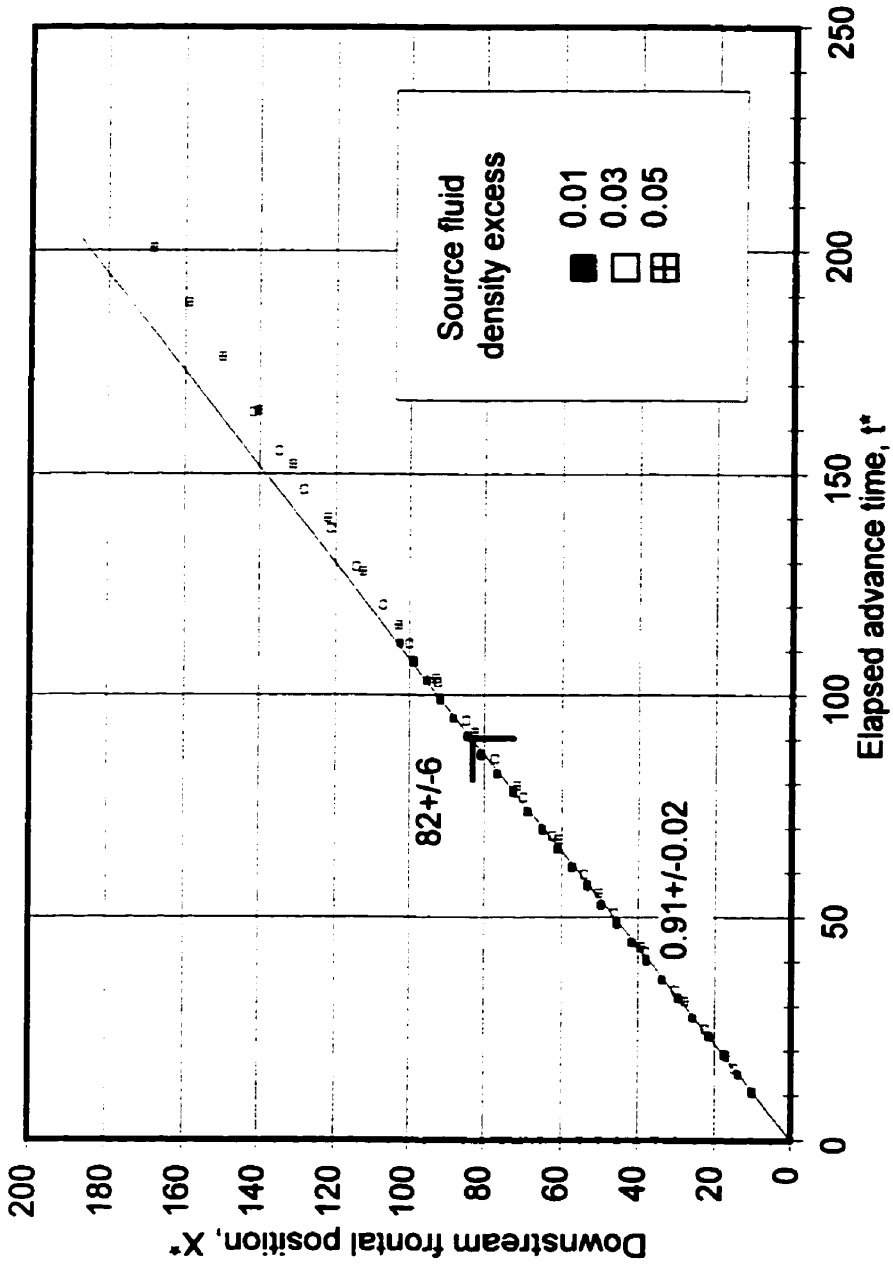

Figure 21. Normalized presentation of the spread rate data of Figure 20 for smooth-surface flows with source fluid density excesses of 0.01, 0.03 and 0.05.

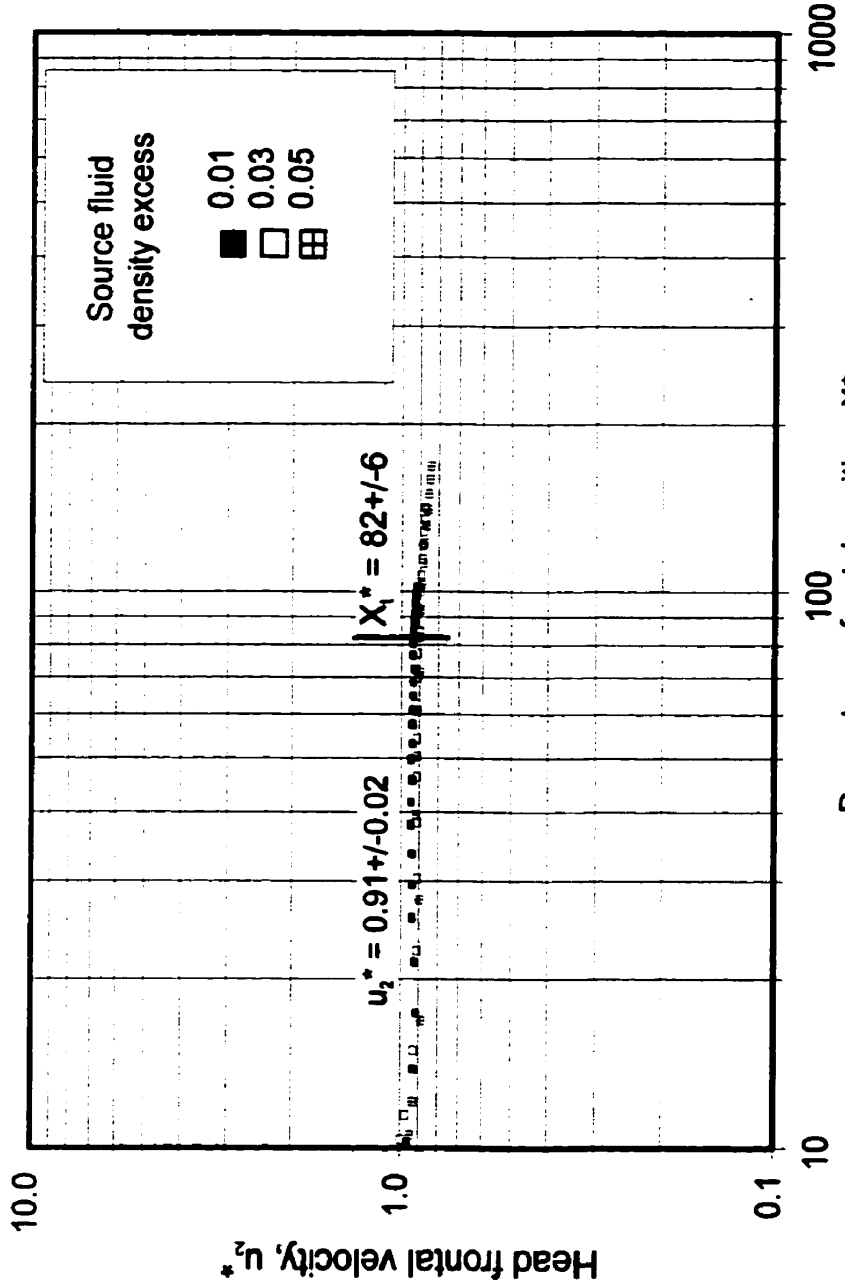

Figure 22. Normalized head frontal velocity presented as a function of the downstream frontal position for smooth-surface flows with source fluid density excesses of 0.01, 0.03 and 0.05.

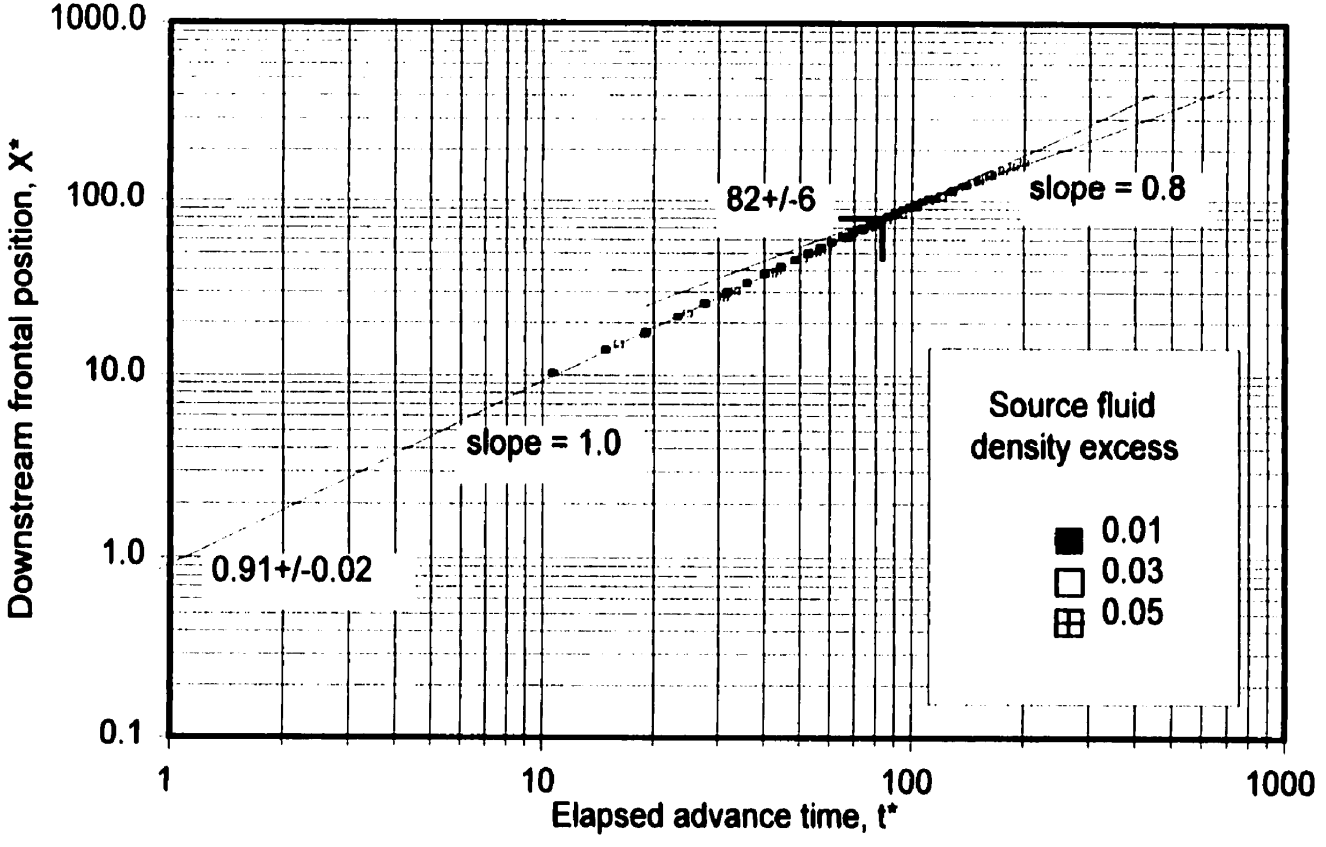

Figure 23. Log-log presentation of the normalized spread rate data for smooth-surface flows with source fluid density excesses of 0.01, 0.03 and 0.05.

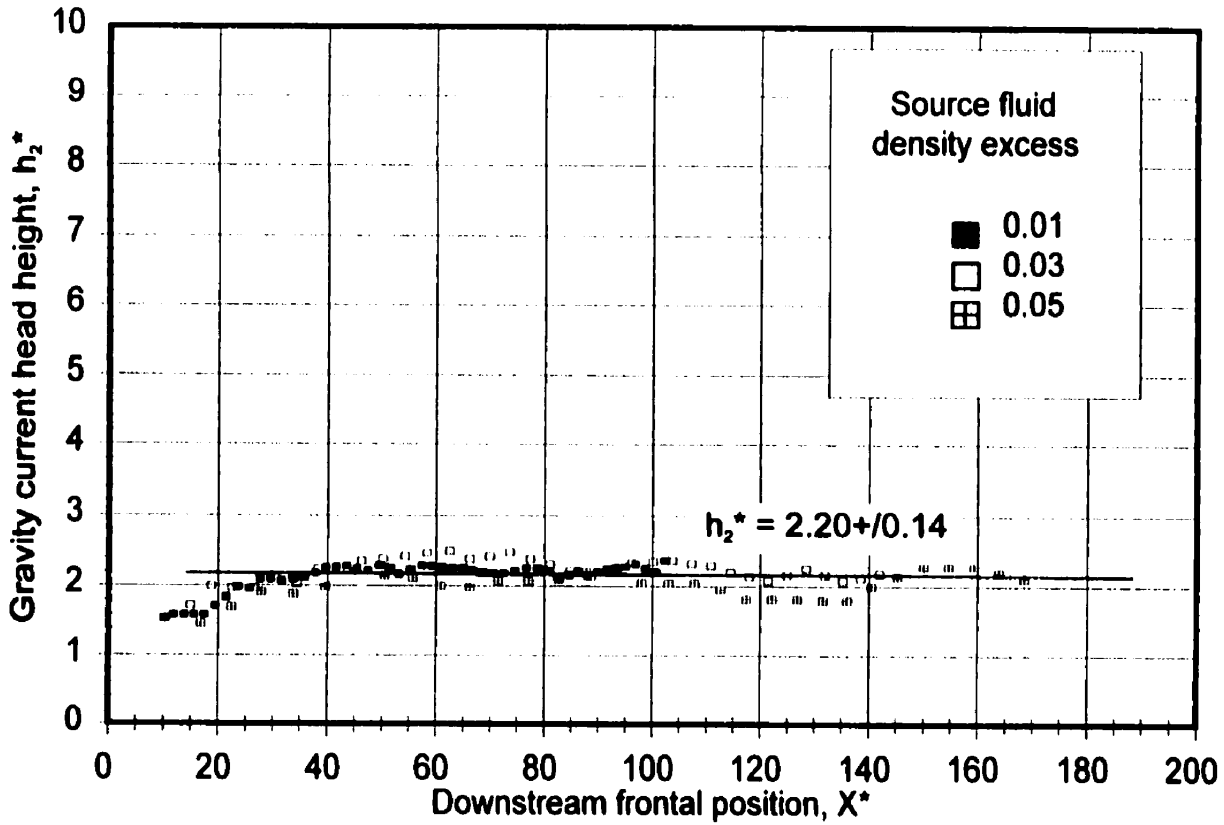

Figure 24. Downstream variation of the gravity current head height for smooth-surface flows with source fluid density excesses of 0.01, 0.03 and 0.05.

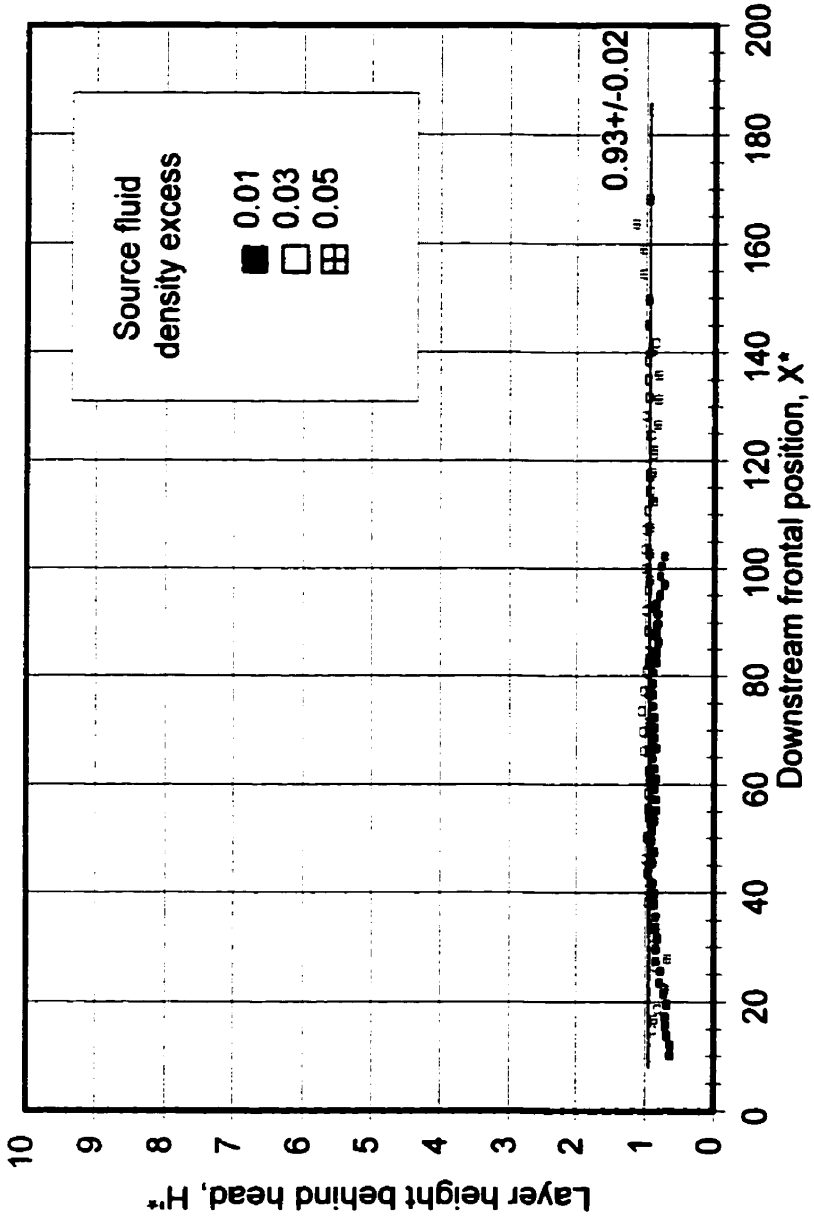

Figure 25. Downstream variation of the source layer height immediately behind the gravity current head for smooth-surface flows with source fluid density excesses of 0.01, 0.03 and 0.05.

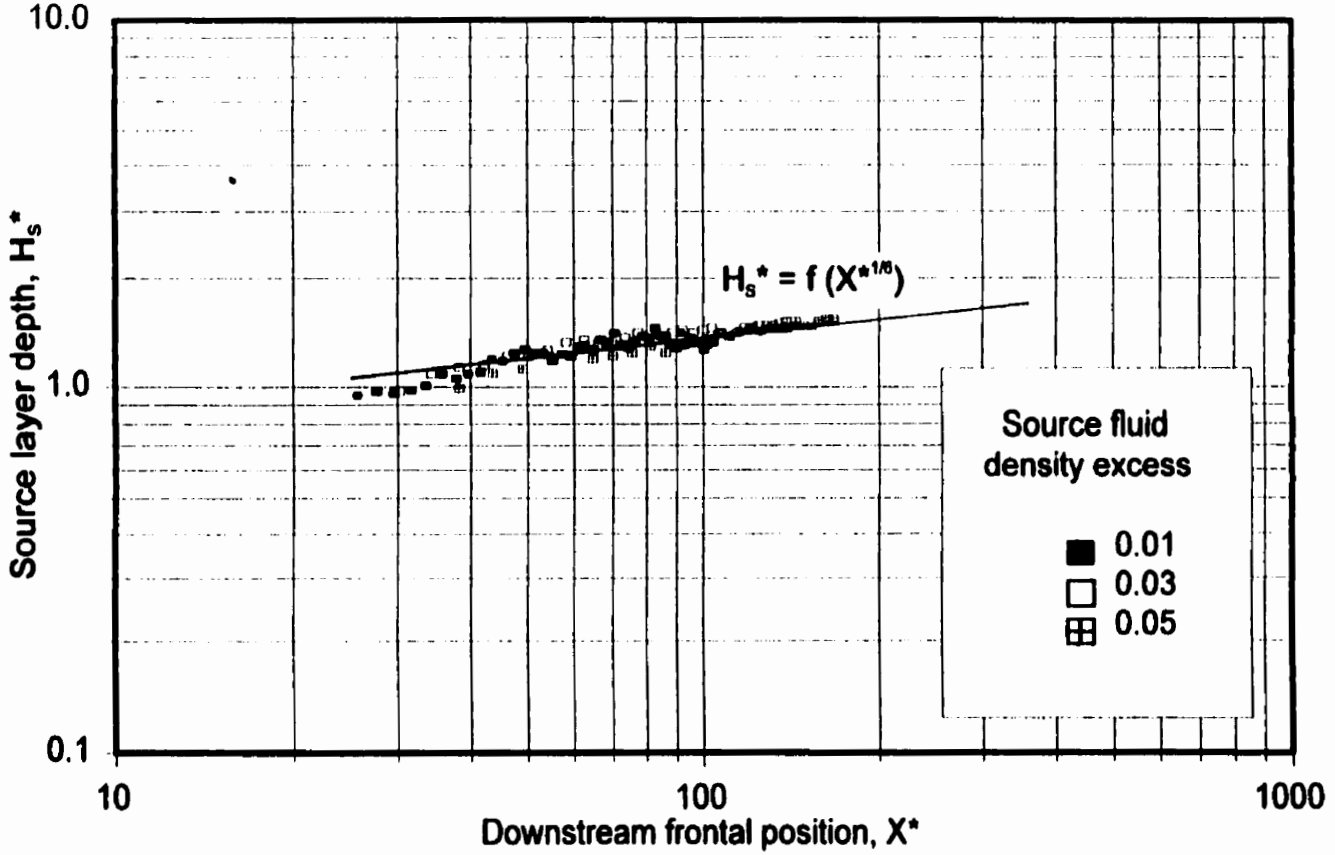

Figure 26. Variation of the source layer height measured at a fixed channel position near the inlet edge as the head progresses down the channel for smooth-surface flows with source fluid density excesses of 0.01, 0.03 and 0.05.

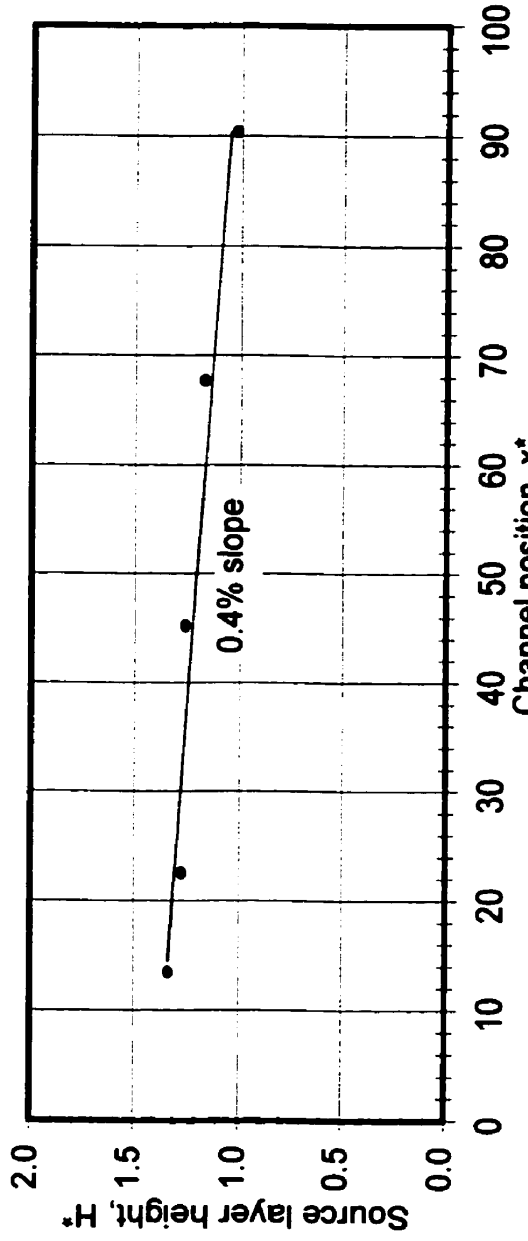

Figure 27. Profile of a gravity current source layer at time t* = 113 for a smooth-surface flow with a source fluid density excess of 0.01 and a head frontal position of X* = 100.

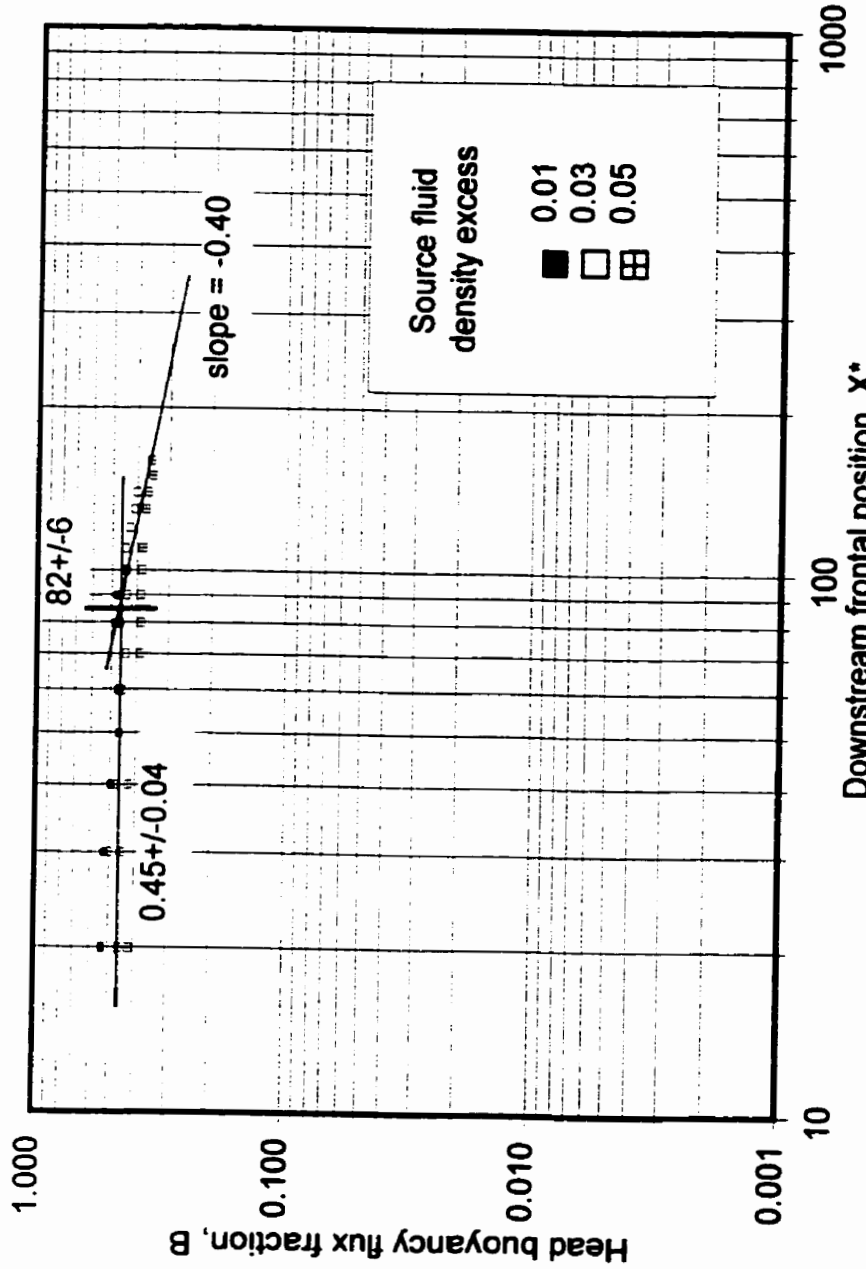

Figure 28. Variation of the gravity current head buoyancy flux fraction with downstream frontal position for smooth-surface flows with source fluid density excesses of 0.01, 0.03 and 0.05.

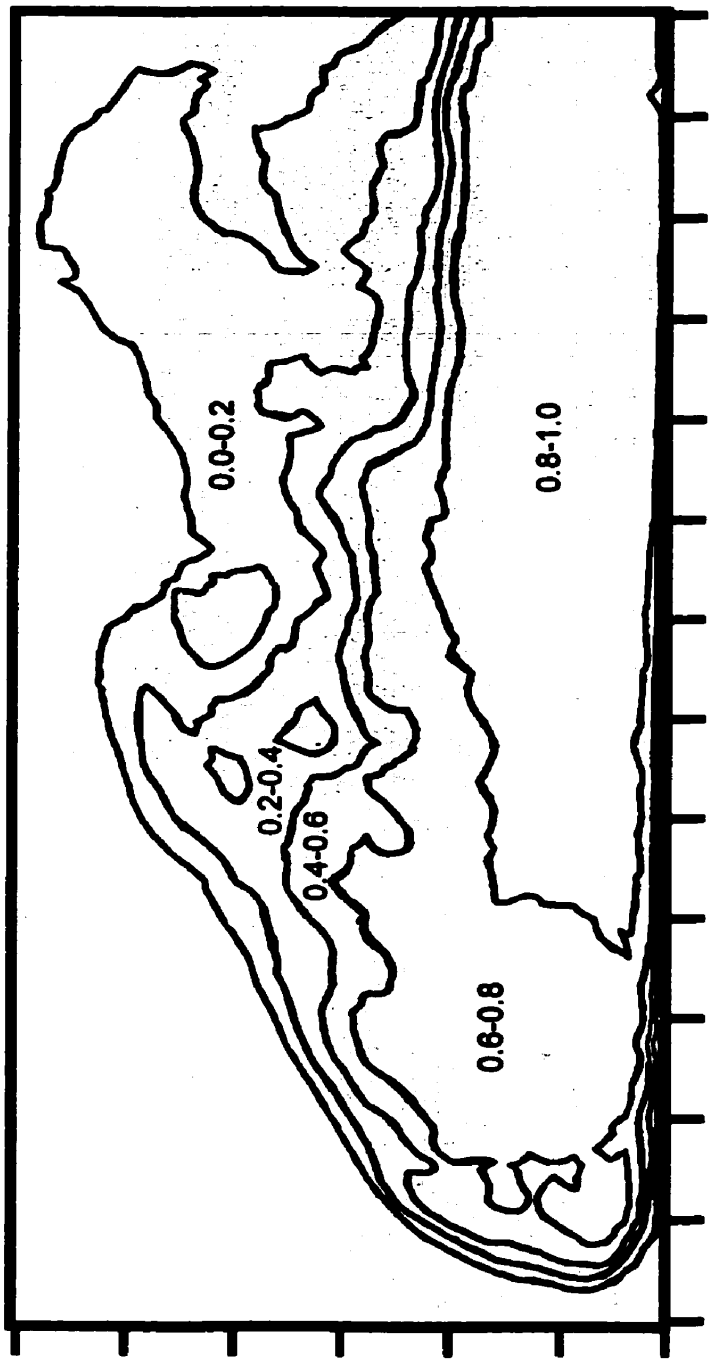

Figure 29. Typical five-contour buoyancy flux fraction profile from the present work for the head of a gravity current flowing over a smooth surface with a source fluid density excess of 0.01 and a downstream frontal position of X^*=40. (Scales are divided in 1 cm increments.)

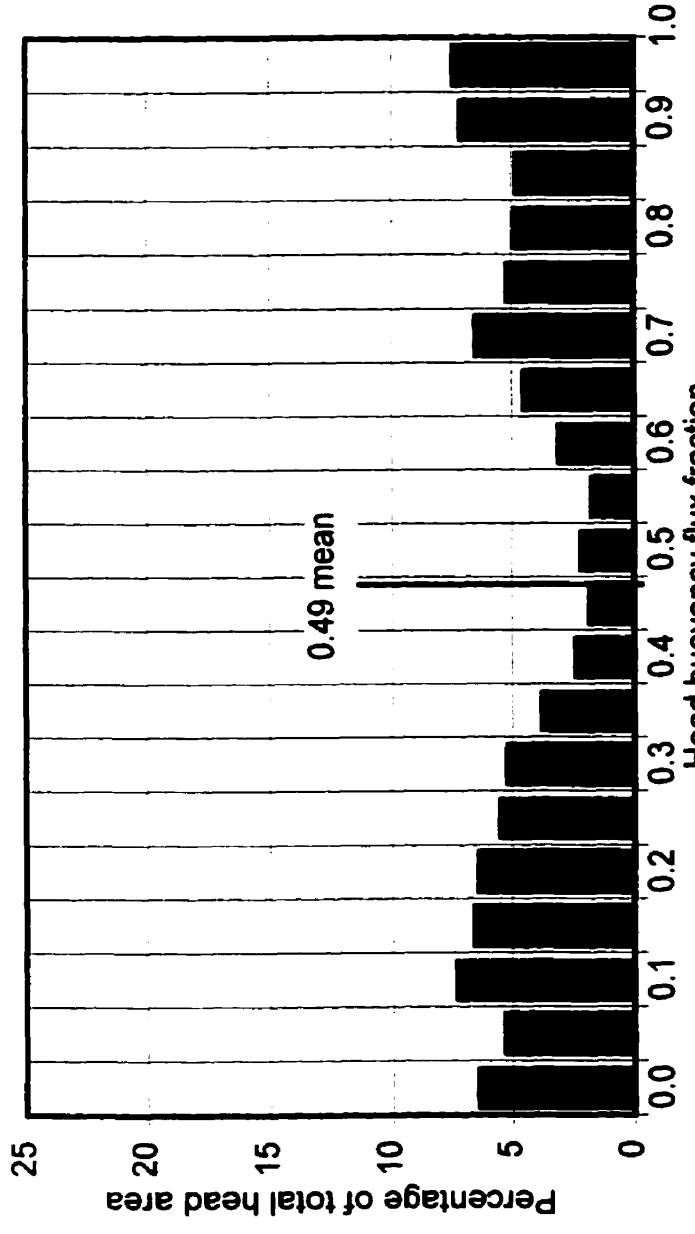

Figure 30. Typical histogram showing the percentage of total head area occupied by a particular range of buoyancy flux fraction for a smooth-surface flow with a source fluid density excess of 0.01 and a downstream frontal position of $X^*=40$.

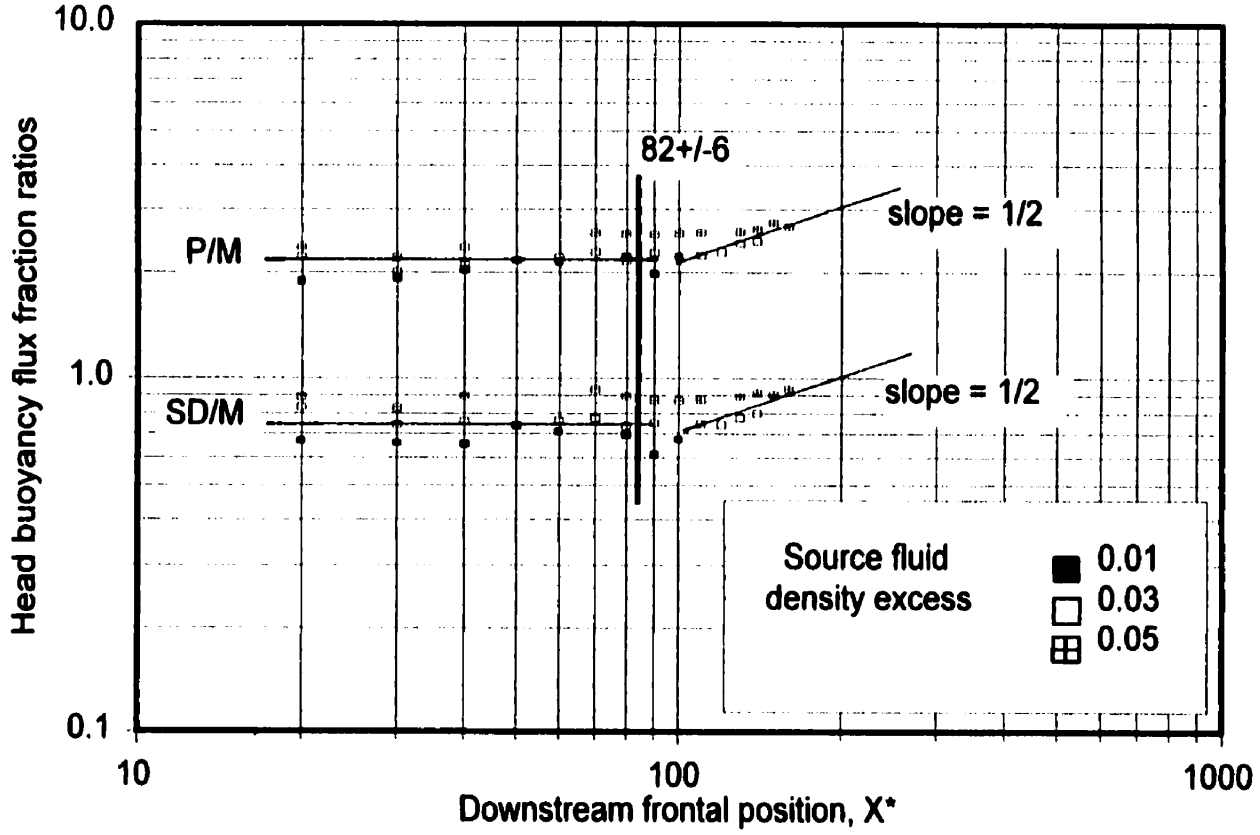

Figure 31. Variation of the peak/mean and standard deviation/mean ratios of the gravity current head buoyancy flux fraction with downstream frontal position for smooth-surface flows with source fluid density excesses of 0.01, 0.03 and 0.05.

CHAPTER 6

ROUGH-SURFACE FLOW RESULTS AND DISCUSSION

It should be emphasized, at this point, that the gravity current flow theory discussed in Chapter 5 was developed for flows over smooth surfaces only. It was not intended to apply to flows over rough surfaces such as the two-dimensional, beam-roughened surfaces used in this work. It is of interest, therefore, to determine how well, or how poorly, this smooth-surface gravity current flow theory extends to these rough-surface flows.

6.1 Experimental Results for Rough-Surface Spread Rates

The log-log plots of Figures 32 - 35 show the normalized gravity current frontal advance data for each of the rough-surface flows. In these figures, the frontal advance rate appears to be slightly dependent on the source fluid density excess, $(\Delta\rho/\rho_A)_S$, particularly for the flows over the larger roughness element scales.

It is concluded that this fluid density excess dependency increases as the surface roughness increases and can be attributed to the greater tendency for the heavier flows to fill the spaces between roughness elements as they are passed over. Figures 32-35 for the rough-surface flows should be compared to Figure 23 for the smooth-surface flows in which this fluid density excess dependency was not found to be significant.

In each of these figures, the inertial-buoyant regime is indicated by a line with a slope of unity. The y-intercept of this line at $t^*=1$ represents the initial constant frontal velocity, u_2^*, observed in the inertial-buoyant flow regime for each surface roughness. In comparing Figures 32-35, it becomes apparent that u_2^* is significantly influenced by the roughness element scale.

This dependency is shown in Figure 36 in which the roughness element scale is normalized by forming the ratio of the roughness height to the height of the source layer above the roughness element height, $h_R/(H'-h_R)$. In this figure, the initial frontal advance velocity is defined as the slope of the spread rate curve at $t^*=0$. It is observed to fall off in what appears to be a linear fashion with increasing surface roughness scale such that $u_2^*=0.91-0.14[h_R/(H'-h_R)]$.

The transition to the viscous-buoyant flow regime is also apparent in Figures 32-35 indicating that it does not occur at a fixed point but rather over a region. It appears that the downstream distance to the position where this transition begins is significantly reduced for flows over the rough surfaces in comparison to the smooth-surface flows. Figure 37 shows the observed transition position as a function of the surface roughness. Moving from the smooth-surface data to that of the smallest roughness element tests produces more than a 50% decrease in the distance to the transition position. Increasing the surface roughness to the largest scale tested further decreases this distance only slightly.

Beyond the transition regions in Figure 32-35, the slopes of the lines represent the spread rate exponents that describe the decelerations of the flows for the

viscous-buoyant spread rate equation. Recall that the smooth-surface theory presented shows that this exponent should be 0.8. Figure 38, however, shows that this exponent decreases with increasing surface roughness, falling approximately 10% over the range of roughness tested.

Three general conclusions can be drawn from the results of Figures 36-38 regarding the effects of surface roughness on gravity current spreads. First, rougher surfaces tend to decrease the initial constant frontal advance velocity of the flow. Second, they give rise to gravity currents that are dominated by viscous effects much earlier in their dispersion. Third, once viscous effects become significant, the rough surfaces tend to decelerate the flows much more quickly than the corresponding smooth surfaces.

These effects are primarily due to the increased boundary shear stresses that are associated with the rougher surface flows. Consequently, the rough-surface flow data deviates significantly from that predicted by the smooth-surface theory presented. Clearly, then, the normalized spread rate equations for smooth-surface flows are inadequate for describing flows over rough surfaces. They over-predict the advance rates and, therefore, should be re-defined to apply to a wider range of surface types.

6.2 Rough-Surface Spread Model Development

Based on observations of the video records and the results of Figures 36-38, it is concluded that the gravity current spread rate is significantly dependent on the surface roughness in both the inertial-buoyant and viscous-buoyant flow regimes. It is proposed,

then, that surface roughness affects the gravity current advance through a combination of two mechanisms, leading to reduced frontal velocities and flow deceleration.

The first is associated with the roughness elements, or rather the spaces between the elements. These spaces, in effect, facilitate an entrainment mechanism by which lighter ambient fluid is able to be introduced into the gravity current layer. The mixing of this additional ambient fluid into the gravity current layer results in a reduction in the layer's fluid density excess and, therefore, its buoyancy flux. This, then, leads to a lower frontal velocity than would have been observed for a corresponding smooth-surface flow.

The second mechanism is a function of the friction at the lower solid boundary. As expected, shear stresses between the gravity current and the floor are observed to increase with larger roughness elements and downstream position. These increased stresses result in appreciable flow deceleration. Each of these mechanisms will be discussed in detail in the following paragraphs.

Before proceeding to a rough-surface spread rate model, though, it is important to understand the model upon which the smooth-surface spread rate equations, Equations 1-5 and 1-6, are based. Figure 39 a) illustrates a very simple slab model of a gravity current layer of height, H', flowing over a smooth floor, h_R=0. The head structure is neglected in this analysis so that there is no height distinction between it and the flowing source layer. Accordingly, mixing at the head is neglected.

This is a reasonable assumption for smooth-surface flows as was concluded from Figure 28 and discussed in Section 5.4. Also, as previously indicated in Section

1.3.1., work by Simpson and Britter (1979) shows that, for smooth surfaces, the amount of ambient fluid entrained into the head, as it is overrun by the advancing layer, is very small. In addition, mixing is considered to be negligible across the upper horizontal interface between the more dense source fluid and the lighter ambient fluid where the structure is gravitationally very stable (Ellison and Turner, 1959). The vertical density profile across the layer, then, is assumed to be uniform with a mean layer density, ρ_L, equal to the source fluid density, ρ_B.

Consequently, the density of the layer is conserved as it progresses to the left in Figure 39 since no ambient fluid is entrained into it. The buoyancy flux of the layer that drives the flow, therefore, is constant with a strength equal to the source buoyancy flux. This description has been the basis for the smooth-surface flow theory presented thus far where, by Equation 1-5, the flow has a constant frontal velocity in the inertial-buoyant regime and, by Equation 1-6, the flow decelerates due to viscous effects in the viscous-buoyant regime. Based on the experimental results of Section 6.1, however, it is clear that, without modification, this theory does not extend to the rough-surface flows studied here.

The entrainment mechanism associated with the spaces between the roughness elements is described using the model illustrated in Figure 39 b). For flows over two-dimensional, square-beam roughened surfaces as presented here, analysis of the video record indicates that the gravity current tends to ride along the top of the roughness elements as pictured in Figure 40. In this model, note that the layer height,

H', is still measured from the smooth floor at y=0, however, and mixing across the upper horizontal interface is still assumed to be negligible.

Consequently, for any time, t, and position, X, there is a volume of gravitationally unstable fluid of density ρ_A that becomes trapped in the spaces between the roughness elements as the layer advances over them. This fluid subsequently mixes with the advancing layer fluid so that the layer's mean density and buoyancy flux strength decrease to levels less than those for the corresponding smooth-surface flow. Indications of the mixing between these two fluids can be observed in Figure 40 where packets of lighter fluid are observed to rise out of the roughness element spaces and into the gravity current layer. This mixing mechanism is not present in smooth-surface flows to a significant extent.

The exchange of fluid between the layer and the roughness element spaces is highlighted in Figure 41. As the heavier gravity current flows along the top of the roughness elements, some fluid at its lower boundary is sheared off by the top of the roughness elements. This heavier fluid, then, drops down the wall of the roughness element and creates a circulation within the space.

While mixing occurs within the roughness space, some of the lighter fluid is forced out to be mixed into the layer above. The video record indicates that this fluid enters the head from the roughness spaces with no initial horizontal momentum. Consequently, the horizontal momentum of the flowing layer is reduced somewhat as the mass of lighter fluid is accelerated and carried along with the flow. Eventually, the

lighter fluid trapped in the roughness spaces is observed to completely mix with the heavier layer fluid passing over the roughness array.

For a smooth-surface flow, it was concluded that it was reasonable to base the buoyancy flux of the gravity current layer on the source fluid density excess. For a rough-surface flow, however, the buoyancy flux of the layer that results from the rough-surface entrainment mechanism just described will be somewhat less than that for the corresponding smooth-surface flow. From this, a rough-surface reduced gravity term can be defined for the gravity current layer such that

$$g'' = \alpha g'_S = \alpha g\left(\frac{\Delta\rho}{\rho_A}\right)_S = \alpha g\left(\frac{\rho_B - \rho_A}{\rho_A}\right). \qquad (6\text{-}1)$$

In this relation, α is the buoyancy flux reduction factor that accounts for the decrease in the mean layer density that results from the mixing between the heavier layer fluid and the lighter ambient fluid trapped in the roughness element spaces. As previously defined, g'_S is the reduced gravity term based on the source fluid density excess. Note that this entrainment mechanism applies to both the inertial-buoyant and viscous-buoyant flow regimes.

As $g'' = \alpha\, g'_S$, it follows that the buoyancy flux reduction factor, α, is simply the ratio of the mean fluid density excess of the layer, $(\Delta\rho/\rho_A)_L$, to the source fluid density excess of the flow, $(\Delta\rho/\rho_A)_S$. Referring to Figure 39 b), the mean fluid density of the layer, ρ_L, would be the density that would result from the complete mixing of the layer fluid, ρ_B, with the ambient fluid in the roughness element spaces, ρ_A, for a given

downstream position, X. Based on the assumptiion of complete mixing and on the geometry indicated in Figure 39 (b), the following expression for α can be obtained:

$$\alpha = \left[1 + \frac{1}{2}\left(\frac{h_R}{H' - h_R}\right)\right]^{-1} = \frac{2}{2 + \left(\frac{h_R}{H' - h_R}\right)}. \qquad (6\text{-}2)$$

Note that α is simply a function of the normalized roughness element height previously used in Section 6.1 and Figures 36-38. It represents the fraction of the source fluid density excess that the gravity current layer's fluid density excess would be if complete mixing between the layer fluid and the lighter fluid trapped in the roughness element spaces were to occur. Note that for smooth-surface flows with h_R=0, α will have a value of 1 and the layer fluid density excess would be that of the source, allowing the smooth-surface flow theory to be used as described.

Figure 42 shows the dependence of α, in terms of $(1-\alpha)/\alpha$, on the normalized roughness element height, $h_R/(H'-h_R)$. As expected, the fluid density excess of the layer in a rough-surface flow is inversely proportional to the roughness scale and decreases with the greater amount of layer dilution associated with the larger roughness elements.

The second mechanism that affects the downstream flow of the gravity current is associated with the viscous-buoyant regime only and leads to flow deceleration. This behaviour is a function of the friction generated at the solid boundary between the fluid and the wall. To accurately predict the behaviour of such flows, an appropriate friction model must be incorporated into the spread rate equation. For smooth-surface flows, Equation 1-6 uses the kinematic viscosity of the fluid to account for the viscous effects

that lead to the flow deceleration in this regime. However, as concluded in Section 6.1, this model is not adequate for flows over the roughness arrays used here.

Similar to the approach used by Didden and Maxworthy (1982) to derive Equation (1-6), a rough-surface, viscous-buoyant force balance leads to a spread rate equation in which the wall shear stress must be evaluated in terms of the surface roughness. The logarithmic law for the velocity distribution in the completely-rough regime (Eq. 20.32a, Schlichting, 1979) can be used, then, to evaluate the rough wall condition, leading to a different exponent for time in the spread rate equation than was used in Equation (1-6).

The difficulty here, though, is that rough surface flows of the type studied can behave in one of two ways depending on the geometry of the roughness configuration. As described by Perry et al. (1969), these flows can fall into the category of either "k"-type or "d"-type rough wall flows, distinguished by the significant length scale involved (k is the roughness scale and d is the bulk flow scale). Consequently, extrapolation of the "law of the wall" into the roughness region becomes difficult without prior knowledge of the flow characteristics.

In either type of flow, though, Perry et al. (1969) indicate that the bulk outer flow occurs over the top of the roughness array which can then be likened to a smooth surface with a series of depressions or grooves within which the outer flow generates vortices. This flow description closely fits the flows observed in the present work such that the roughness array is, now, not submerged entirely in the gravity current flow but

rather influences the flow only in a narrow sub-layer region near the top of the roughness array.

Unfortunately, there is a lack of data from the present work to evaluate the flows in terms of "k"-type and "d"-type flows and, thus, properly extrapolate the "law of the wall". In this situation, then, the effects of the roughness on the bulk flow can be accounted for by using a modified, or "effective" fluid viscosity, ν_{EFF}, as concluded by Nikuradse (1933), allowing Equation 1-6 to be modified as follows:

$$X = k\left(\frac{g'' Q^3}{\nu_{EFF}}\right)^{1/5} t^{4/5}. \qquad (6\text{-}3)$$

Here, k is a constant, g" is the reduced gravity term modified for rough-surface flows and ν_{EFF} is the effective rough-surface viscosity. In effect, this is the equivalent fluid viscosity that will produce the same frictional effects in a smooth-surface flow that would exist in a rough-surface flow with the working fluids used here. The task, then, is to define the effective rough-surface viscosity in terms of the roughness element scale.

Newton's equation of viscosity shows that the shear stress, τ, developed in a fluid flow at a solid boundary is proportional to the local velocity gradient, du/dy, measured normal to the wall. The proportionality constant, in this case, is the fluid viscosity. The equation shows that

$$\tau = \rho\nu\frac{du}{dy}. \qquad (6\text{-}4)$$

Borrowing from the general theory for friction in a fluid flow and using dimensional analysis, it can be shown (Daugherty et al., 1985) that the shear stress is also proportional to the square of velocity. Using the mean layer velocity, U, as the appropriate velocity scale and defining the friction coefficient, c_f, as the proportionality constant, this relationship is given as

$$\tau = \rho c_f \frac{U^2}{2}. \tag{6-5}$$

Holding the two preceding expressions for shear stress equal, then, leads to a useful definition of the effective rough-surface viscosity. As a rough first approximation, the vertical velocity profile in the gravity current layer is assumed to be linear with a mean layer velocity of U such that du/dy = 2U/H with the conditions that u=0 at y=0 and u=2U at y=H. Noting that the flowrate in the gravity current layer is given by Q=UH, the effective rough-surface viscosity is, then, determined to be

$$\nu_{EFF} = \frac{c_f}{4} Q \tag{6-6}$$

from which an effective rough-surface gravity current Reynolds number would be

$$Re_{EFF} = \frac{Q}{\nu_{EFF}} = \frac{4}{c_f}. \tag{6-7}$$

A mean value of the friction coefficient can be evaluated using the work of Mills and Hang (1983) who developed an empirical expression to relate the friction coefficient to the roughness scale for fully rough flows over flat plates. The expression is given as

$$c_f = \left(2.635 + 0.618 \ln \frac{L}{k_S}\right)^{-2.57} \qquad (6\text{-}8)$$

where L is the plate length and k_s is the equivalent sand grain roughness introduced by Schlichting and discussed by Coleman et al. (1984).

The specific correlation for Schlichting's equivalent sand grain roughness for transverse square ribs, as used in this work, was developed by Donne and Meyer (1977). It is given below using symbols consistent with the present work.

$$k_S = h_R^{\left(3.4-3.7\left(\frac{s}{h_R}\right)^{-0.73}\right)}. \qquad (6\text{-}9)$$

This equation is applicable to roughness arrays in which the element pitch spacing, S/d, or S/h_R, is two, as in this work. To be dimensionally correct, the variables must be in SI units of mm.

Following this procedure, the value of h_R=0 for smooth surfaces implies that the flow is inviscid because c_f and k_s approach zero as h_R approaches zero resulting in an undefined effective Reynolds number. However, a smooth-surface friction coefficient can be found from Equation 6-6 since, for smooth surfaces, the effective viscosity should just be the viscosity of the working fluid. With this value and Equations 6-8 and

6-9, it can be shown that the effective smooth-surface roughness height required to satisfy the equations is very small compared to the roughness scales used and, therefore, can be taken as zero, i.e., h_R=0 for the smooth-surface flows.

By definition, the effective rough-surface Reynolds number is a function of the effective rough-surface viscosity and, by Equations 6-7, 6-8 and 6-9 above, an indirect function of the surface roughness scale. As shown in Figure 43, the effective rough-surface Reynolds number varies with the surface roughness scale according to a -1/3 power dependence. Accordingly, the effective rough-surface Reynolds number for the largest roughness scales is less than a third of the smooth-surface value of 1000.

With this effective rough-surface viscosity approach and the modified definition of the reduced gravity term for rough-surface flows, Equation 6-3 can be used to model the spread rate in the viscous-buoyant regime for rough-surface flows as studied here. In agreement with traditional theory, then, flows over rougher surfaces with increased shear stresses can be treated in a manner similar to higher viscosity, lower Reynolds number flows over smooth surfaces.

6.3 Normalization of Rough-Surface Spread Rate Data

It should be re-stated, at this point, that the normalization of all data, thus far, was done using the characteristic scaling parameters developed for smooth-surface flows described in Section 1.3.1. These parameters are a function of the reduced gravity term, g'_s, which is based on the source fluid density excess of the flow and the constant source flux rate, Q, only and do not account for surface roughness effects.

Consequently, it is necessary to develop a new normalization method for rough-surface gravity current flows using the effective viscosity approach just developed.

An appropriate method is one already used by Chen (1980) in which the characteristic length and time scales are similar to those already defined but which incorporate the gravity current Reynolds number to account for viscous effects. Chen defined these scales as $R_1=d_{REF}Re$ and $t_1=t_{REF}Re$ for length and time, respectively. For this work, however, these scales are re-defined as d_R and t_R with $u_R=d_R/t_R$ such that

$$d_R = d'_{REF}\,Re_{EFF} = \frac{d_{REF}\,Re_{EFF}}{\alpha^{1/3}} \tag{6-10}$$

$$t_R = t'_{REF}\,Re_{EFF} = \frac{t_{REF}\,Re_{EFF}}{\alpha^{2/3}} \tag{6-11}$$

$$u_R = u'_{REF} = \alpha^{1/3}\,\frac{d_{REF}}{t_{REF}} = \alpha^{1/3}\,u_{REF}. \tag{6-12}$$

Note that d'_{REF}, t'_{REF} and u'_{REF} are now based on the rough-surface reduced gravity term, g", and the Reynolds number is the effective rough-surface Reynolds number. Parameters normalized with these scales are indicated by the superscript **. Thus,

$$X^{**} = \frac{X}{d_R} = \frac{\alpha^{1/3}\,X}{d_{REF}\,Re_{EFF}} \tag{6-13}$$

$$t^{**} = \frac{t}{t_R} = \frac{\alpha^{2/3}\,t}{t_{REF}\,Re_{EFF}} \tag{6-14}$$

$$u_2^{**} = \frac{u_2}{u_R} = \frac{u_2}{\alpha^{1/3} u_{REF}} \tag{6-15}$$

6.4 Influence of Roughness on Spread Rates

Based on the rough-surface model developed here, the spread rate equations, in dimensional form, for the inertial-buoyant and viscous-buoyant flow regimes, respectively, become

$$X = C \alpha^{1/3} (g'_S Q)^{1/3} t \tag{6-16}$$

$$X = k \alpha^{1/5} \left(\frac{g'_S Q^3}{\nu_{EFF}} \right)^{1/5} t^{4/5} \tag{6-17}$$

Note that for smooth-surface flows, $\alpha = 1$ and $\nu_{EFF} = \nu$, reducing the equations to the smooth-surface forms introduced in Section 1.3.1. In addition, note that the buoyancy flux reduction factor, α, applies to both flow regimes while the effective viscosity term appears only for the viscous-buoyant flow regime. In normalized form, these equations become

$$X^{**} = C t^{**} \tag{6-18}$$

$$X^{**} = k t^{**4/5}. \tag{6-19}$$

The spread data from all tests, previously presented in Figures 32-35, is re-plotted in Figure 44 using the new rough-surface normalization procedure developed

here. It is shown to collapse well onto a single curve, highlighting the eventual deceleration of the flow in the viscous-buoyant regime. The slope of this curve at $t^{**}=0$ is the normalized frontal velocity, or Froude number, for the inertial-buoyant flow regime and yields a value of $u_2^{**}=0.90+/-0.04$. This is the constant C in the previous equations and agrees quite well with the value observed for the inertial-buoyant regime of the smooth-surface flows presented in Section 5.1 indicating that, for a brief time, boundary shear stresses in the rough-surface flows are not yet a significant factor.

The log-log plot of Figure 45 shows the functional dependence of X^{**} on t^{**}. As expected, initially the slope is unity and the flows exhibit the constant-velocity characteristic of the inertial-buoyant regime. It is clear from this figure that a deviation from the constant velocity flow appears to occur at $X^{**}=0.09$ and $t^{**}=0.10$. This is the beginning of the transition region to the viscous-buoyant regime. For the smooth-surface flows in which $Re_{EFF}=1000$ and $\alpha=1$, this transition would be about $X^{*}=90$ which agrees well with the value of 88 previously reported by Chan et al. (1993).

Eventually, the slope of the data on the log-log plot tends to a value of 4/5 for the viscous-buoyant regime in which flow deceleration is prominent. This 4/5 power dependence of frontal position on the advance time agrees with the theory presented here and by the authors previously mentioned. Work by Didden and Maxworthy (1982) concludes that the spread rate constant, k, for the viscous-buoyant flow regime is about 0.73. Interpretation of Figure 45 shows that this constant has a somewhat lower value of 0.6 for the present rough-surface experiments.

This new rough-surface model extends the previously presented smooth-surface theory to account for 1) the fluid exchange and mixing between the lighter fluid in the roughness element spaces and the heavier current fluid and 2) the increased boundary shear stresses caused by the larger roughness scales. The collapse of the data in Figures 44 and 45 confirms that this approach provides a reasonable description of the rough-surface flow dynamics.

6.5 Influence of Roughness on Layer Heights

As indicated in Figures 40 and 41 and in the video record, the gravity current tends to flow along the top of the roughness elements such that the roughness array constitutes a smooth raised floor with rectangular troughs situated across the flow path. In effect, then, it adds an offset to the head and layer height data equal to the roughness element height. Recalling that h_2 and H' are measured in an upwards direction with y=0 at the smooth-surface floor, the height data is reduced by the roughness element height so that the variation of (h_2-h_R) and $(H'-h_R)$ with X can be examined. In this manner, the head and layer heights observed in rough-surface flows can be more appropriately compared to those of the smooth-surface flows.

Figures 46 and 47 show the downstream trends of the gravity current head and layer heights. In these presentations, the rough-surface model described in Sections 6.2 and 6.3 is used to normalize both the height and downstream position data. Although the figures indicate that the head and layer heights become independent of the downstream position after some initial growth region, a strong variation in these heights

with the surface roughness scale can be observed. From these figures, it can be seen that both the head and layer heights increase with increasing surface roughness.

The rough-surface model, however, was developed primarily to account for surface friction as it affects the downstream travel and, to a lesser extent, to account for the layer dilution associated with the entrainment into the layer of the lighter fluid trapped in the roughness element spaces. Consequently, it may not be appropriate to normalize vertical scales using the characteristic rough-surface length scale, d_R, as was done in Figures 46 and 47. Alternatively, normalization of the height data is done using only the intermediate characteristic scale, d'_{REF}, which accounts only for the additional layer dilution. The downstream position, however, is normalized using d_R and presented as X^{**}.

Accordingly, plots of $(h_2-h_R)/d'_{REF}$ and $(H'-h_R)/d'_{REF}$ versus X^{**} are presented to describe the head and layer heights for flows over all surfaces. Note that for smooth-surface flows with $\alpha=1$ and $h_R=0$, the scaling parameter, d'_{REF}, becomes d_{REF} and the plots reduce to the results shown in Figures 24 and 25 presented in Section 5.2 for h_2^* and H'^* versus X^*. Figures 48 and 49 give the gravity current head and layer heights as a function of the downstream frontal position for all tests performed in this study.

It was shown for the smooth-surface flows that these heights quickly reach a steady state value and remain essentially unchanged as the structure moves down the channel. Results presented in Figures 48 and 49 show the same to be true for flows over the two-dimensional, square-beam roughened surfaces used in the present work.

After an initial growth period during the first 25% of the channel, the head and layer heights reach stable values.

The data of Figure 48 appears to collapse with two distinct values of $(h_2-h_R)/d'_{REF}$. The smooth-surface tests indicate a value of 2.20+/-0.14, which agrees with the earlier results of Figure 24, while the rough-surface data leads to a value of 2.83+/-0.19. The scatter of the rough-surface data about its mean value is less than about 10% which is significantly less than the 30% increase in the mean values observed when the smooth and rough-surface data are compared.

It is observed that this roughness effect is much more noticeable when the smooth and rough-surface data are compared than when the rough-surface data alone is considered. Accordingly, all of the rough-surface data is assumed to collapse with a single value. The jump in head height, $(h_2-h_R)/d'_{REF}$, due to the rough surfaces, then, is considered to be the result of an increase in entrainment near the leading edge of the gravity current head which induces additional mixing as the nose interacts with each roughness element.

In Figure 49, the height of the layer immediately behind the head, $(H'-h_R)/d'_{REF}$, shows no dependence on the surface roughness condition. The data for all tests collapses very well with a value of 0.95+/-0.06 which is very close to the value of 0.93 indicated in Figure 25 for smooth-surface flows alone. Further, there is no indication with this data that there is a distinct change from smooth to rough-surface flows as was seen with the head height data.

In fact, the layer height should not be expected to increase with increasing surface roughness as used here. Consider an open system, control volume in the gravity current layer located just behind the head that moves with the head. This volume is defined by two lateral cross-sections, the bottom solid surface and the upper interface between the layer and the mixed fluid above it. Accordingly, a net positive flux of fluid into this volume would be required to produce a growth in the layer height.

The flowrate into and out of the cross-sections can be assumed to be the same as long as the sections are relatively close to one another so that there is no net volume of fluid added by this mechanism. Any mixing between the layer fluid and the fluid in the roughness element spaces affects only the density and not the volume of the fluid in the control volume. Consequently, any increase in layer height must be the result of entrainment of fluid across the upper surface of the control volume. As previously presented, however, mixing across this surface is assumed to be negligible (Ellison and Turner, 1959).

As noted earlier, the shape of the gravity current head can be described by the ratio of the head height to the height of the layer immediately behind the head. For smooth surfaces with h_R=0, this ratio was determined to be 2.38 based on the experimental results reported in Section 5.2. This shape parameter increases to 3.0+/-0.19 for the rough-surface data presented here. Figure 50 shows the influence of the surface roughness scale on this shape parameter indicating, once again, that there is a noticeable difference in flow geometry between smooth and rough-surface flows that does not appear when only the rough-surface data is considered.

Measurements of the growth of the gravity current layer height at fixed channel positions, such as near the inlet edge, were not made for the rough-surface flows. The results of measurements for the smooth-surface flows as presented in Figures 26 and 27, however, are assumed to be typical of flows over rougher surfaces. Recall the explanation for the layer growth near the source given in Section 5.2. The increased frictional resistance induced by greater roughness element scales would require a more rapid layer growth near the source to create sufficient static pressure head to drive the flow. Accordingly, the interface between the current layer and the mixed fluid above it would be sloped down toward the head.

6.6 Influence of Roughness on the Gravity Current Froude Number

Recalling the plot of u_2^* versus X^* in Figure 22, the Froude number adopted for smooth-surface flows is based on a normalization of the frontal velocity using the characteristic velocity scale, u_{REF}. Using the same smooth-surface normalization method, this same data is plotted once again in Figure 51 along with the rough-surface spread rate data. It can be seen that the initial normalized frontal velocity decreases and the transition to the viscous-buoyant regime occurs much earlier for rougher surfaces. It is clear from this figure, then, that the smooth-surface model does not extend to rough-surface flows without modification.

The spread rate data, u_2^{**} versus X^{**}, for all tests is presented in Figure 52 using the rough-surface normalization procedure developed earlier. Again, note that the normalized frontal velocity is, in fact, the Froude number adopted for this work. Its

definition is based on the rough-surface characteristic velocity scale, $u_R=u'_{REF}$, which is a function of the reduced gravity term, g", such that

$$Fr = \frac{u_2}{u_R} = \frac{u_2}{u'_{REF}} = \frac{u_2}{(g'' Q)^{1/3}} = u_2^{**} \qquad (6\text{-}20)$$

$$g'' = \alpha g'_S = \alpha g \left(\frac{\Delta\rho}{\rho_A}\right)_S. \qquad (6\text{-}21)$$

The frontal velocity data of Figure 52 collapses quite well using the rough-surface normalization procedure developed in Section 6.2 and 6.3. Over the downstream extent of the flows, the inertial-buoyant, transition and viscous-buoyant regimes are evident. During the constant frontal velocity flow, the Froude number is observed to be constant with a value of 0.91+/-0.04 which is consistent with previous presentations. The Froude number for this regime, then, is a very good predictor of the frontal velocity over the range of surface roughness (including smooth-surface flows) and fluid density excess considered.

The inertial-buoyant/viscous-buoyant transition region begins at about $X_t^{**}=0.09$ in agreement with Figures 44 and 45. Beyond this region, the frontal velocity decreases due to the increasing viscous effects that now govern the flow as it progresses down the channel. Based on the viscous-buoyant spread rate equation given in Section 6.4, it can be shown that the flow deceleration should occur such that $u_2^{**} = f\,(X^{**})^{-1/4}$. The data of Figure 52 for the viscous-buoyant regime from all the tests is observed to agree quite well with this downstream rate of deceleration.

6.7 Downstream Mixing in Rough-Surface Flows

It was concluded in Section 5.4 that dilution of the gravity current head for smooth-surface flows was relatively small as it travelled down the channel length. Recalling Figure 28, it can be seen that the head buoyancy flux fraction, and, thus, the mean head fluid density excess, falls less than 20% from its initial value over the length of the channel. The majority of this decrease is observed to occur after the flow has passed into the viscous-buoyant regime where shear stress effects at the lower solid boundary become significant.

As indicated in Figure 28, once viscous effects become significant in the smooth-surface flows, the buoyancy flux fraction is observed to fall off in accordance with a power law such that $B = m\,(X^{**})^{n}$. In this relation, m is a constant representing the y-intercept of the relation and n is the power law exponent, or the downstream viscous-buoyant dilution rate exponent. The parameter, n, represents the rate at which the head buoyancy flux fraction decreases with downstream frontal position and is a measure of the downstream dilution rate of the head. This power law dependence is found to exist for the rough-surface flows, as well.

Plotted on linear scales, the downstream dilution data for each test decreases asymptotically to some minimum value. On logarithmic scales, the data is linearized such that the y-intercept at $X^{**}=1$ is 10^{m} and the slope of the line is given by

$$n = \frac{\Delta[\log(B)]}{\Delta[\log(X^{**})]}. \qquad (6\text{-}22)$$

The smooth-surface data for downstream mixing is presented, once again, in Figure 53 where the downstream frontal position, X^{**}, is now normalized using d_R. The constant, m, and dilution rate exponent, n, are indicated on the figure. Linear regressions of the logarithmic smooth-surface data in the viscous-buoyant regime reveai that m varies by less than 10% and n varies by less than 3% for the range of fluid density excesses used. As concluded in Section 5.4. for smooth-surface flows, the influence of the source fluid density excess on the downstream mixing is insignificant over the range tested.

Figures 54-57 give the same data for each of the rough-surface flows. In these figures, however, it is clear that the downstream dilution is strongly influenced by the source fluid density excess. In general, it can be seen that the rate at which the head buoyancy flux fraction decreases with downstream frontal position can increase by as much as 50% when the source fluid density excess is increased from 0.01 to approximately 0.03-0.05.

These figures and the linear regressions of the data for each of the rough-surface cases show that there is a significant distinction between the 0.01 fluid density excess tests and the 0.03 and 0.05 fluid density excess tests. Overall, the y-intercept, m, for the 0.03 and 0.05 fluid density excess tests varies less than 20% about the mean value while the dilution rate exponent, n, varies less than 10% for the same tests. In contrast, m decreases by more than 60-80% while n increases by more than 60-80% when the fluid density excess used is increased from 0.01 to the range of 0.03-0.05.

The data, therefore, indicates that a transition in the downstream mixing behaviour must occur somewhere between source fluid density excess values of 0.01 and 0.03. As Figures 54-57 indicate, further increases in the source fluid density excess above this transition value lead to relatively small and insignificant increases in the overall downstream mixing for the same surface roughness scale. Accordingly, these figures show the values of the parameters, m and n, for the 0.01 fluid density excess tests and for the data of the 0.03 and 0.05 fluid density excess tests considered together. No distinction is made between the data for the 0.03 and 0.05 fluid density excess tests.

The data of Figures 54-57 is replotted in Figures 58 and 59 showing the 0.01 fluid density excess tests and the 0.03 and 0.05 fluid density excess tests, respectively. Once again, no distinction is made in Figure 59 between the data for the 0.03 and 0.05 fluid density excess tests. For each test, the parameters, m and n, are summarized on the figures. In general, these figures indicate that the downstream reduction in the head buoyancy flux fraction is only slight during the inertial-buoyant phase of the flows. Beyond the transition point and into the viscous-buoyant regime, however, the decrease in the value of this parameter is quite substantial for each of the surface roughness scales.

Figure 59, for instance, indicates that the mean fluid density levels in the head region of the flow reach levels as low as only 0.05% greater than that of the surrounding ambient fluid. Surprisingly, though, as observed in the video record, the general structure of the head remains intact even for dilution levels as great as this. Figure 58

indicates that, for the roughest surfaces tested, the downstream dilution rate is as much as 3 times greater than that for the corresponding smooth-surface flow with a 0.01 source fluid density excess. For the flows with a 0.03-0.05 source fluid density excess, Figure 59 shows that the dilution rate is as much as 4.5 times greater.

It is apparent from these figures that surface roughness significantly affects the downstream rate at which the gravity current head is diluted and, thus, the rate at which the head buoyancy flux fraction is diminished. Accordingly, to represent this influence, a viscous-buoyant rough-surface mixing ratio, θ_R, is defined to quantify the mixing associated with a particular surface roughness scale relative to that associated with the corresponding smooth-surface flow. This rough-surface mixing ratio is defined as

$$\theta_R = \frac{n_{ROUGH}}{n_{SMOOTH}} \qquad (6\text{-}23)$$

where n is the previously defined dilution rate exponent.

Figure 60 shows this mixing ratio as a function of the normalized surface roughness scale, $h_R/(H'-h_R)$, for flows with a 0.01 source fluid density excess and for flows with a 0.03-0.05 source fluid density excess. For each case, the data is represented by a linear relation such that the ratio has a value of one for smooth-surface flows and increases with increasing surface roughness scale. In agreement with previous results, the value of this mixing ratio is greater for the heavier gravity current flows.

As previously noted and as observed from Figure 60, the downstream dilution rate is significantly dependent on the source fluid density excess for values in the order of 0.01 and up to approximately 0.03. Beyond this value, further increases in the fluid density excess appear to have little effect on the dilution of the head. In addition, this fluid density excess dependence is magnified for the rougher surfaces.

As noted in Section 6.1, this effect can be attributed to the greater tendency for the heavier flows to fill the spaces between roughness elements as they are passed over, increasing the amount of lighter ambient fluid entrained into the head region. Recall Figures 40 and 41 which highlight the interaction between the heavy current fluid and the lighter ambient fluid trapped in the spaces between the roughness elements as the two mix.

The primary effect on the gravity current flow due to increasing the surface roughness scale is to increase the friction at the lower solid boundary. As the friction, and, thus, the shear stress, grows with downstream position, the rough-surface boundary layer gets thicker as it flows over the surface roughness elements. This growing layer thickness, then, causes more dense fluid to be turned back in the no-slip layer near the roughness elements. Consequently, the flux of dense fluid into the head is reduced and less of it is available to mix with and balance the flux of incoming ambient fluid.

In addition to this effect, the entrainment of lighter ambient fluid into the head is significantly increased, as the fluid trapped in the roughness element spaces is entrained by the head as it passes over. This effect, combined with the greater

boundary layer thickness, leads to a reduction in the dense fluid supplied to the head and an increase in the ambient fluid entrained at the lower solid boundary. Under these conditions, the system is no longer able to maintain a steady state buoyancy flux fraction as it progresses down the channel. Note that these effects are not observed in the smooth-surface flows.

Further quantification of the surface roughness influence on the downstream gravity current head dilution rate can be expressed in terms of the downstream distance, $X_{50\%}$, at which the head buoyancy flux fraction falls to 50% of its initial value. For each surface roughness scale tested, the ratio of the rough/smooth-surface channel positions at which the buoyancy flux fraction falls to this value is given in Figure 61. This ratio is defined as

$$(X_{50\%})_R = \frac{(X^{\bullet}_{50\%})_{ROUGH}}{(X^{\bullet}_{50\%})_{SMOOTH}} \qquad (6\text{-}24)$$

where the downstream distances are normalized using d_R.

The data presented in Figure 61 shows that this distance ratio decreases as the surface roughness scale increases in accordance with a power law relation. Linear regression of the data, in logarithmic form, reveals that the power law exponent for this relationship is approximately -1/4 for the data recorded. Accordingly, the data shows that the gravity current head experiences much greater mixing with the ambient fluid for flows over rougher surfaces. In addition, this surface roughness effect is increased for the heavier flows.

For the largest surface roughness scales used and a source fluid density excess of 0.01, the observed distance required for the head buoyancy flux fraction to fall to half of its initial value is approximately 40% of that for the corresponding smooth-surface flow. For the 0.03-0.05 fluid density excess tests, the distance required is approximately 28% of that for the corresponding smooth-surface flow. The constants for the power law relations show that the distance required in the heavier flows is approximately 25% less than that observed in the 0.01 fluid density excess tests.

Figure 62 shows profiles of the buoyancy flux fraction in a gravity current head for three downstream positions (X^{**}=0.083, 0.188, 0.292) for a flow with a source fluid density excess of 0.01 and a normalized roughness scale, $h_R/(H'-h_R)$ of 0.83 (h_R=1.9 cm). The flow is moving to the left with an initial frontal advance velocity of 3.7 cm/s and decelerates to about 3.0 cm/s near the end of the channel. The head height above the roughness element array is approximately 7 cm.

The profiles illustrate the typical behaviour of the current - flowing along the top of the roughness element array. The roughness elements are not apparent in these figures because the profiles are derived from time-averaged images. It is apparent, though, that the mean buoyancy flux fraction in the head drops very rapidly as the head progresses down the rough-surface channel.

The histograms in Figures 63 (a), (b) and (c) are a measure of the spatial distribution of the buoyancy flux fraction over the entire head area for each of the three profiles of Figure 62. In each of the distributions, which are found to be typical of the rough-surface flows considered in this work, the mean head buoyancy flux fraction and

the percentage of total head area represented by a particular level of buoyancy flux fraction are indicated. As observed in Figures 53-59, these histograms illustrate the trend of decreasing mean head buoyancy flux fraction with increasing downstream frontal position due to greater dilution with the ambient fluid.

The downstream trends of the peak/mean and the standard deviation/mean ratios of the head buoyancy flux fraction are given in Figures 64 and 65, respectively. Overall, the peak/mean ratios are seen to increase with downstream position, especially after the flow has passed into the viscous-buoyant regime, due to a downstream decrease in the overall mean fluid density excess in the head. The standard deviation/mean ratios, however, remain reasonably steady as the current moves downstream. Closer examination of these figures shows that, in general, these ratios increase as the surface gets rougher and as the source fluid gets heavier.

Figure 64 indicates that local values of the head buoyancy flux fraction can be as high as five times the mean values. Figure 65 shows that there is a significant spatial variation in the local values of buoyancy flux fraction within the gravity current head. Variations as much as 50-100% of the mean values are evident within the head structure. These figures show that the mean head buoyancy flux fraction is not a sufficient predictor for local values.

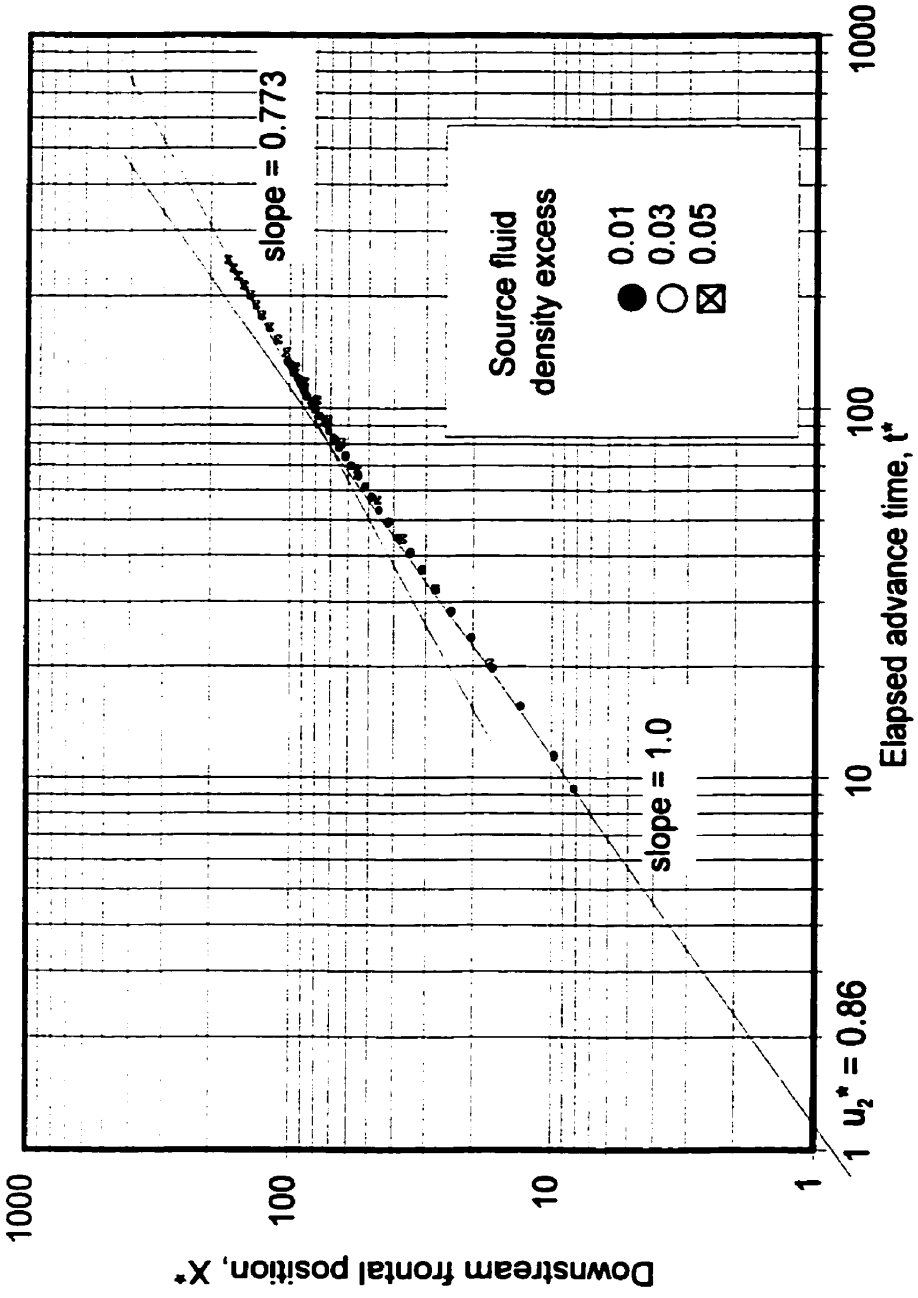

Figure 32. Normalized presentation of the spread rate data for rough-surface gravity current flows with a roughness element height of 6 mm and source fluid density excesses of 0.01, 0.03 and 0.05.

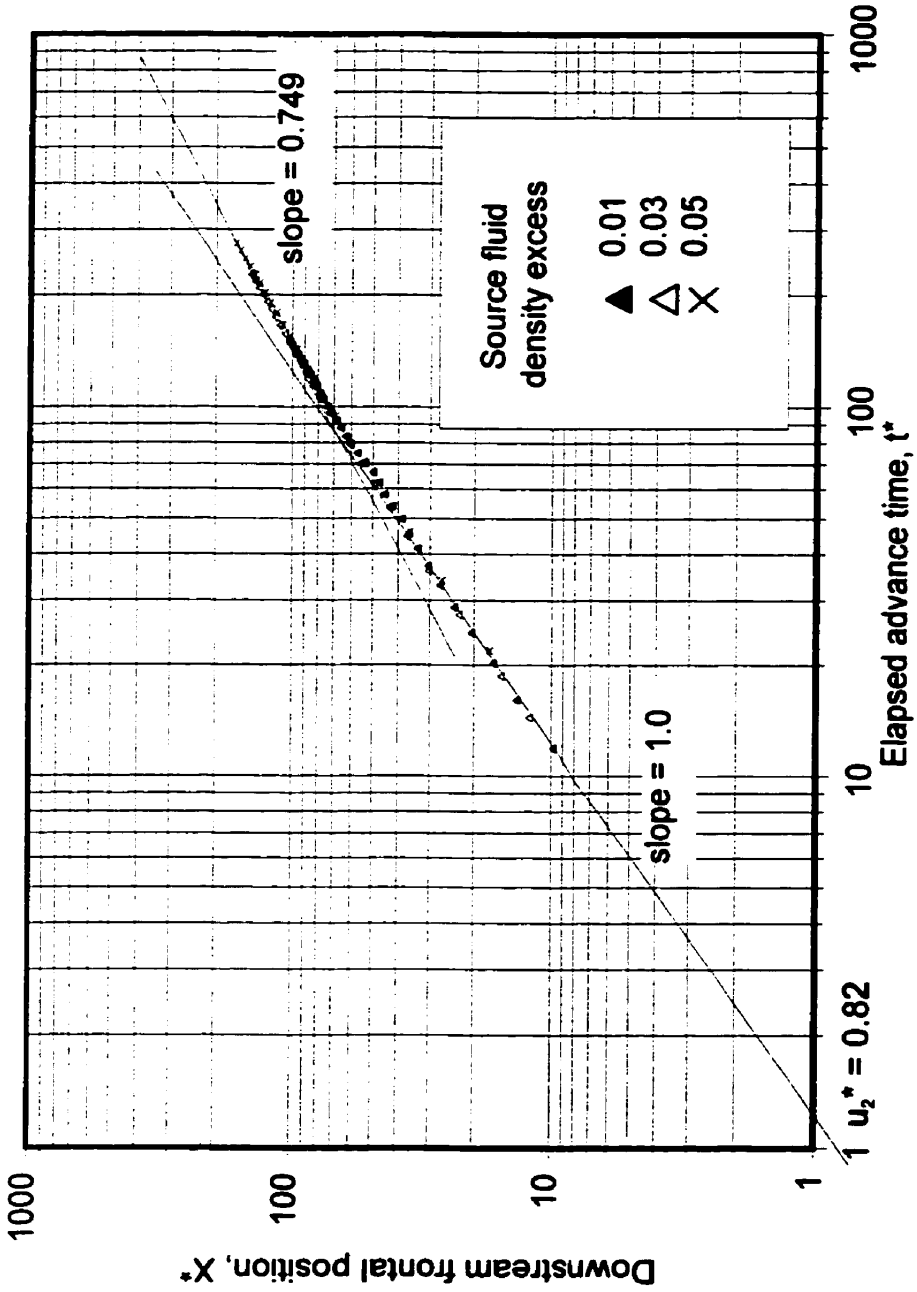

Figure 33. Normalized presentation of the spread rate data for rough-surface gravity current flows with a roughness element height of 13 mm and source fluid density excesses of 0.01, 0.03 and 0.05.

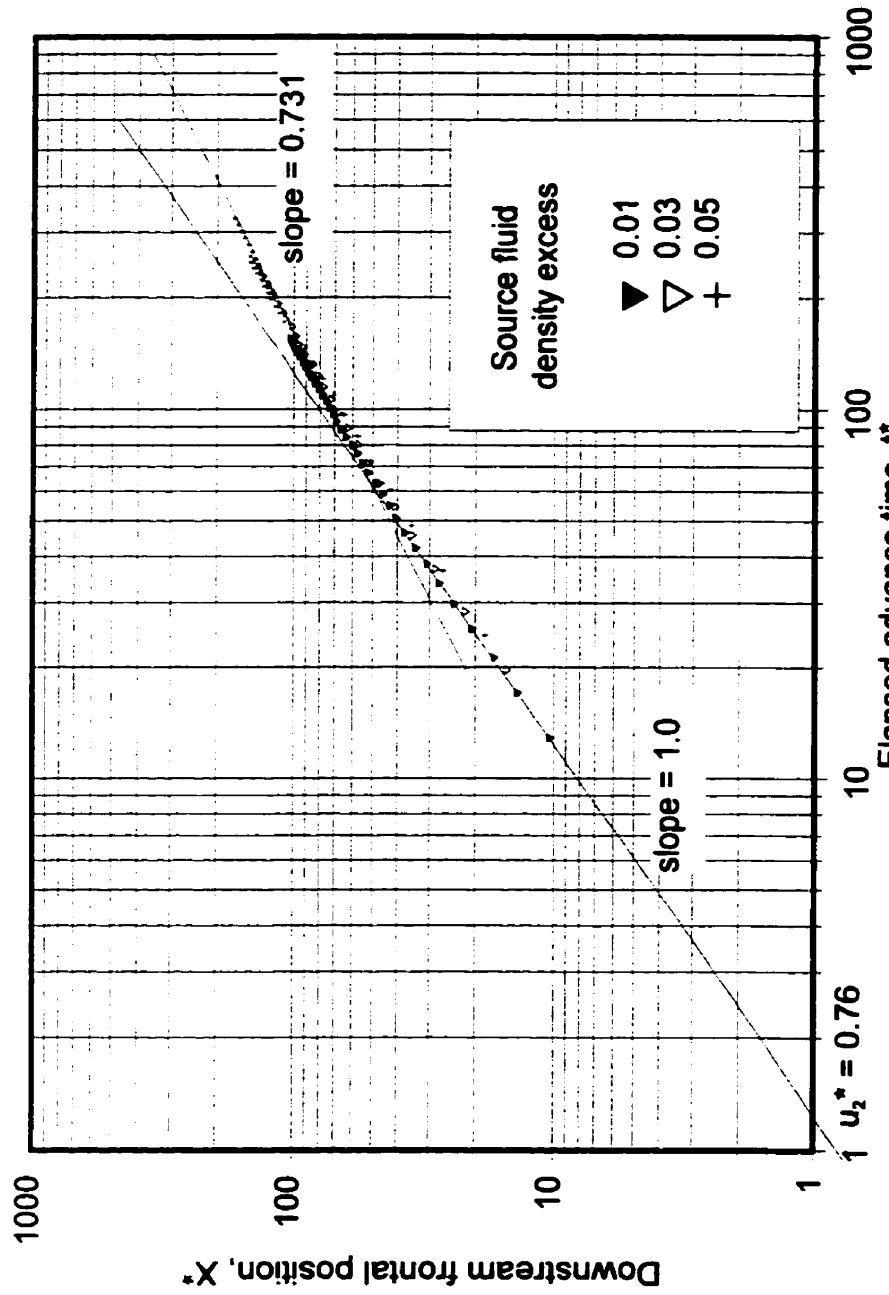

Figure 34. Normalized presentation of the spread rate data for rough-surface gravity current flows with a roughness element height of 19 mm and source fluid density excesses of 0.01, 0.03 and 0.05.

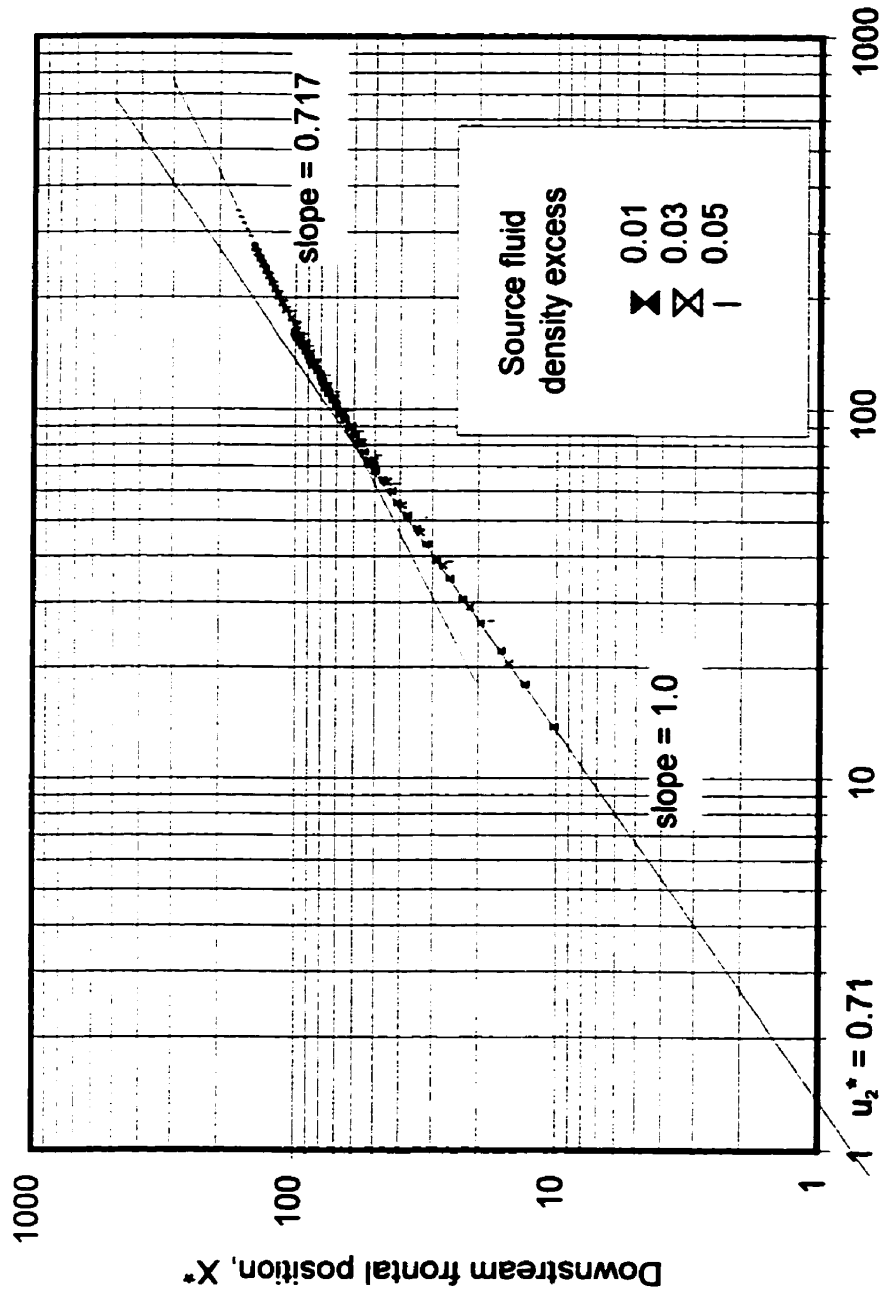

Figure 35. Normalized presentation of the spread rate data for rough-surface gravity current flows with a roughness element height of 25 mm and source fluid density excesses of 0.01, 0.03 and 0.05.

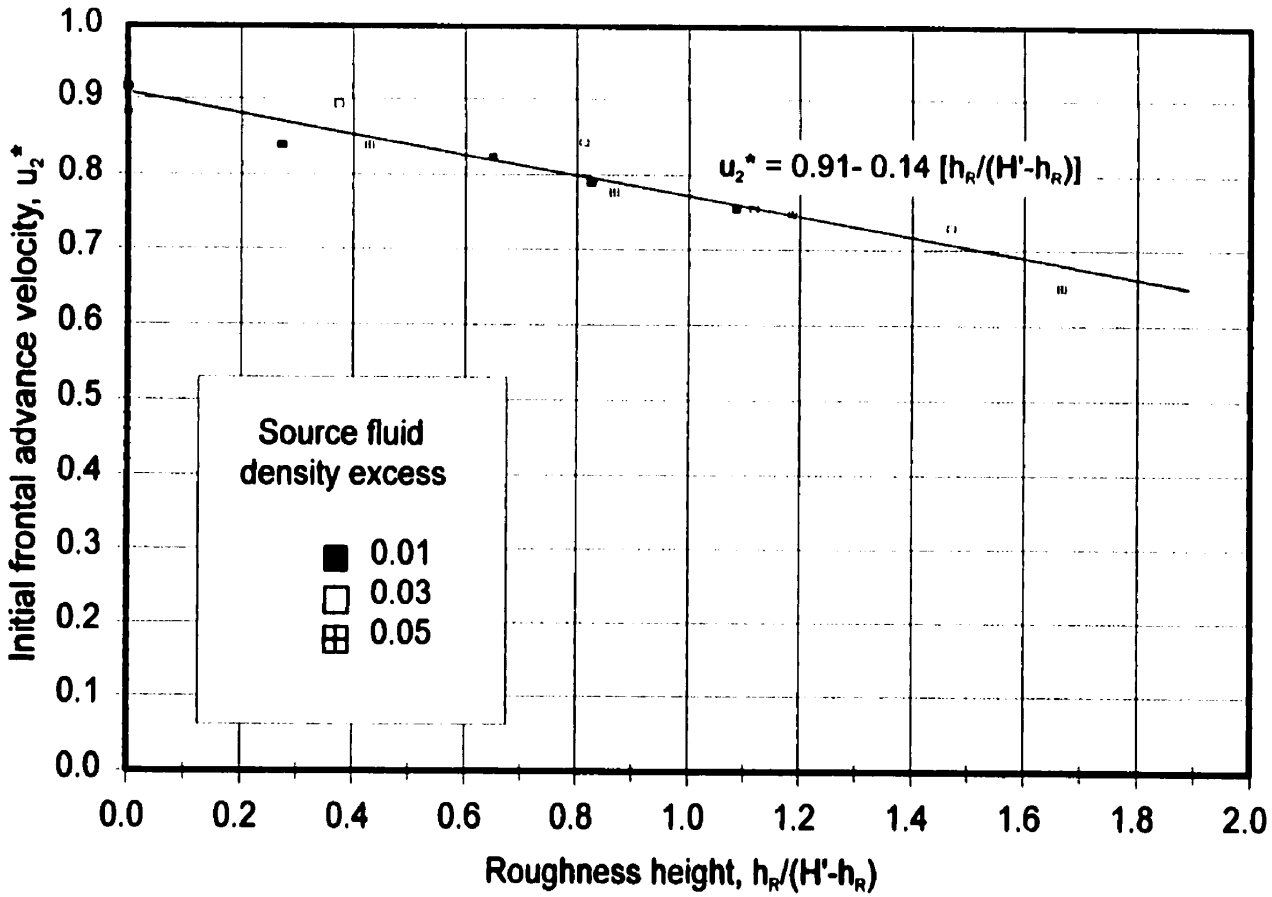

Figure 36. Influence of the surface roughness scale on the initial frontal advance velocity for flows with source fluid density excesses of 0.01, 0.03 and 0.05 where the initial frontal advance velocity is defined as the slope of the spread rate curve at $t^*=0$.

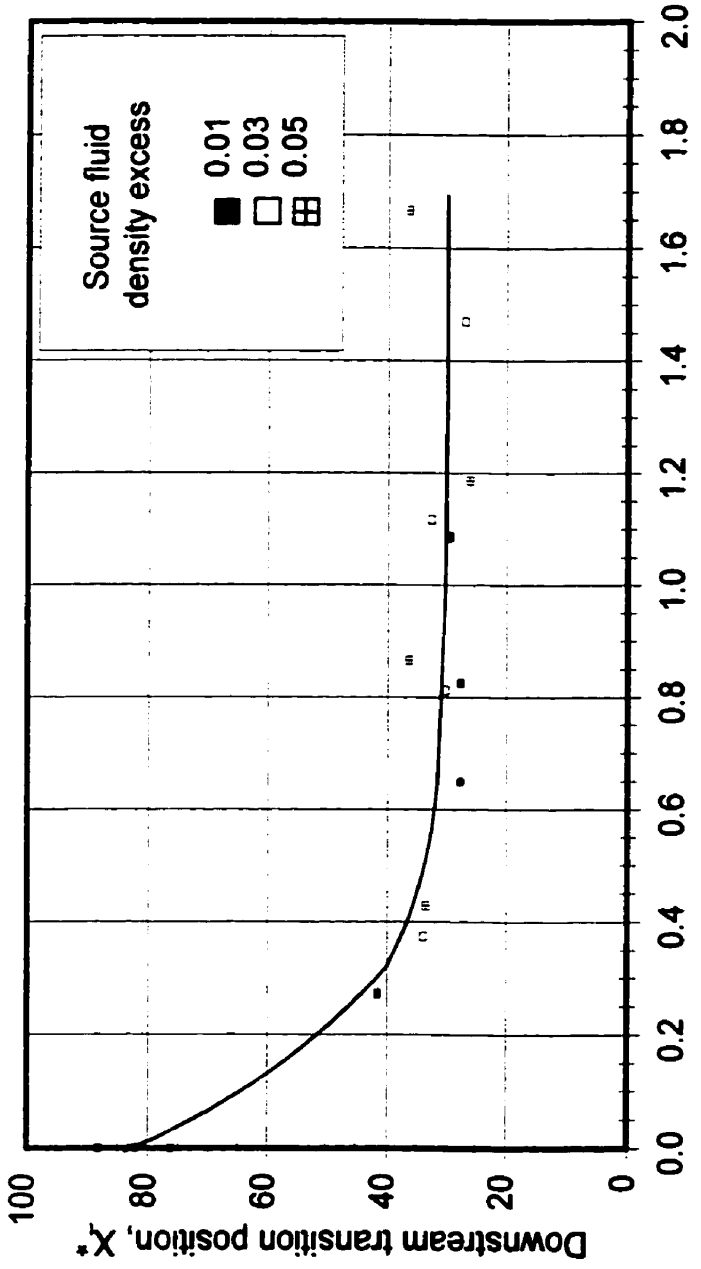

Figure 37. Influence of the surface roughness scale on the downstream transition position which separates the inertial-buoyant and viscous-buoyant regimes for flows with source fluid density excesses of 0.01, 0.03 and 0.05.

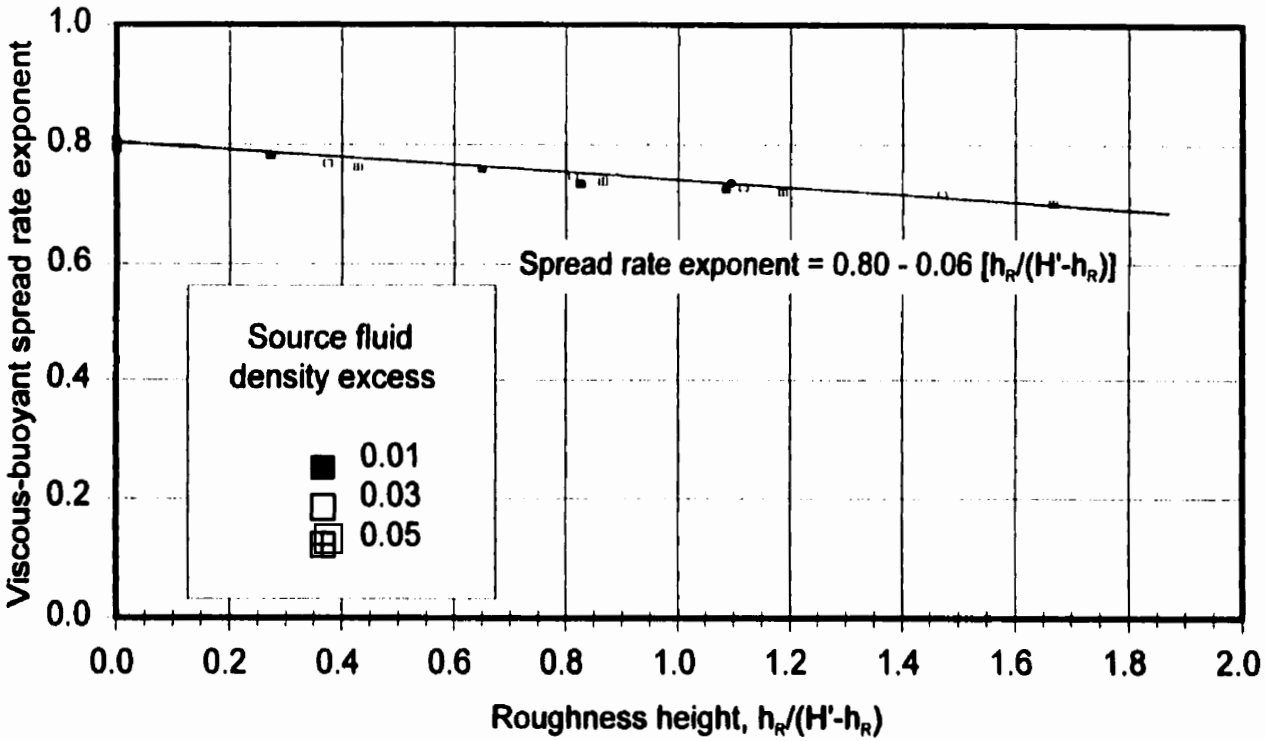

Figure 38. Influence of the surface roughness scale on the viscous-buoyant spread rate exponent for flows with source fluid density excesses of 0.01, 0.03 and 0.05.

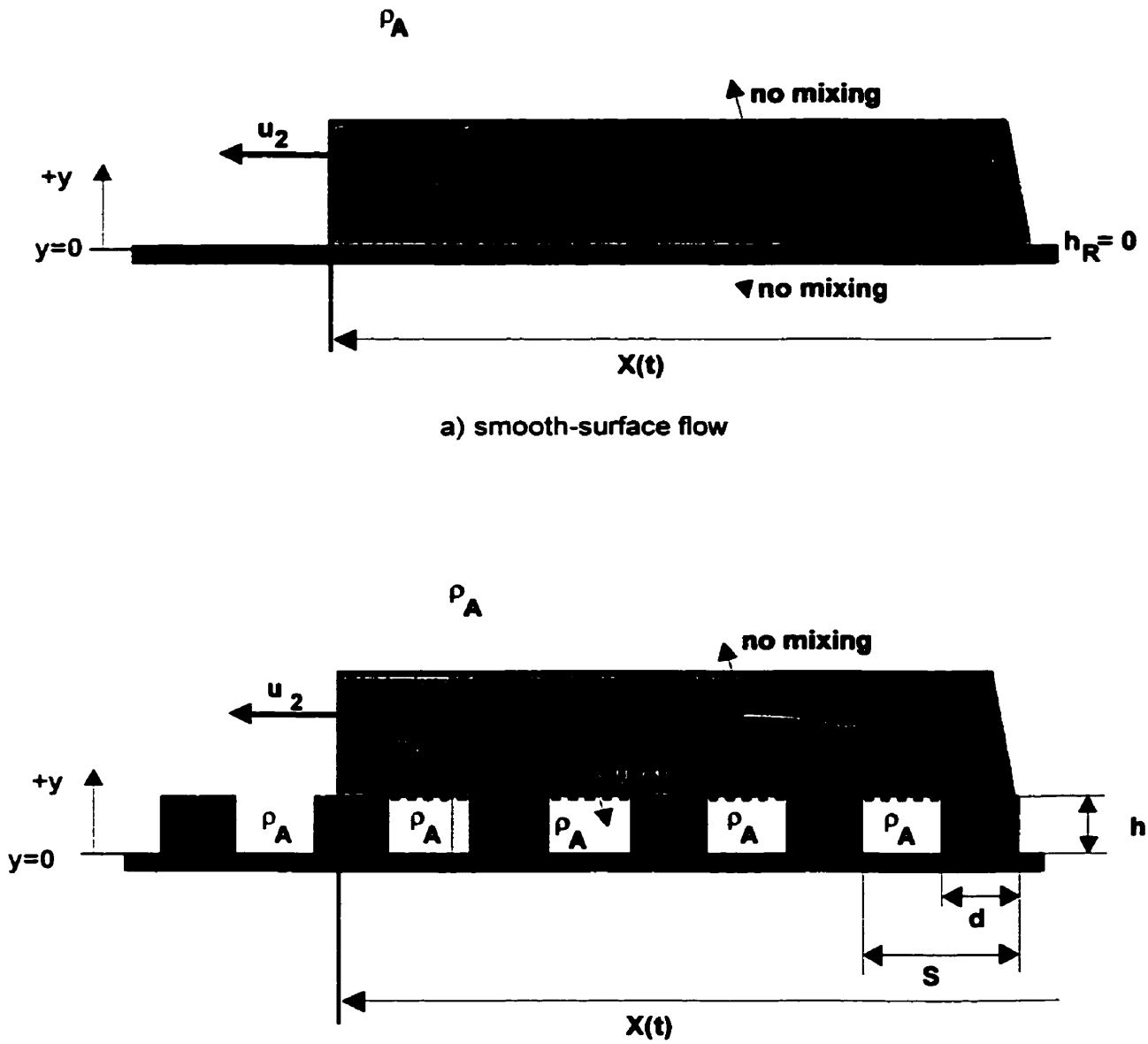

Figure 39. Schematic illustrations of simple models used for development of gravity current flow theory over a) smooth surfaces and b) beam-roughened surfaces.

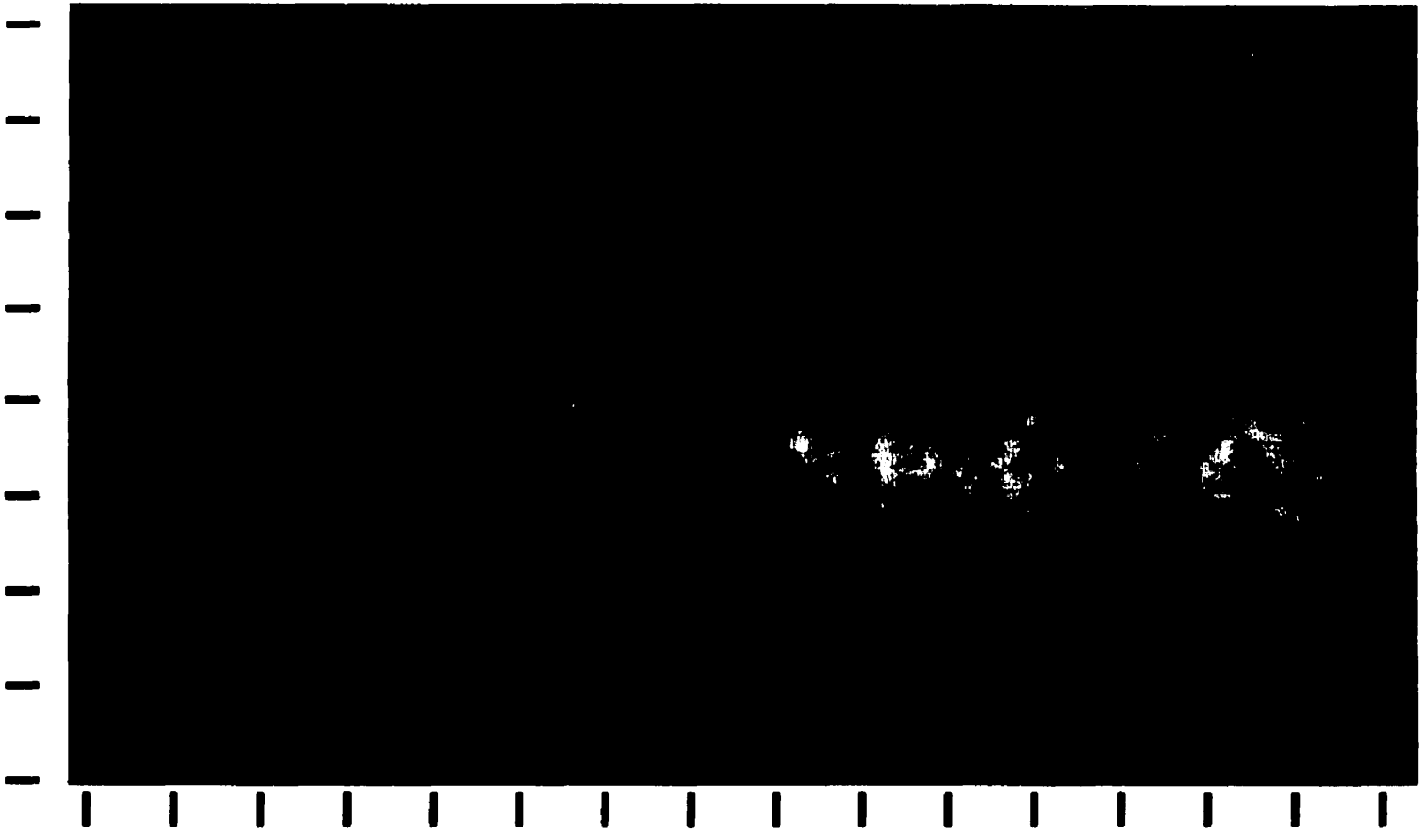

Figure 40. Typical gravity current flow progressing along the tops of the roughness elements in which areas of mixing between the two system fluids appear as darker regions within the head structure. Roughness element height = 1.9 cm. Source fluid density excess = 0.01. (Scales are divided in 1 cm increments. Roughness elements added graphically.)

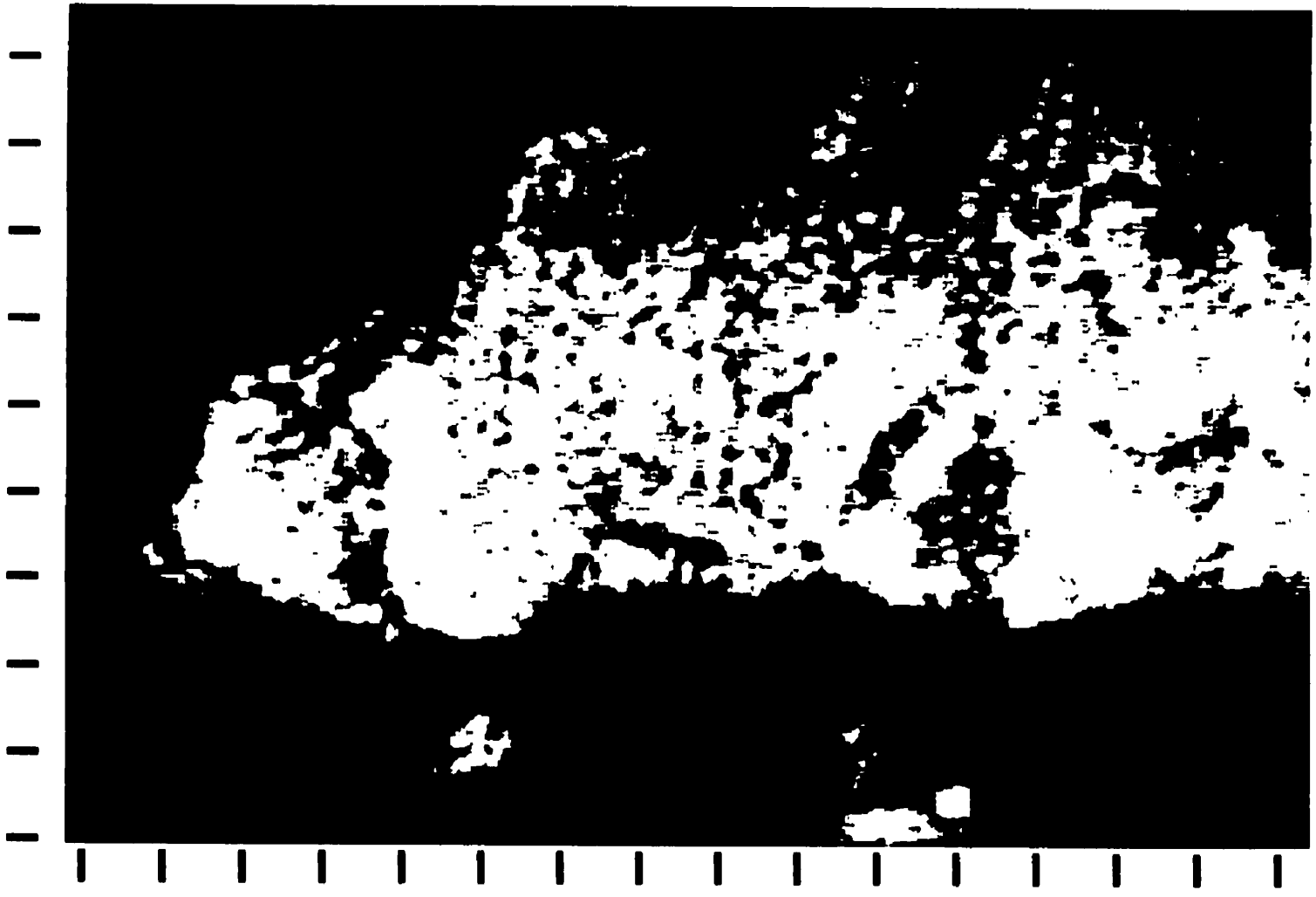

Figure 41. Image of a gravity current flowing along the top of the roughness elements showing the circulation generated within a roughness element space leading to mixing between the ambient and current fluids. Roughness element height = 2.5 cm. Source fluid density excess = 0.01. (Scales are divided in 1 cm increments. Roughness elements added graphically.)

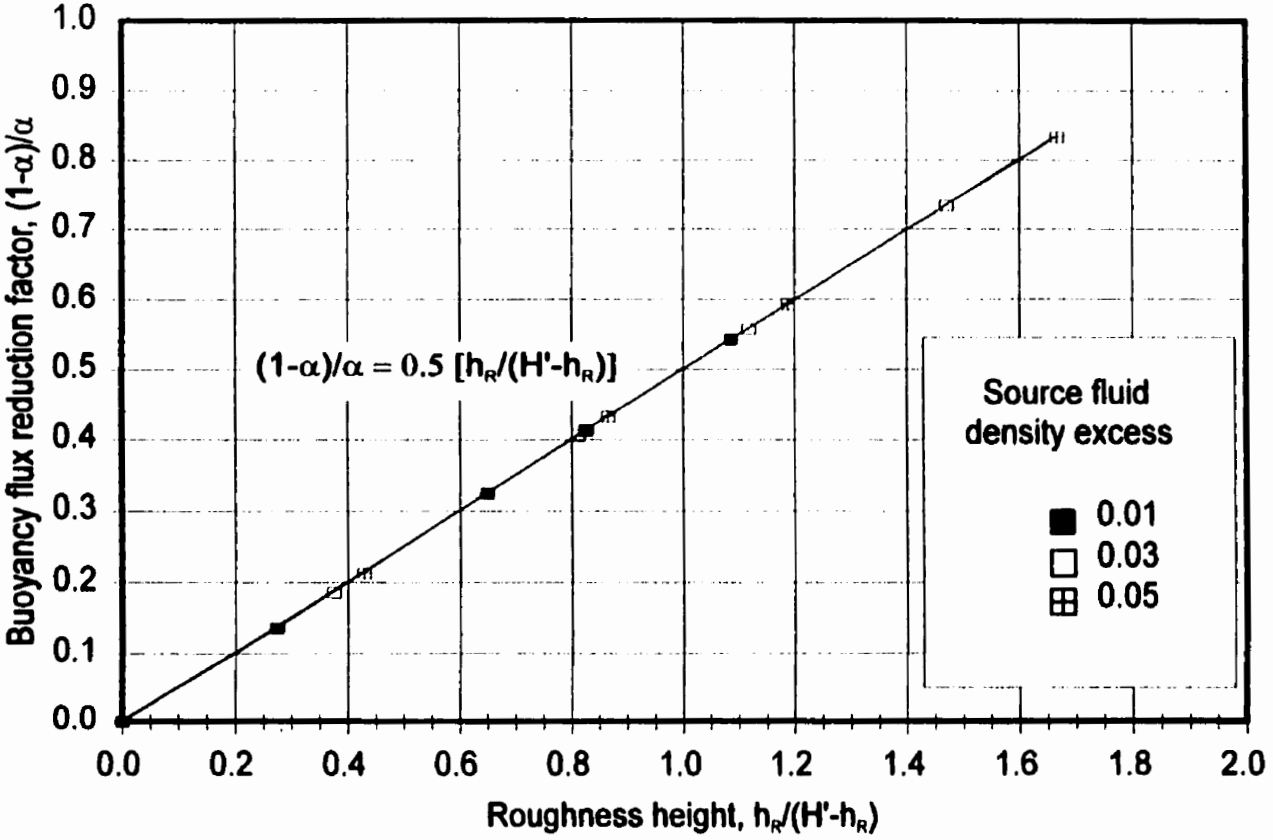

Figure 42. Effect of the surface roughness scale, $h_R/(H'-h_R)$, on the buoyancy flux reduction factor for flows with source fluid density excesses of 0.01, 0.03 and 0.05.

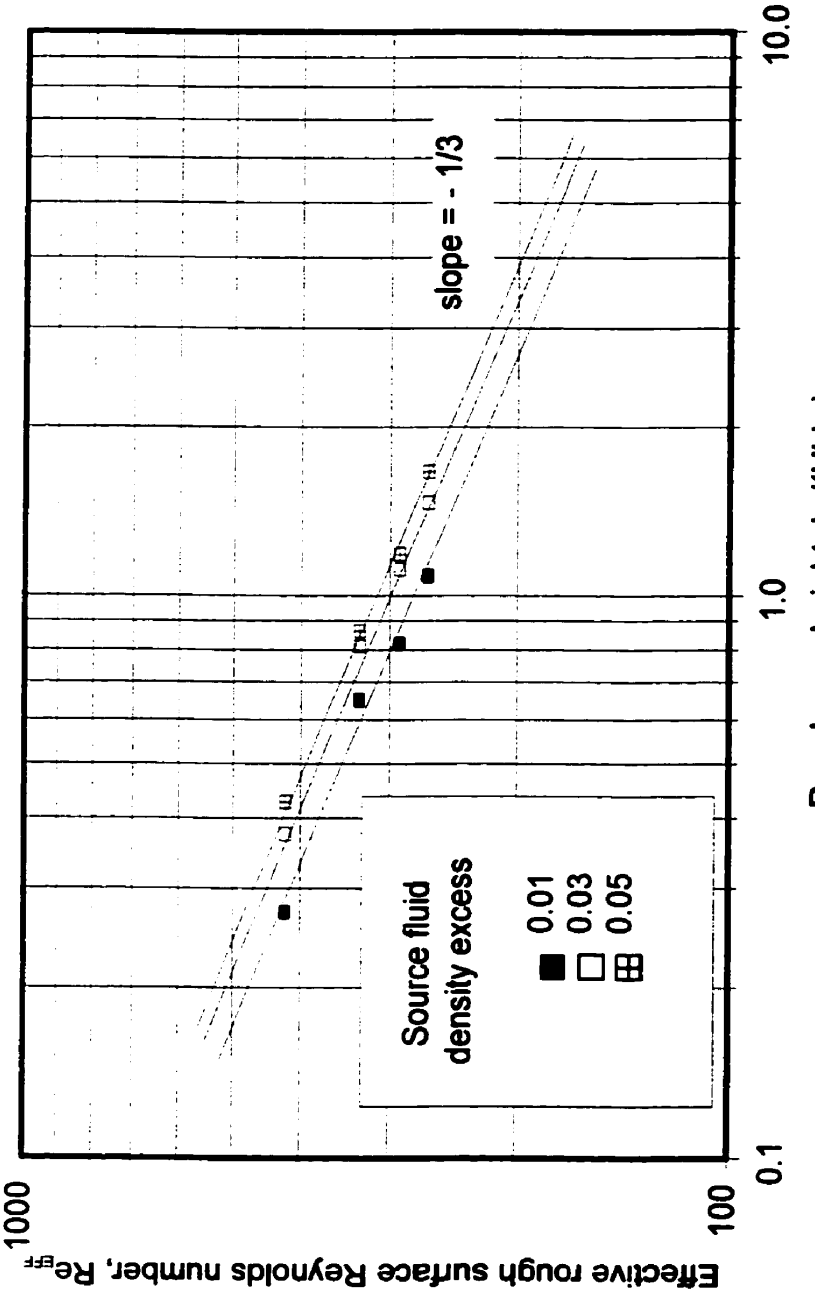

Figure 43. Influence of the surface roughness scale on the effective rough surface Reynolds number for flows with source fluid density excesses of 0.01, 0.03 and 0.05.

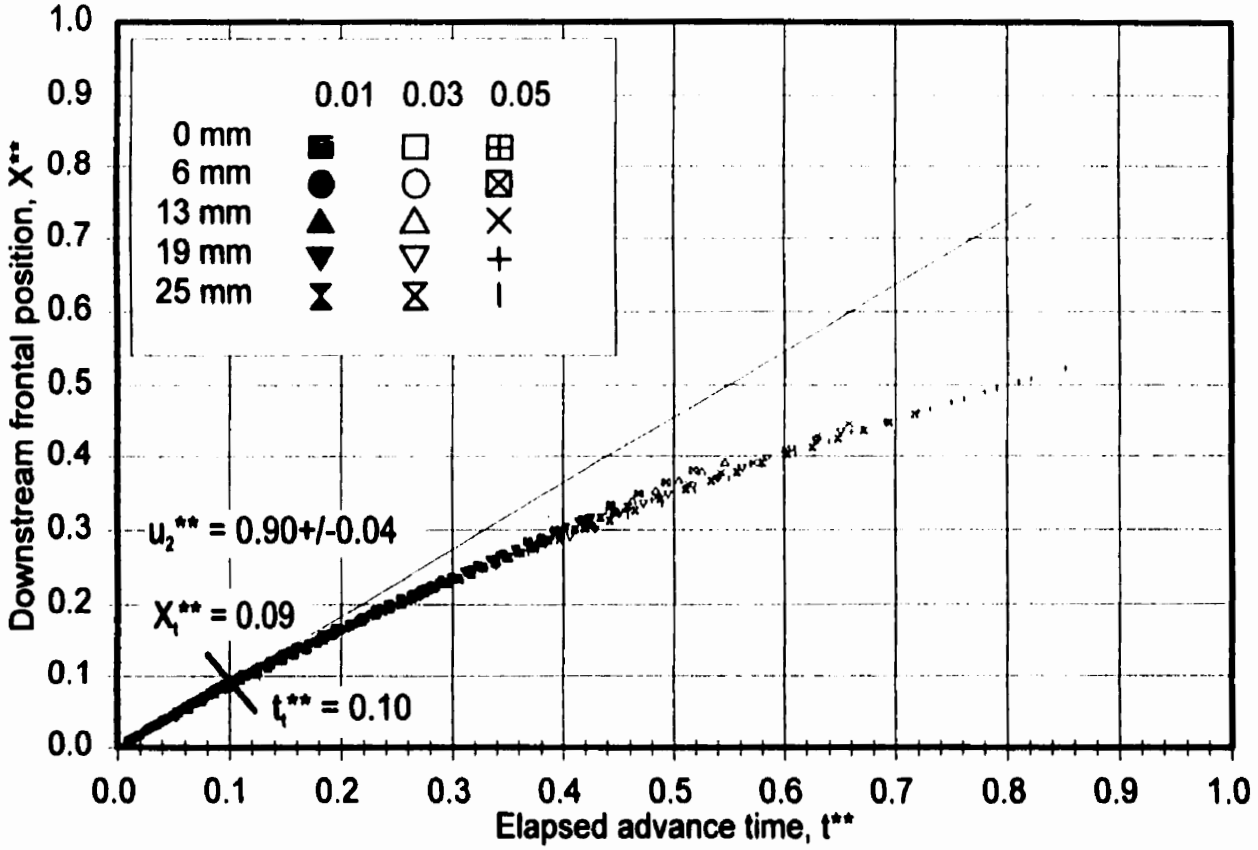

Figure 44. Presentation of the spread rate data for all gravity current flows over the range of surface roughness scales and source fluid density excesses used based on the rough surface normalization procedure.

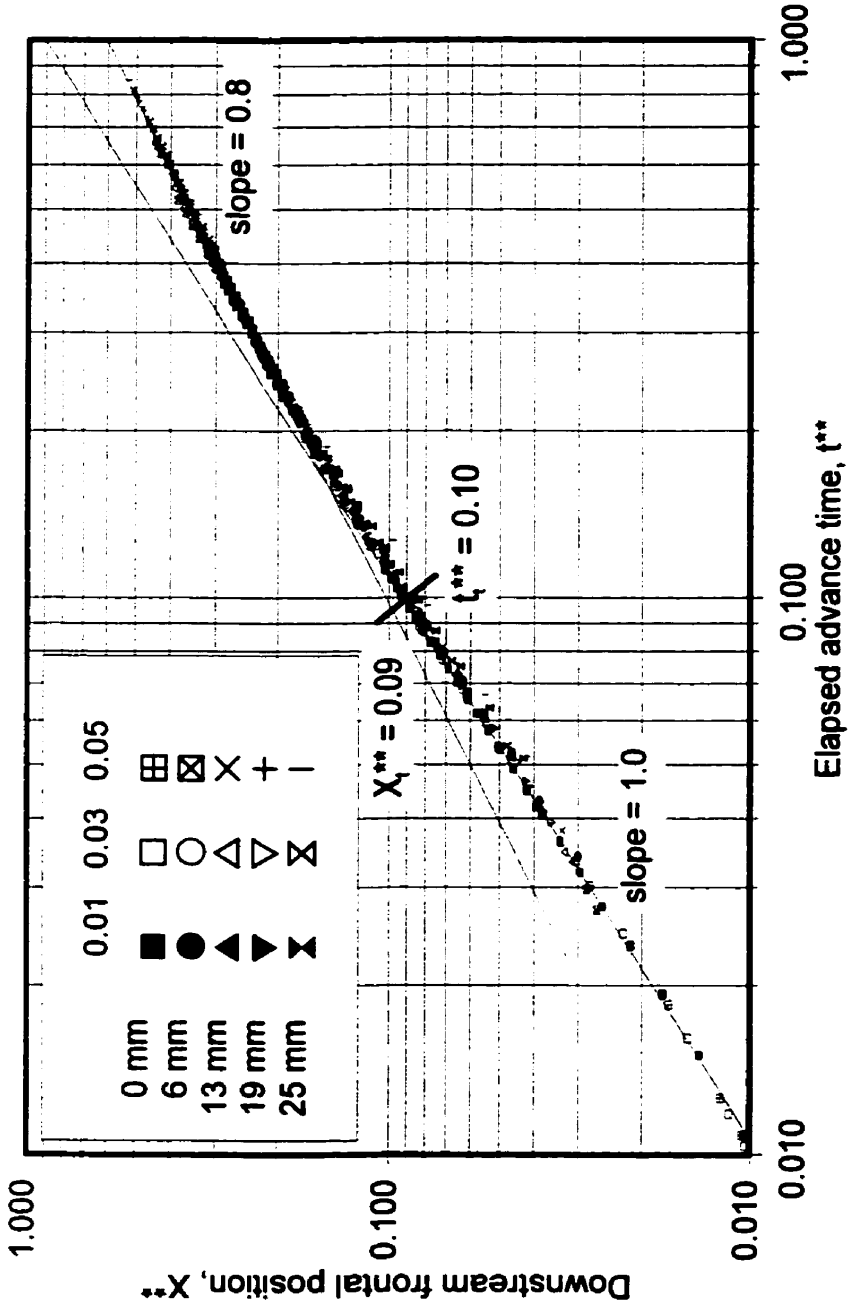

Figure 45. Log-log presentation of the spread rate data for all gravity current flows over the range of surface roughness scales and source fluid density excesses used based on the rough surface normalization procedure.

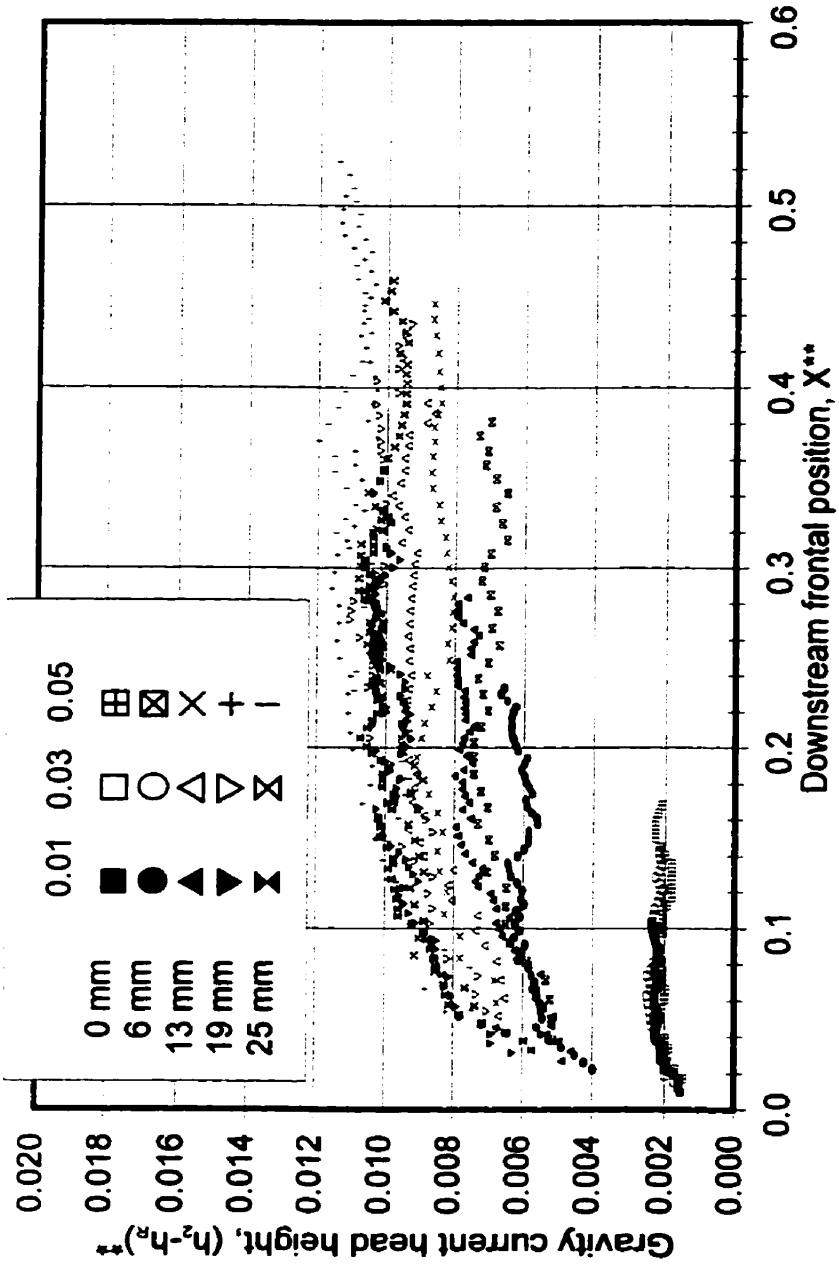

Figure 46. Presentation of the gravity current head height data normalized with d_R for all gravity current flows over the range of surface roughness scales and source fluid density excesses used.

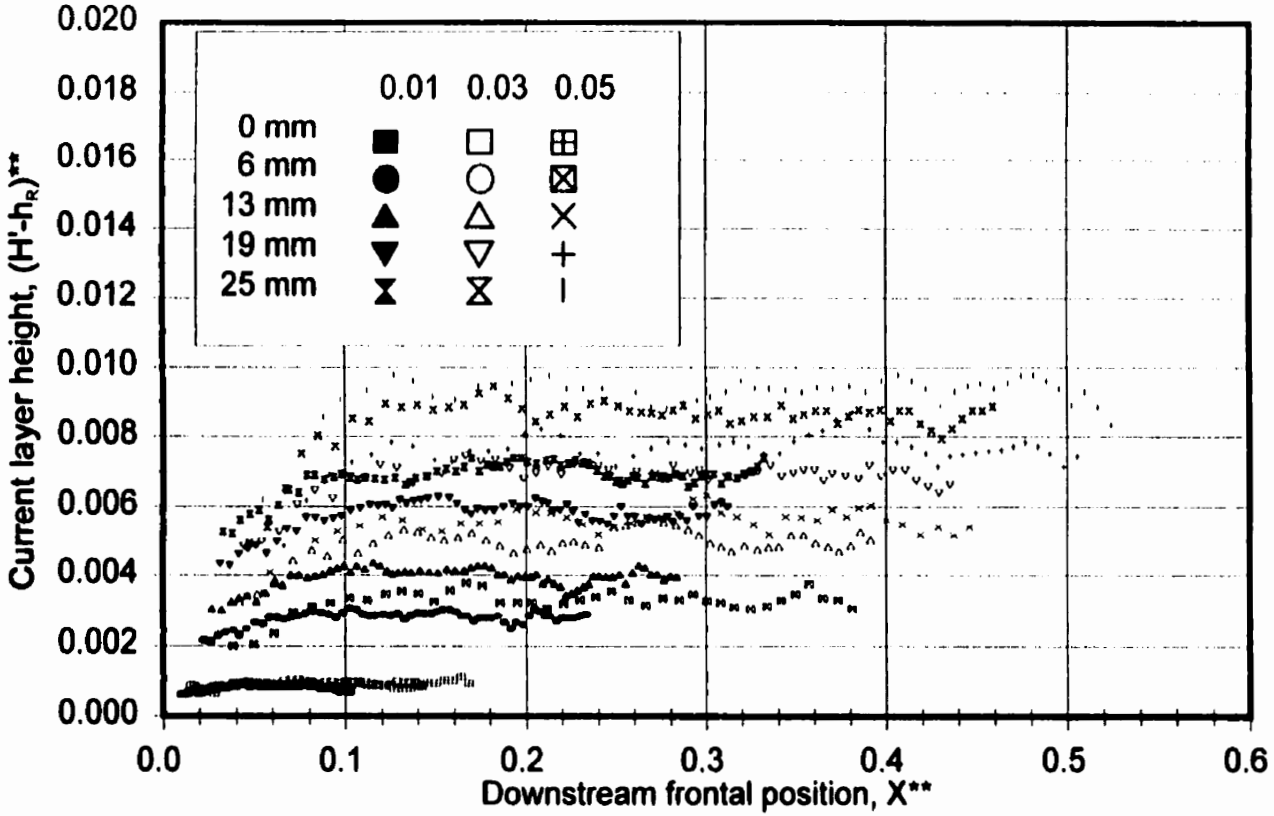

Figure 47. Presentation of the gravity current layer height data normalized with d_R for all gravity current flows over the range of surface roughness scales and source fluid density excesses used.

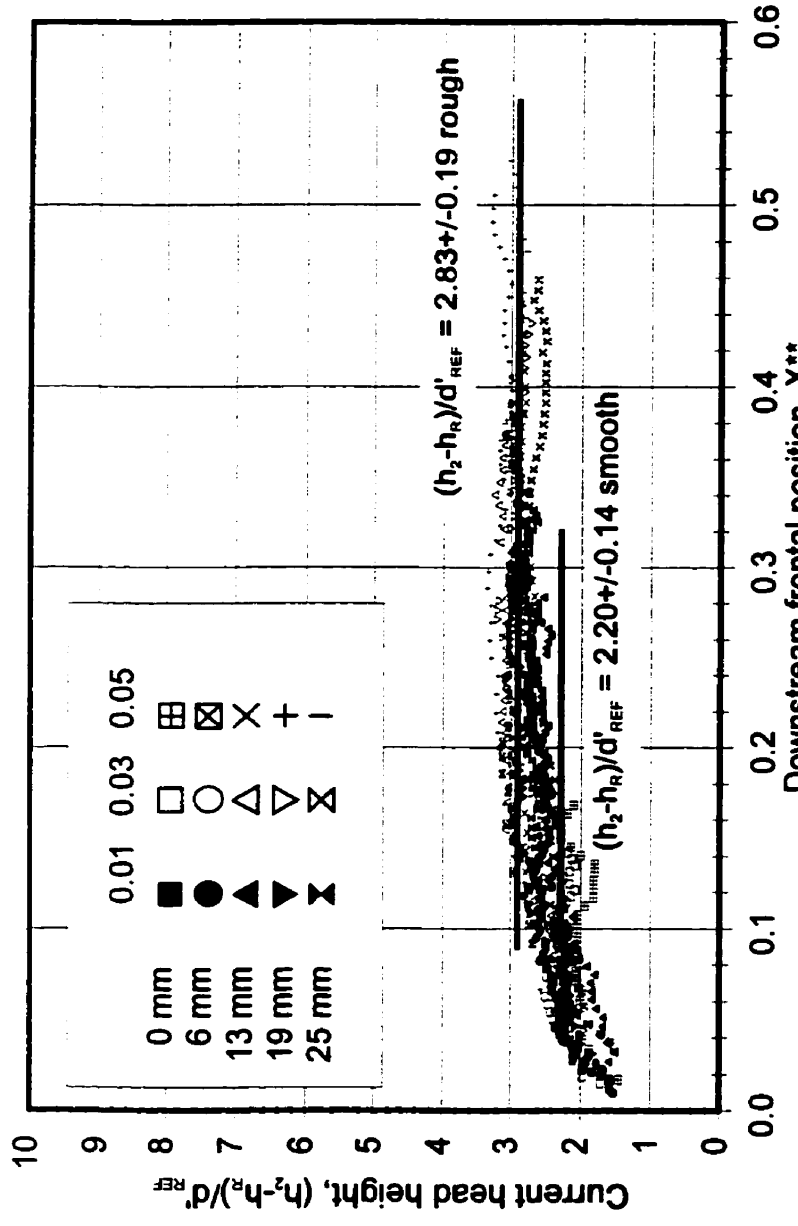

Figure 48. Presentation of the gravity current head height data normalized with d'_{REF} for all gravity current flows over the range of surface roughness scales and source fluid density excesses used.

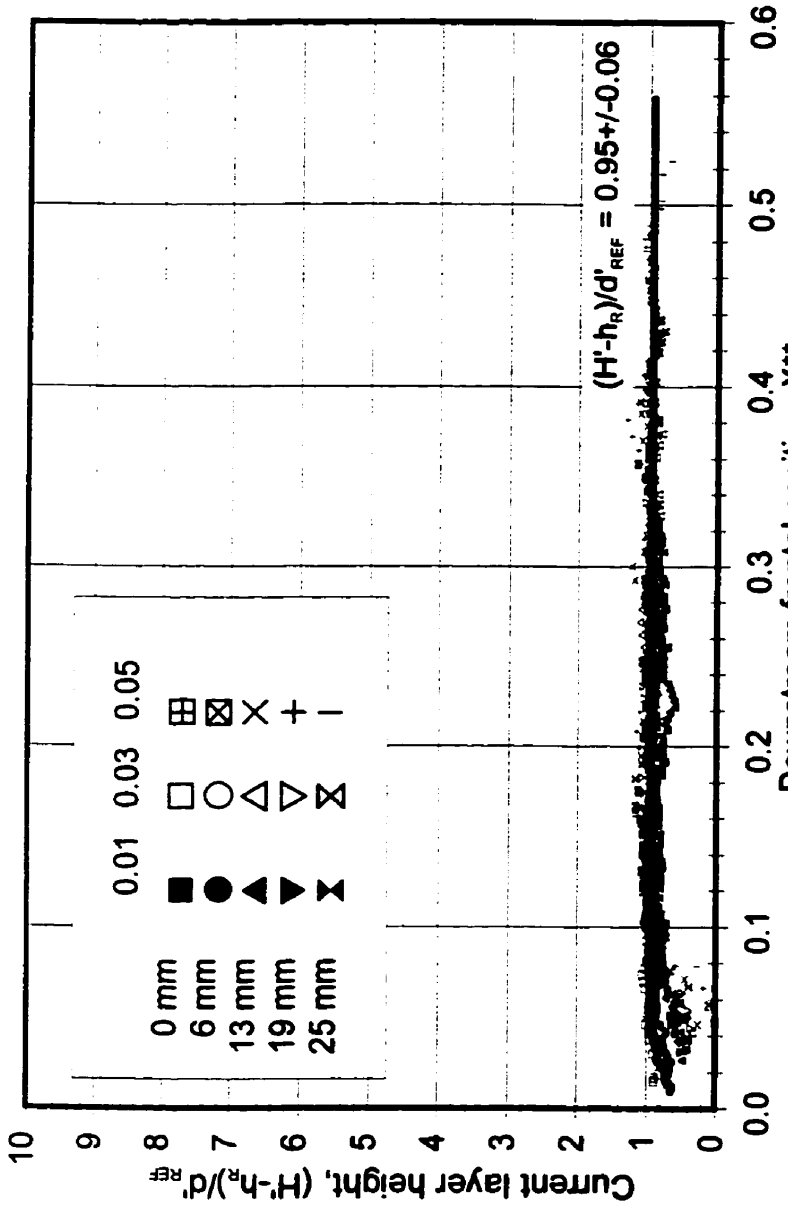

Figure 49. Presentation of the gravity current layer height data normalized with d'_{REF} for all gravity current flows over the range of surface roughness scales and source fluid density excesses used.

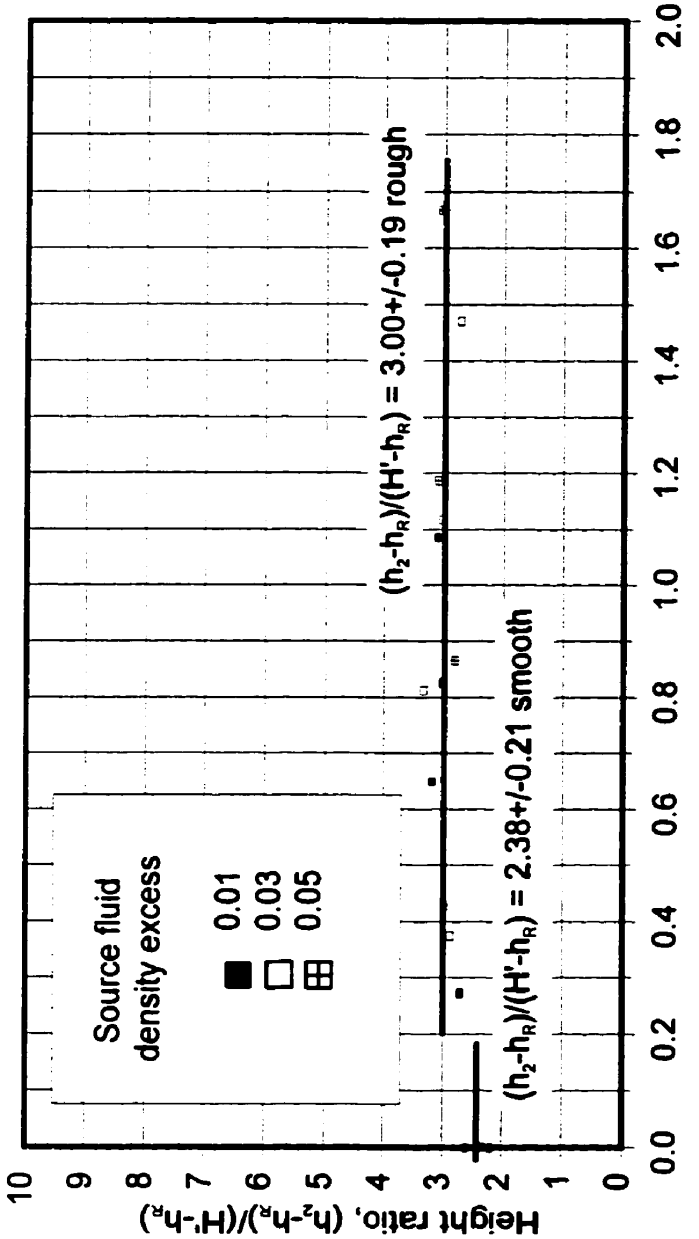

Figure 50. Influence of the surface roughness scale on the ratio of head height to the height of the layer immediately behind the head for flows with source fluid density excesses of 0.01, 0.03 and 0.05. (Note that each point on the graph represents a different test run.)

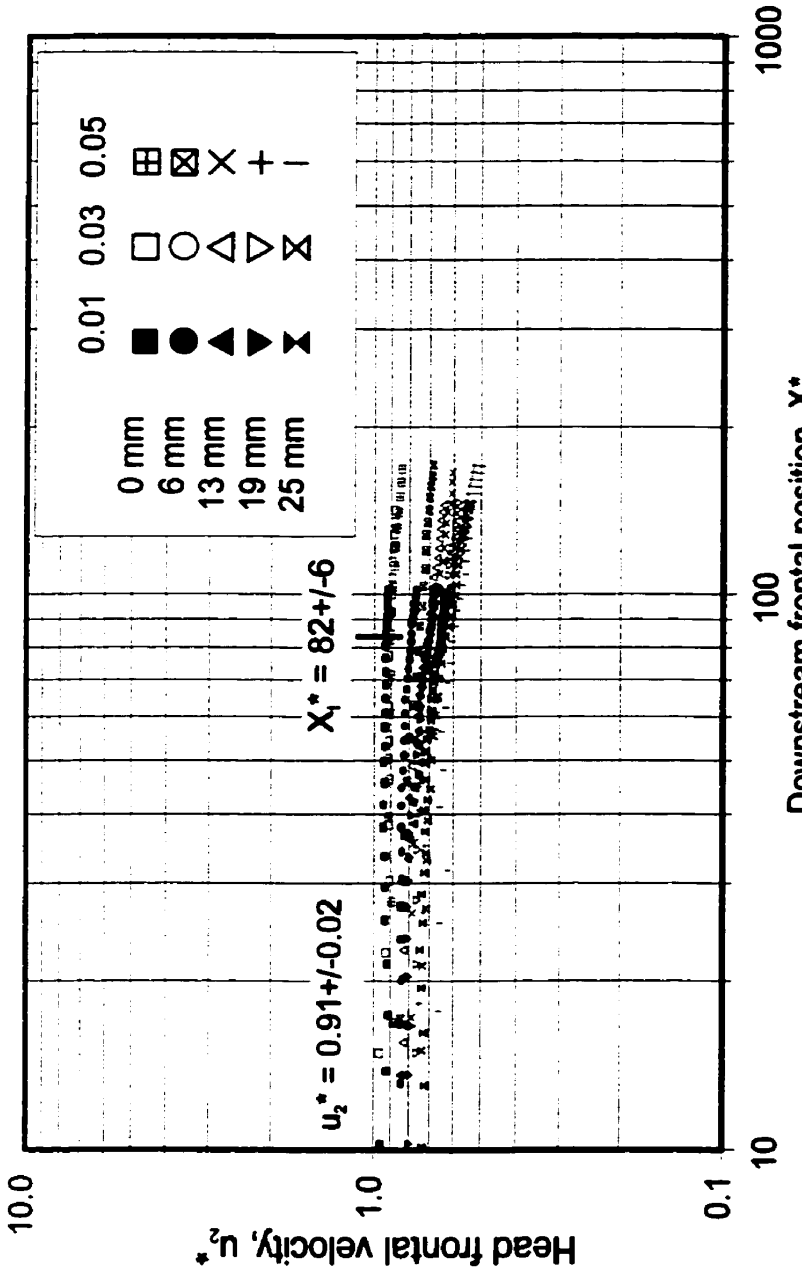

Figure 51. Head frontal velocity versus downstream frontal position normalized using the characteristic smooth surface scales for all gravity current flows over the range of surface roughness scales and source fluid density excesses used.

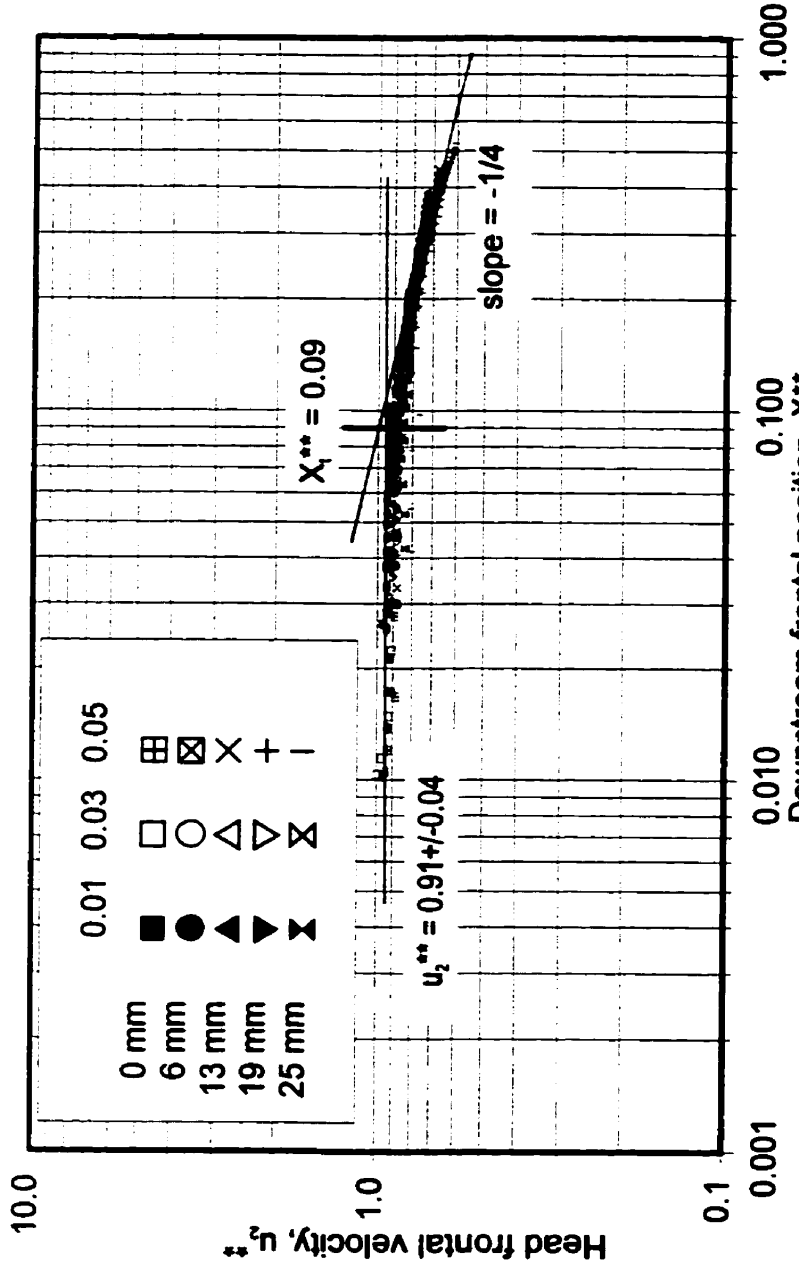

Figure 52. Head frontal velocity versus downstream frontal position normalized using the characteristic rough surface scales for all gravity current flows over the range of surface roughness scales and source fluid density excesses used.

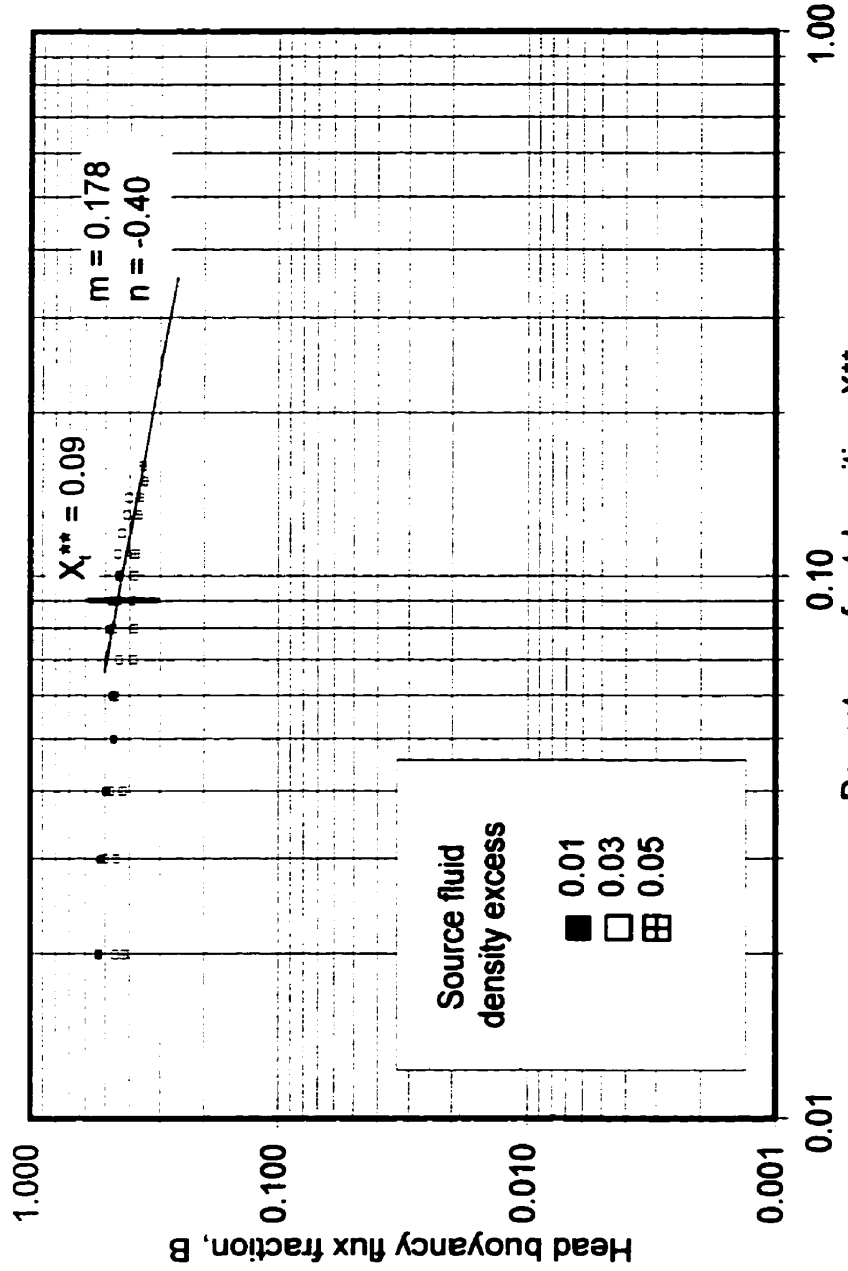

Figure 53. Variation of the head buoyancy flux fraction with downstream frontal position for gravity current flows over the range of source fluid density excesses used and with a surface roughness scale of h_R = 0 mm.

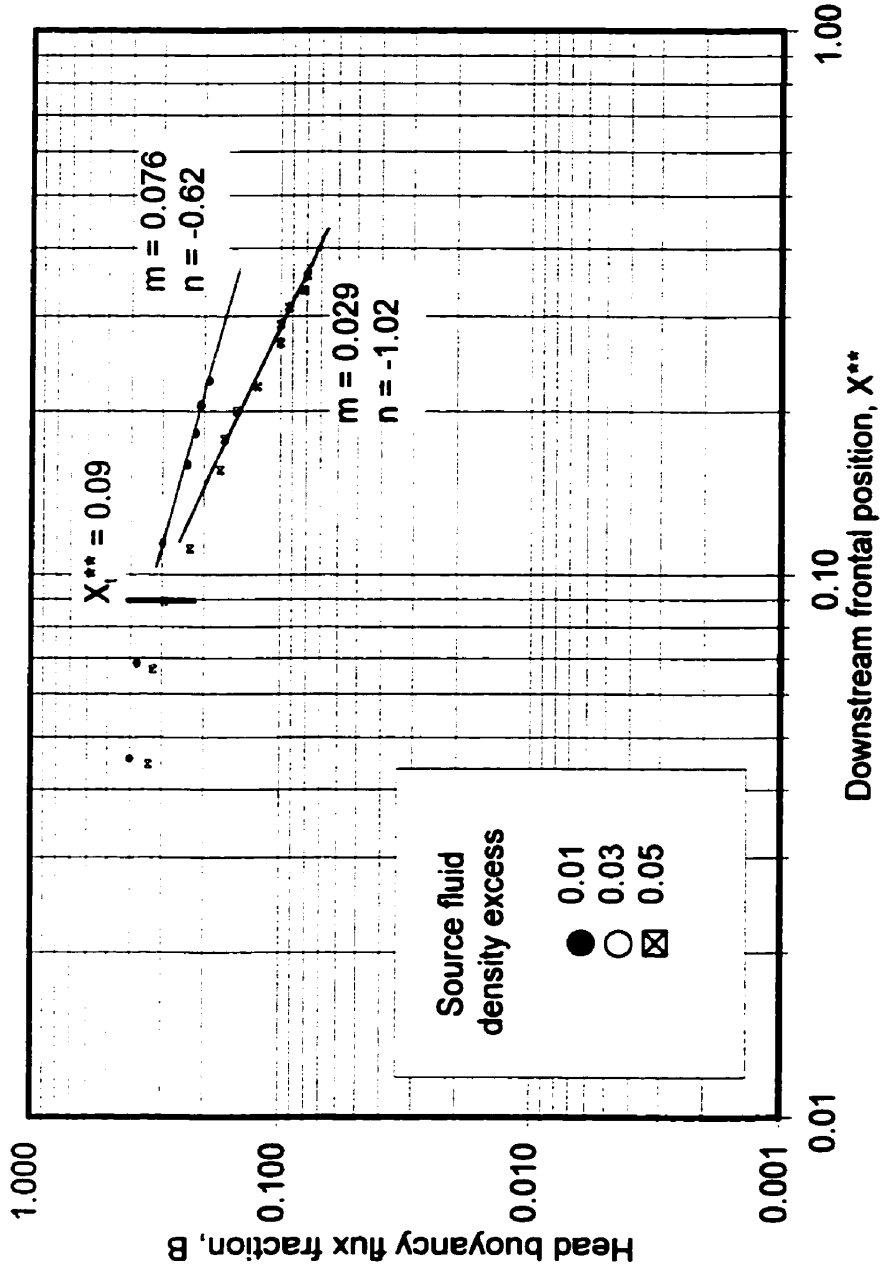

Figure 54. Variation of the head buoyancy flux fraction with downstream frontal position for gravity current flows over the range of source fluid density excesses used and with a surface roughness scale of h_R = 6 mm.

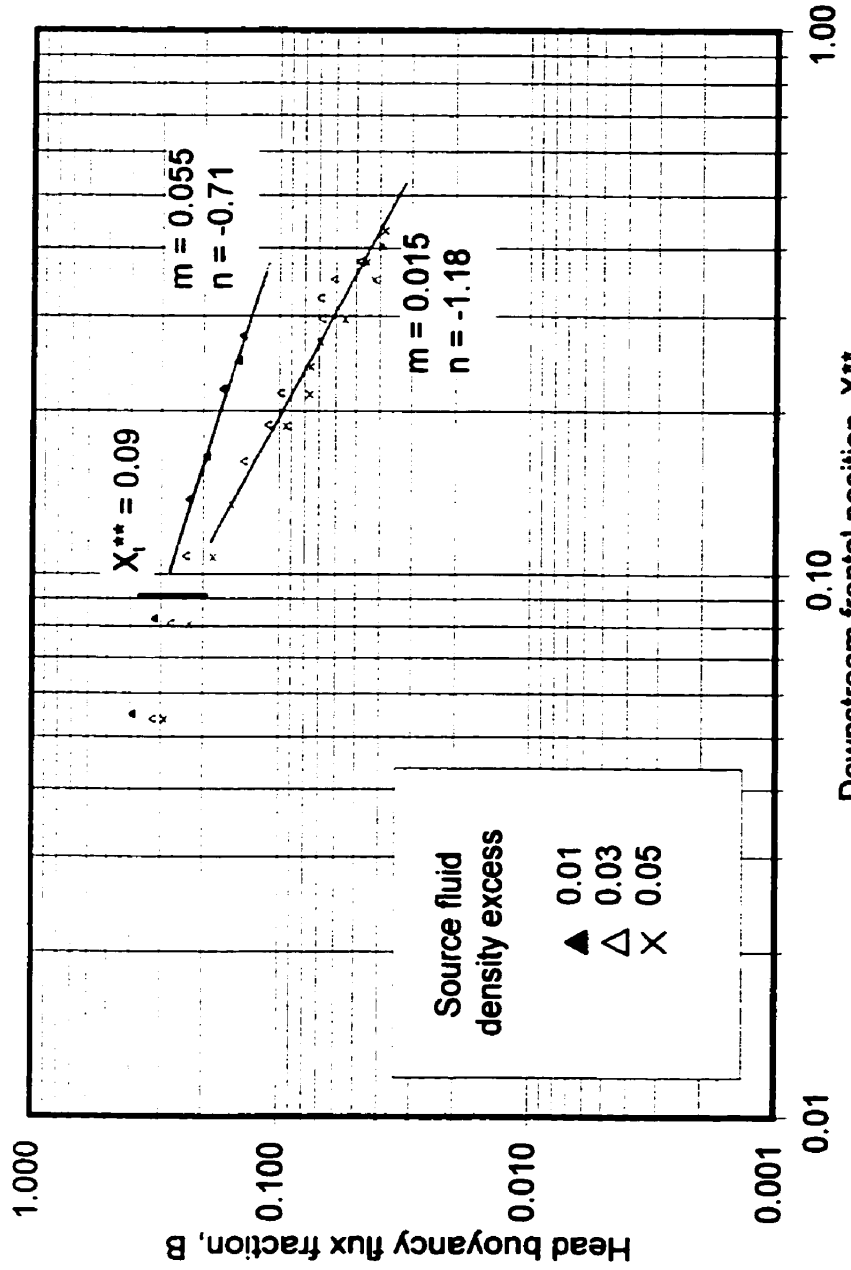

Figure 55. Variation of the head buoyancy flux fraction with downstream frontal position for gravity current flows over the range of source fluid density excesses used and with a surface roughness scale of h_R = 13 mm.

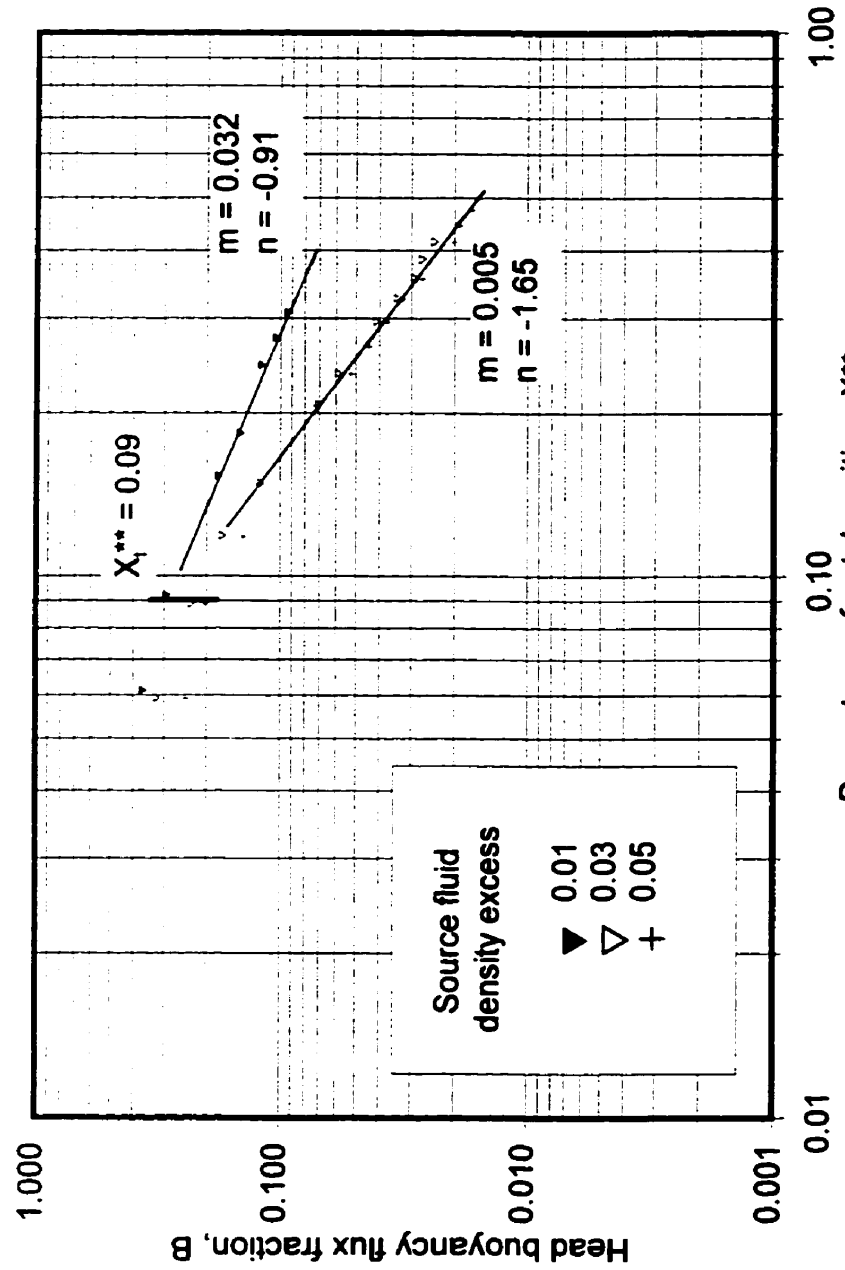

Figure 56. Variation of the head buoyancy flux fraction with downstream frontal position for gravity current flows over the range of source fluid density excesses used and with a surface roughness scale of h_R = 19 mm.

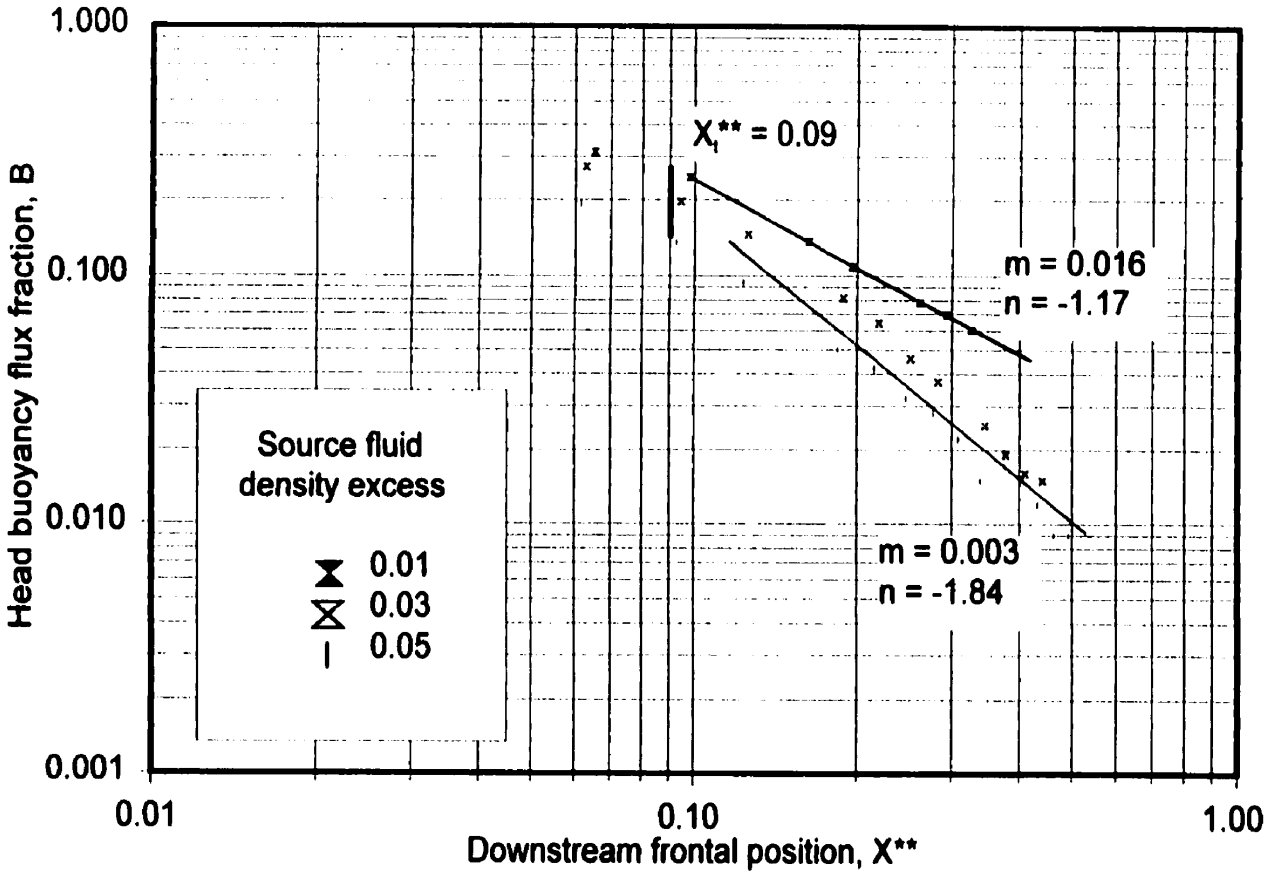

Figure 57. Variation of the head buoyancy flux fraction with downstream frontal position for gravity current flows over the range of source fluid density excesses used and with a surface roughness scale of h_R = 25 mm.

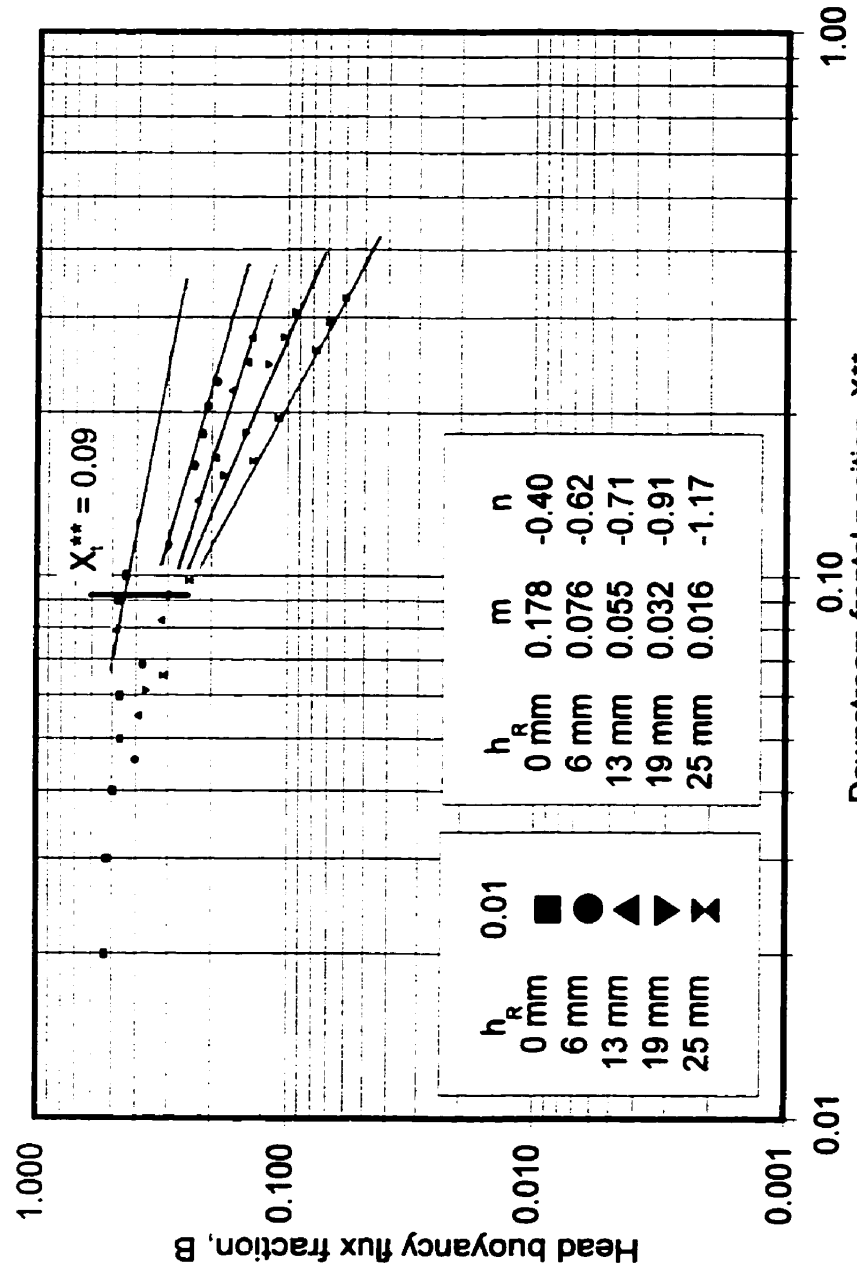

Figure 58. Variation of the head buoyancy flux fraction with downstream frontal position for gravity current flows over the range of surface roughness scales used and with a source fluid density excess of 0.01.

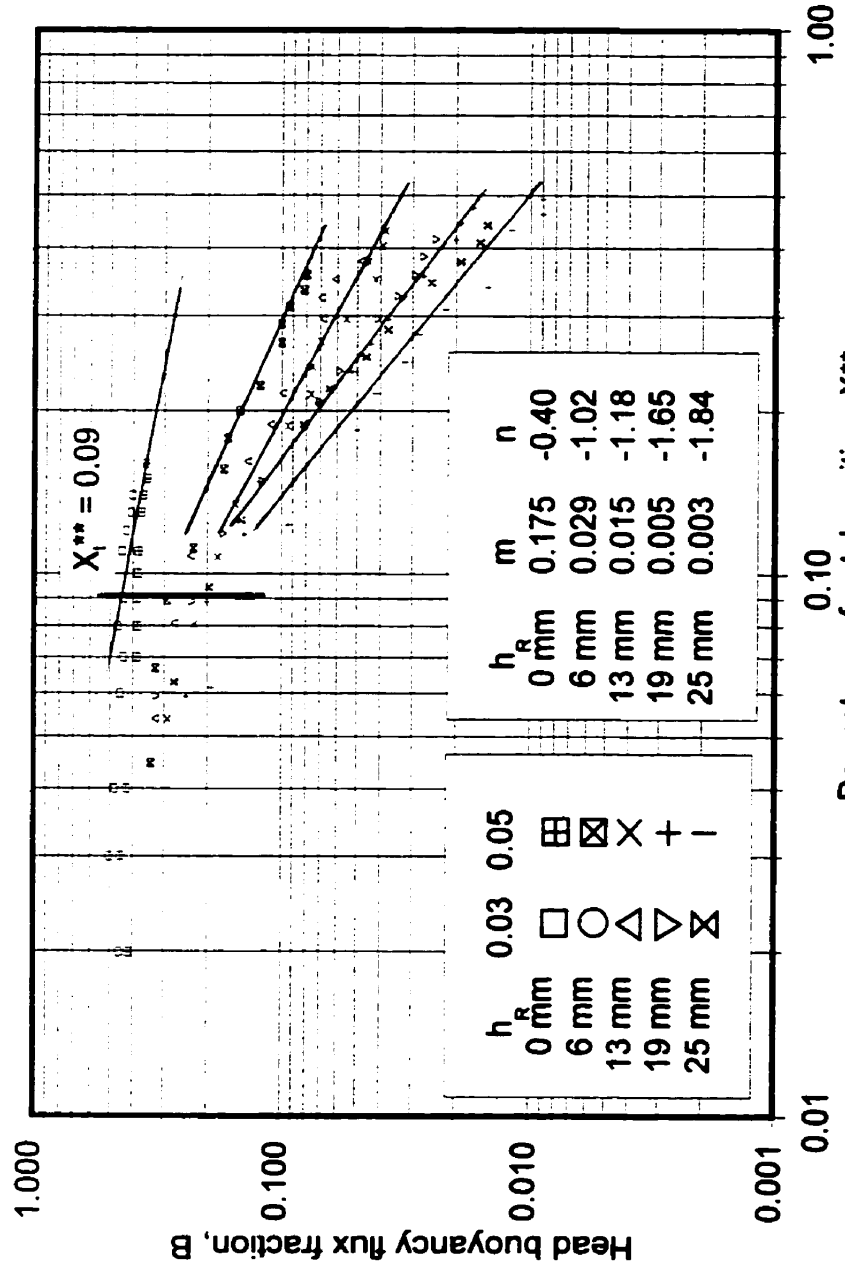

Figure 59. Variation of the head buoyancy flux fraction with downstream frontal position for gravity current flows over the range of surface roughness scales used and with source fluid density excesses of 0.03 and 0.05.

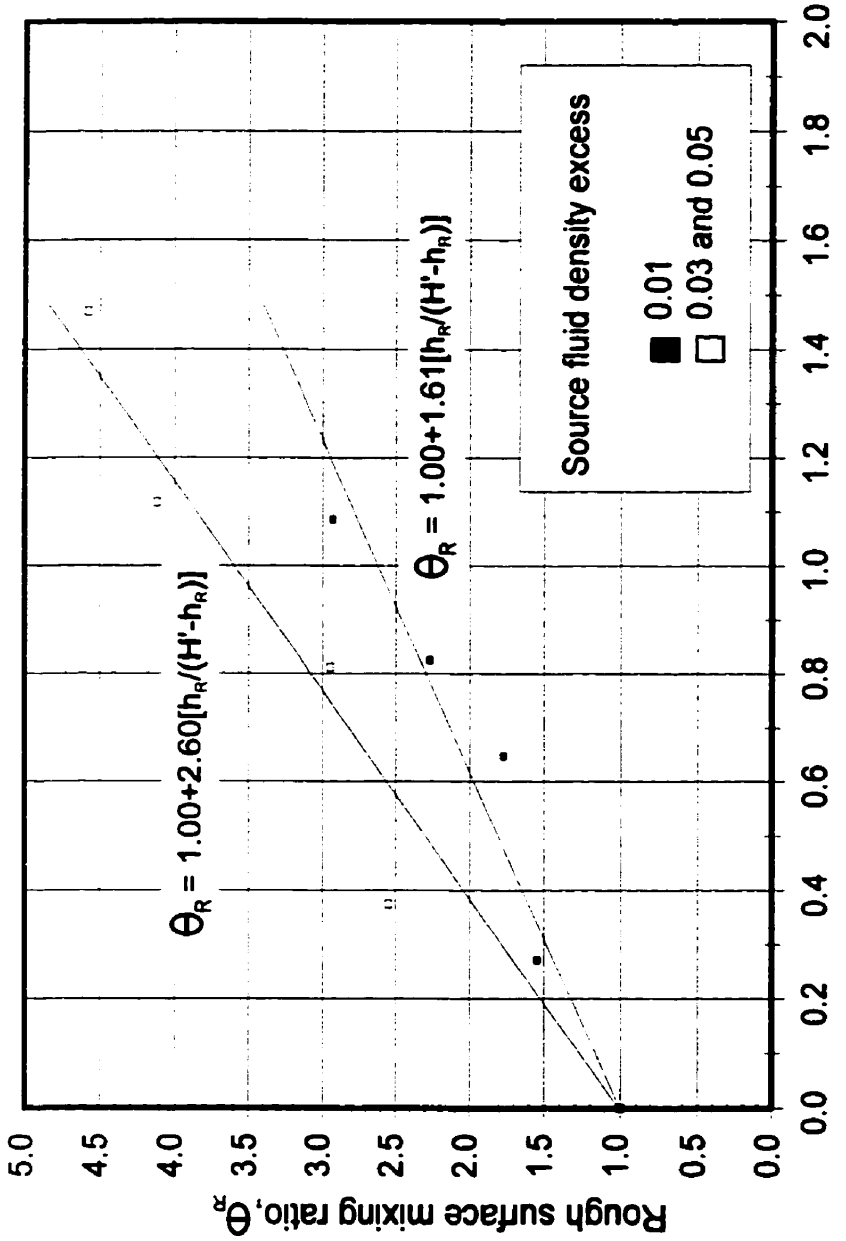

Figure 60. Influence of the surface roughness scale on the observed viscous-buoyant rough-surface mixing ratio for flows with source fluid density excesses of 0.01, 0.03 and 0.05

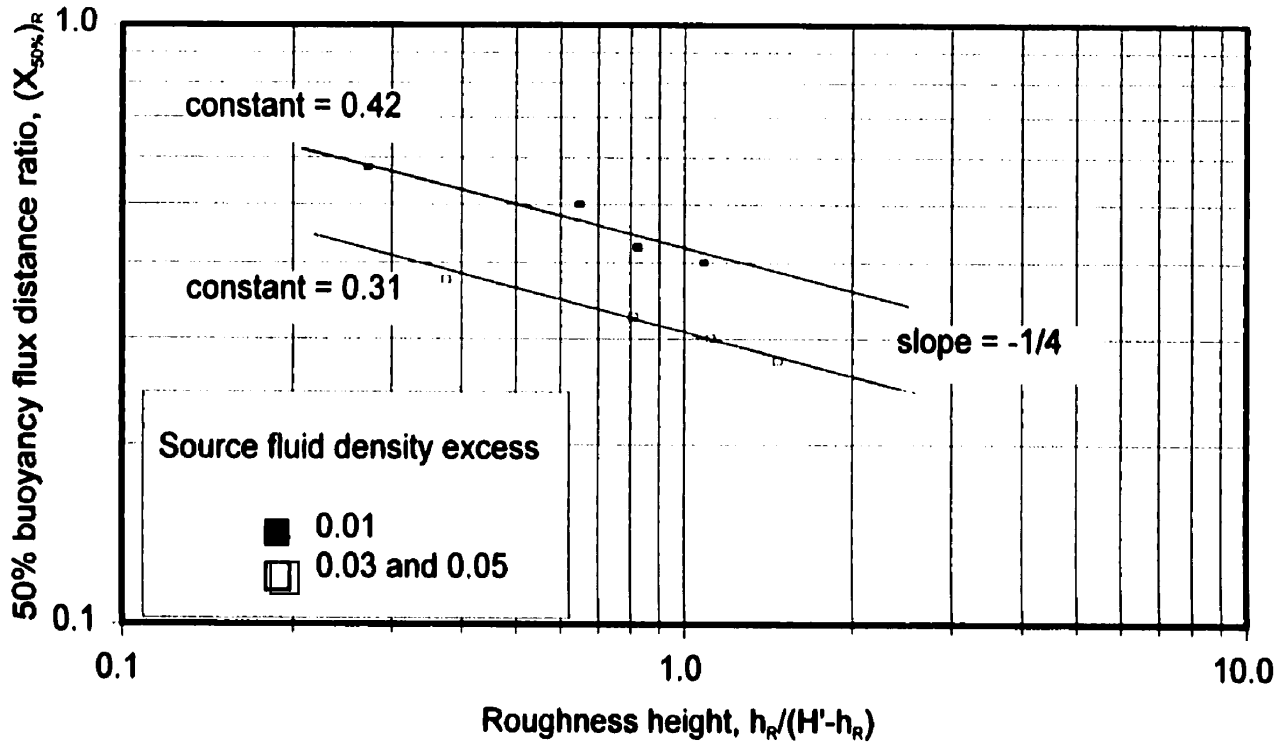

Figure 61. Influence of the surface roughness scale on the ratio of the rough/smooth-surface channel positions at which the buoyancy flux fraction falls to 50% of its initial value for flows with source fluid density excesses of 0.01, 0.03 and 0.05.

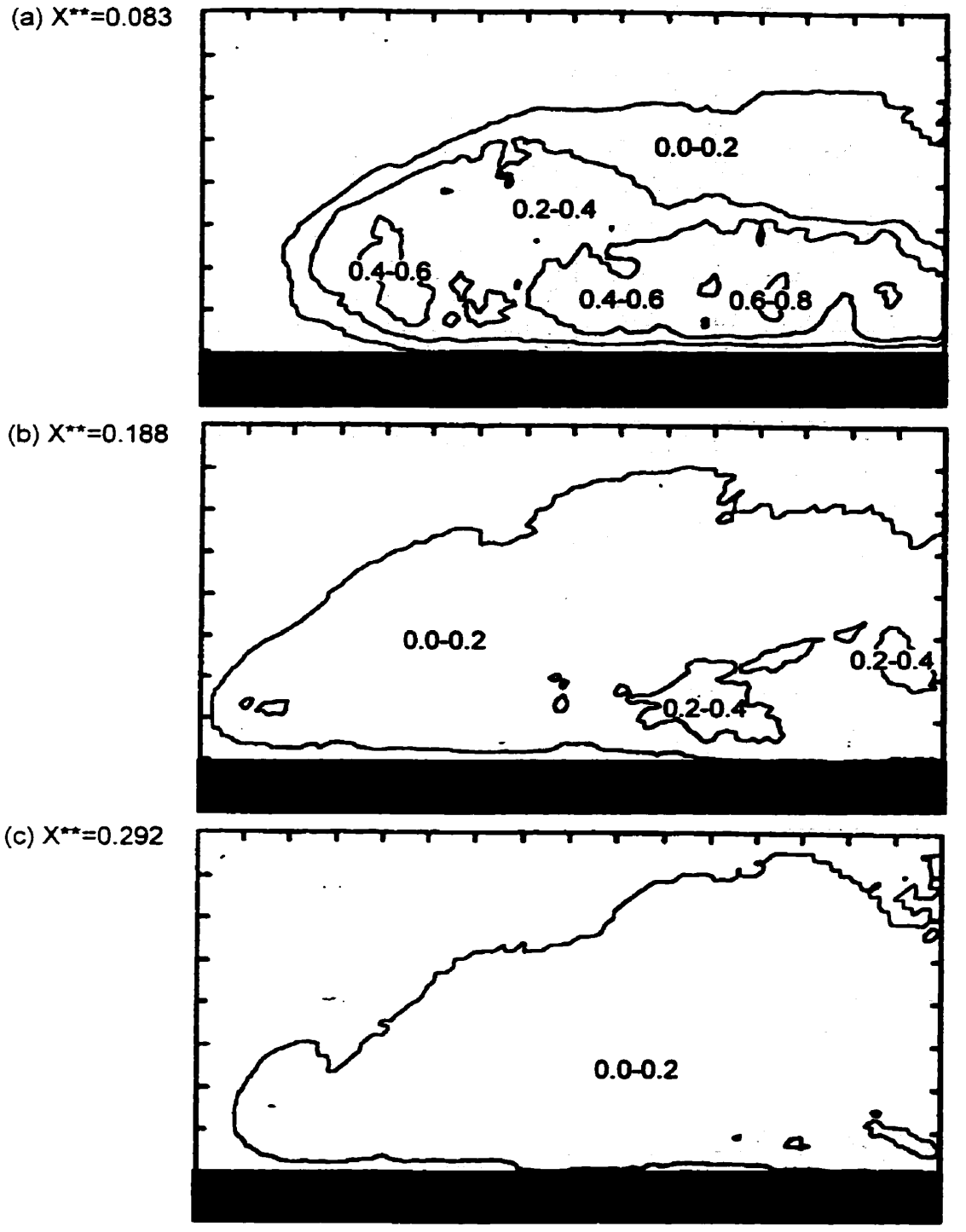

Figure 62. Profiles of the buoyancy flux fraction in a gravity current head for three downstream positions, a) X**=0.083, b) X**=0.188 and c) X**=0.292, for a flow with a source fluid density excess of 0.01 and a normalized roughness scale of 0.83 (h_R =1.9 cm). (Scales are divided in 1 cm increments.)

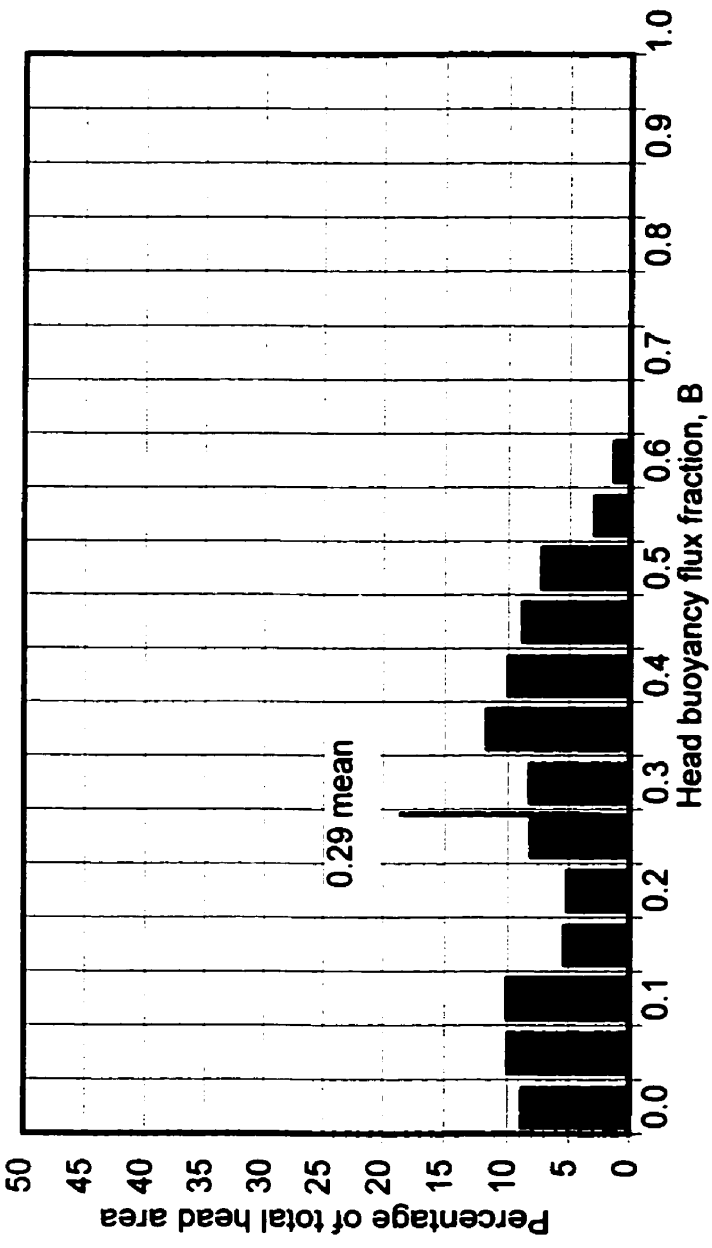

Figure 63a. Histogram showing the percentage of total head area occupied by a particular range of buoyancy flux fraction for the rough-surface flow described in Figure 62a.

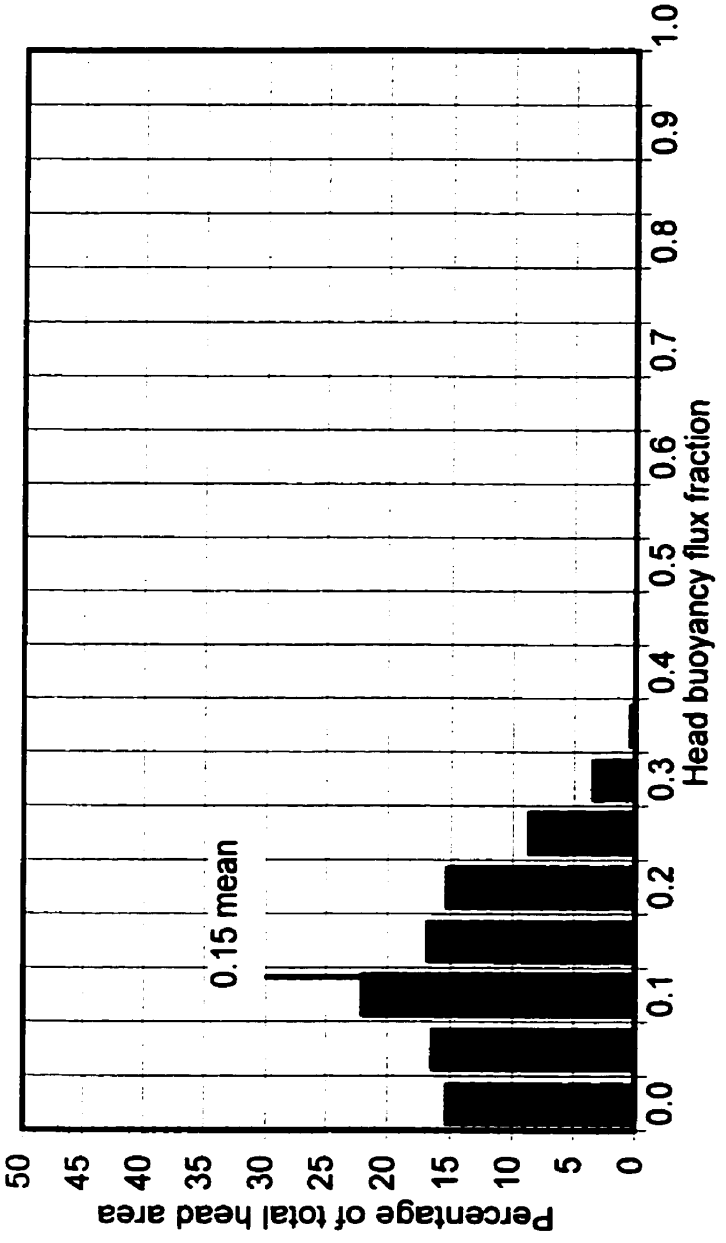

Figure 63b. Histogram showing the percentage of total head area occupied by a particular range of buoyancy flux fraction for the rough-surface flow described in Figure 62b.

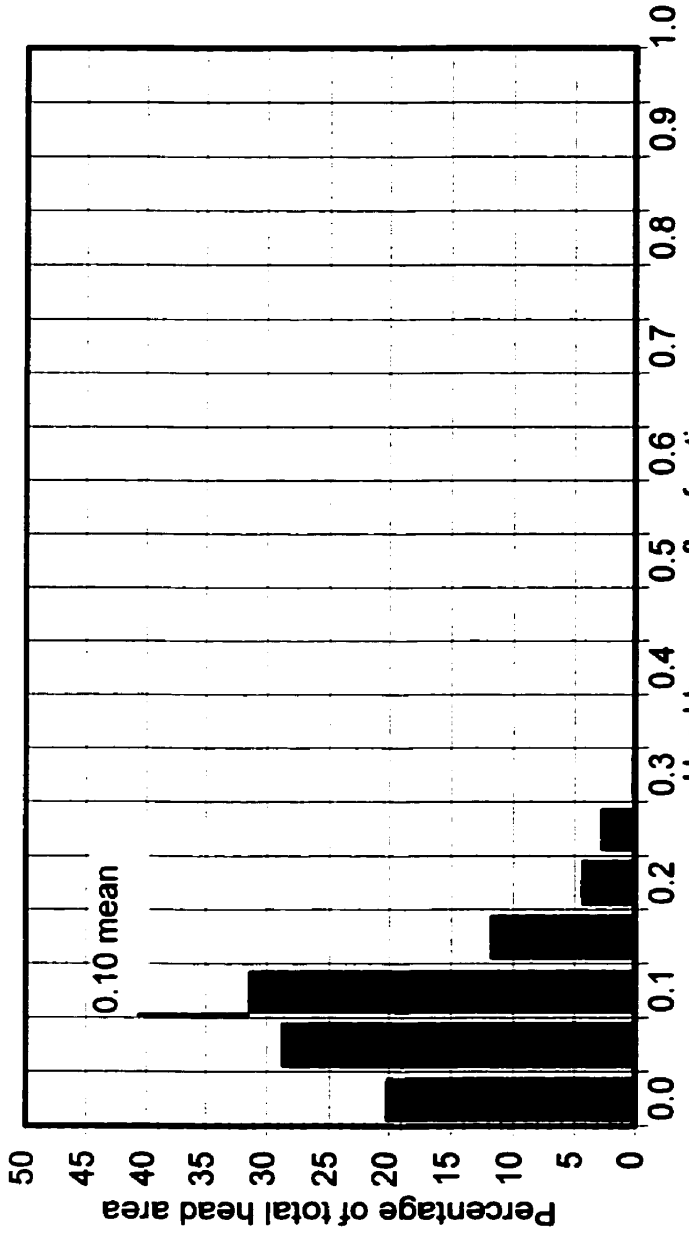

Figure 63c. Histogram showing the percentage of total head area occupied by a particular range of buoyancy flux fraction for the rough-surface flow described in Figure 62c.

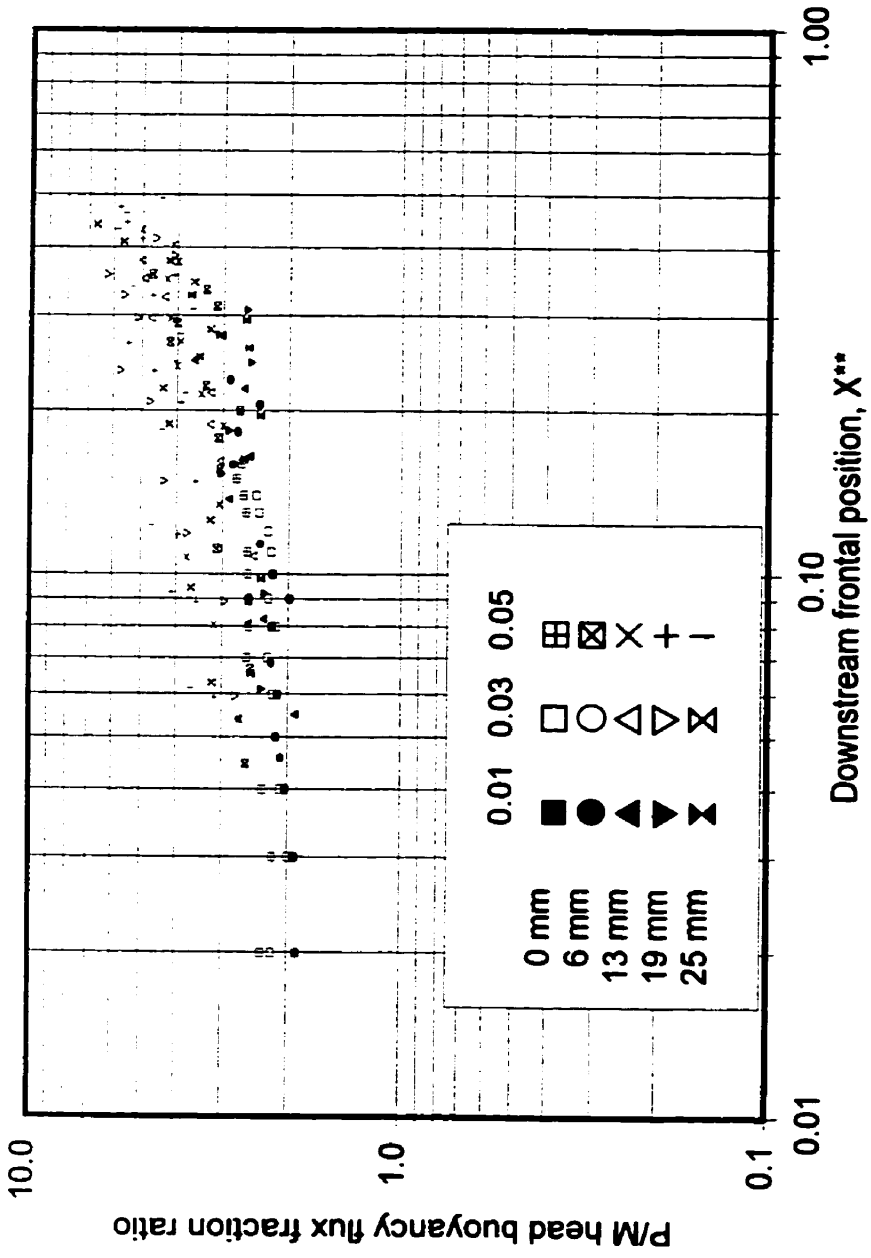

Figure 64. Variation of the peak/mean, P/M, ratio of the gravity current head buoyancy flux fraction with downstream frontal position for all gravity current flows over the range of surface roughness scales and fluid density excesses used.

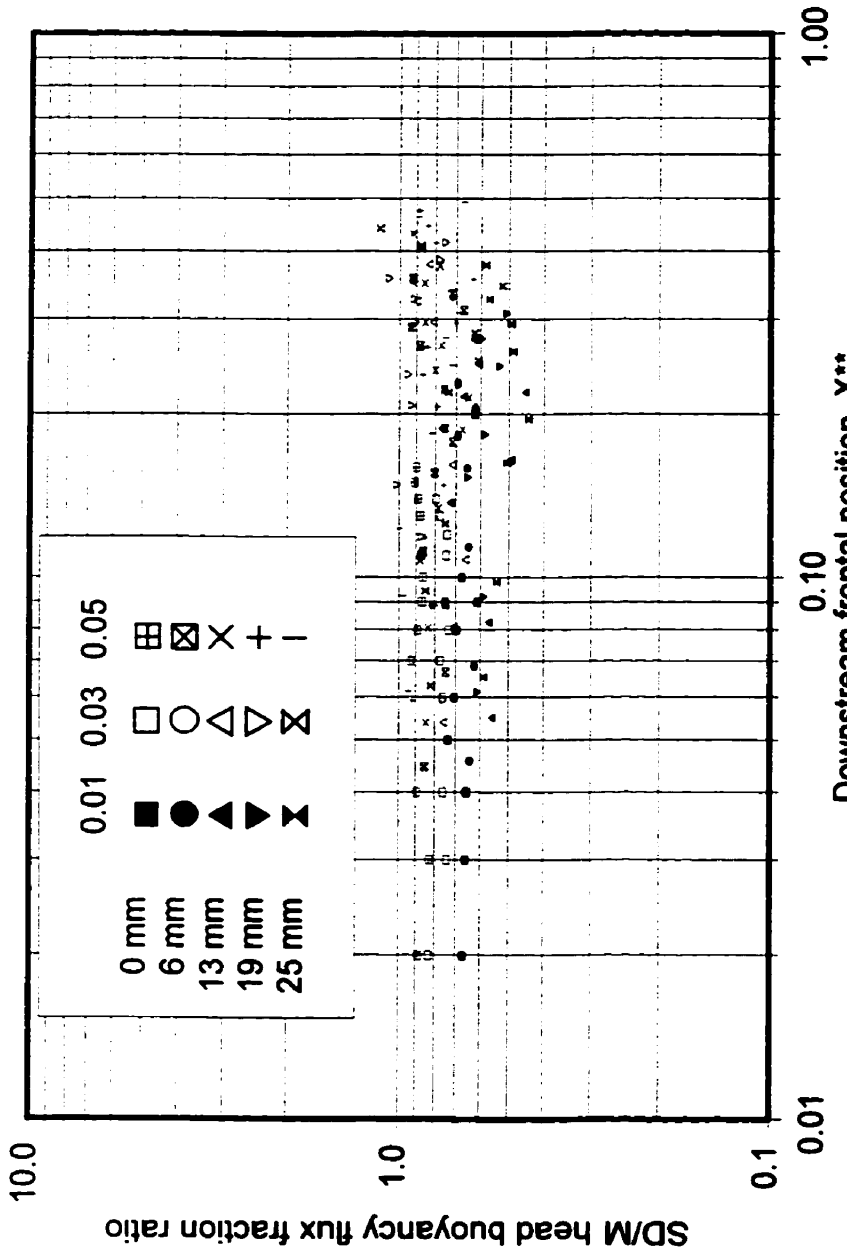

Figure 65. Variation of the standard deviation/mean, SD/M, ratio of the gravity current head buoyancy flux fraction with downstream frontal position for all gravity current flows over the range of surface roughness scales and fluid density excesses used.

CHAPTER 7

CONCLUSIONS

7.1 Modelling, Visualization and Analysis Techniques

The techniques of salt-water modelling, laser-induced fluorescence and digital image processing were successfully used to model, visualize and analyze small-scale, two-dimensional, continuous source gravity current flows. It has been shown that the facility and experimental techniques developed can successfully provide full-field, two-dimensional, planar images of the flow structure for qualitative and quantitative study. These images can be used to study the downstream spread rate of the current and the mixing associated with the flow.

The following three specific conclusions are given with respect to proper quantification of results.

1) In agreement with Walker (1987), it is concluded that fluorescein sodium is a suitable fluorescent dye to use in the LIF visualization technique. For the experimental conditions described in the present work, Figures 9, 10 and 11 confirm that the emission signal strength, for dye concentrations up to 5×10^{-8} mol/l, is linearly proportional to both the dye concentration and the excitation signal strength and that attenuation of the excitation signal is negligible.

2) Through experiment, it was concluded that it is necessary to use working fluids buffered to a pH above 8 in order to maximize the emission signal strength. In

addition to this, aged dye solutions should be used to minimize the effects of oxidation and photo-decomposition which act to reduce the emission signal strength of the dye.

3) As the emission signal strength is typically very low when the above conditions are satisfied, it is concluded that certain procedures are required to successfully quantify it. These are: 1) experiments should be performed in a dark room to eliminate background light noise, 2) appropriate colour glass filters should be used to isolate only the emission signal wavelength for sampling, 3) image intensification is required to increase the signal to measurable levels and 4) a running time-average of approximately one second should be used for image frame grabbing to minimize the noise in the measured signal.

7.2 Smooth-Surface Flows

In general, the experimental methods used show that the smooth-surface gravity current flows generated in this study behave consistently with the accepted theory and observations in terms of structure, flow dynamics and mixing behaviour for the range of fluid density excesses investigated. The results of these smooth-surface flow tests, thus, validate the modelling, visualization and analysis techniques developed and provide valuable reference cases against which the rough-surface flow results have been compared.

The following three specific conclusions are given for the downstream spread rates and the downstream mixing behaviour observed in the smooth-surface flows.

1) Several definitions of the densimetric Froude number have been reported in the literature and good agreement with each has been observed. For modelling the downstream spread rate in the inertial-buoyant regime, however, it is concluded that the appropriate definition should be based on the normalized downstream frontal velocity, u_2^*, as defined by Equation 5-6 and plotted in Figure 22. This form has the advantage of being based on the measured frontal velocity, the controlled volumetric injection rate and the source fluid density excess. It is not a function of the geometry of the gravity current head.

2) The downstream dilution of the gravity current head by the lighter ambient fluid is relatively small for smooth-surface flows as indicated in Figure 28. This is consistent with the relatively low shear stress developed at the solid boundary and the large downstream extent of the inertial-buoyant regime. Accordingly, it is concluded that the head buoyancy flux fraction is conserved during the downstream inertial-buoyant flow and that spread rate models, for this regime, appropriately assume that there is no mixing between the current and the ambient fluids.

3) The buoyancy flux conservation and non-mixing assumptions are reasonable only in terms of mean conditions. Within the gravity current head, however, local values of buoyancy flux fraction can reach levels two to three times greater than the overall mean value for the head. The spatial standard deviation of the buoyancy flux fraction can be 65-95% of the mean value for the head. It is not possible to

predict when and where these local conditions occur. The present work, however, provides valuable statistical information about the fluctuations within the structure.

7.3 Rough-Surface Flows

In general, the smooth-surface theory and observations that were reported in Chapter 5 do not extend to the gravity current flows over the beam-roughened surfaces studied in this research. The results and observations of the rough-surface tests performed over a range of surface roughness and source fluid density excess indicate that there are two rough-surface interactions that lead to lower frontal velocities, greater flow deceleration and increased head dilution than would be observed in a corresponding smooth-surface flow.

The first interaction is the mechanism by which the lighter ambient fluid, trapped in the spaces between the roughness elements, is entrained into the head as it is overrun. The second interaction is due to the increased shear stress and friction at the lower boundary that results from the increased surface roughness scale.

The following specific conclusions are drawn with respect to the results of the rough-surface flow tests.

1) Rougher surfaces tend to decrease the inertial-buoyant frontal advance velocity of the flow, give rise to gravity currents that are dominated by viscous effects much earlier in their dispersion and, once viscous effects become significant, decelerate the flows at a rate much greater than that observed for smooth-surface flows.

2) The video record and images for rough-surface flows indicate that the gravity current structure tends to flow along the top of the roughness element array as indicated in Figures 40 and 41. Fluid exchange occurs between the dense head fluid and the buoyantly unstable, lighter ambient fluid in the roughness element spaces. Circulation patterns are generated within the roughness element spaces as dense head fluid is sheared off by the roughness elements as they are passed over.

3) Using an effective viscosity approach to account for the surface roughness, the existing smooth-surface spread rate theory was modified to develop a rough-surface spread rate model. The new inertial-buoyant and viscous-buoyant equations, Equations 6-16 and 6-17 are applicable for both smooth and rough surface flows. Normalized using this new model, the rough-surface spread rate results are consistent with those for the corresponding smooth-surface flows.

4) Since the gravity current tends to flow along the top of the roughness element array, the parameters (h_2-h_R) and $(H'-h_R)$ are used to quantify head and layer heights, respectively. Further, it is more appropriate to normalize these vertical heights with d'_{REF} rather than with d_R which is based on the effective rough-surface Reynolds number. The normalized rough-surface head height increases by approximately 30% above the value for the smooth-surface flows. The normalized rough-surface layer height agrees very well with that for the smooth-surface flows.

5) The rough-surface buoyancy flux fraction of the gravity current head decreases with downstream position in accordance with a power law. This downstream

dilution, however, increases significantly with increased source fluid density excess and surface roughness scale. An appropriate mixing model is required to account for these density and roughness effects.

6) As shown in Figure 60, a rough-surface mixing ratio was defined to quantify the downstream dilution rate for the rough-surface flows in terms of the dilution rate observed for the smooth-surface flows. The downstream dilution rate increases with increasing roughness scale. This effect is more significant for the heavier flows. It is concluded that this fluid density excess dependency increases as the surface roughness increases and can be attributed to the greater tendency for the heavier flows to fill the spaces between roughness elements as they are passed over.

7) As with the smooth-surface flows, the mean head buoyancy flux fraction is not a good predictor of local values for the rough-surface flows. Peak values as high as five times the mean head value are possible since the rough-surface mean head buoyancy flux fraction is typically much lower than that for the corresponding smooth-surface flow. The spatial standard deviation is consistent with that reported for the smooth-surface flows.

CHAPTER 8

FUTURE WORK

8.1 Visualization and Analysis Techniques

The work carried out under the present research study has shown that the visualization and analysis techniques developed work well. Future work, however, in the following areas would make valuable contributions to the improvement and refinement of these techniques for future research.

1) Improved uniformity in the vertically collimated excitation laser sheet could be achieved by using a higher quality, optic grade, plano-cylindrical, collimating lens. The lens used in the present research was custom made from acrylic sheet.

2) During the late stages of the present study, an attempt was made to develop a gravity current tracking system that would operate without user interaction. The intention was to use real time image processing to scan the image and locate the leading edge of the gravity current head to provide feedback to adjust the tracking system speed control. Unfortunately, this was never completed. This type of control would provide more consistent and smoother tracking while automating the process.

3) There have been considerable improvements in the processing speed of computers and the availability of image processing and enhancement software since the present experimental work was completed. Using real-time image

processing and image grabbing directly to digital memory would eliminate the need for the VHS recording step. This would eliminate considerable noise from the data and reduce the processing stage from the present two-step procedure to a single one-step on-line procedure. Essentially, then, all image processing could be done in real-time.

4) Given the potential for real-time processing, a complete statistical analysis of many subsequent images could be performed to provide valuable information about the fluctuations and variability of the gravity current head buoyancy flux fraction. This would provide a more complete picture of the dilution mechanisms.

8.2 Rough-Surface Flow Experiments

Future work in the following areas would make valuable contributions to the further understanding of the mixing mechanisms in the rough-surface gravity current flows studied in the present research.

1) It was shown that the gravity current structure tends to flow along the top of the roughness element array. Significant dilution of the gravity current head, then, results from the fluid exchange between the heavier head fluid and the lighter fluid in the roughness element spaces. A series of experiments could be performed in which the roughness element spaces are pre-filled with the same source fluid used to generate the head. This would eliminate the gravitationally unstable fluid exchange at the roughness element level and should produce a gravity current flow that approaches the smooth-surface flow.

2) As described in Chapter 6, there was virtually no distinction between the downstream dilution results for the 0.03 and 0.05 fluid density excess cases for each surface roughness scale used. In contrast, there was a significant difference between the 0.01 fluid density excess tests and the 0.03 and 0.05 fluid density excess tests. Accordingly, a series of experiments could be performed to investigate the dependency on the fluid density excess for values from 0.03 down to less than 0.01.

3) Perform experiments to evaluate the rough-surface flow behaviour in terms of the "k"- and "d"-type flows described by Perry et al. (1969) so that an appropriate application of the "law of the wall" can be made.

4) The development of an appropriate downstream mixing model is required to more completely normalize the effects of the surface roughness scale and the source fluid density excess.

REFERENCES

Ayrault, M., Simoens, S. and Mejean, P., 1993, "Effects of a two-dimensional obstacle on the dispersion of dense gas releases", Symposium on Experimental and Numerical Flow Visualization, ASME Winter Annual Meeting, New Orleans, Louisiana, November 28 - December 3, 1993, FED-Vol. 172, pp. 233-239.

Benjamin, T.B., 1968, "Gravity currents and related phenomena", Journal of Fluid Mechanics, Vol. 31, Part 2, pp. 209-248.

Blackmore, D.R., Herman, M.N. and Woodward, J.L., 1982, "Heavy gas dispersion models", Journal of Hazardous Materials, Vol. 6, pp. 107-128.

Britter, R.E., 1979, "The spread of a negatively buoyant cloud in a calm environment", Atmospheric Environment, Vol. 13, pp. 1241-1247.

Britter, R.E. and Griffiths, R.F., 1982, "The role of dense gases in the assessment of industrial hazards", Journal of Hazardous Materials, Vol. 6, pp. 3-12.

Britter, R.E. and Snyder, W.H., 1988, "Fluid modelling of dense gas dispersion over a ramp", Journal of Hazardous Materials, Vol. 18, pp. 37-67.

Brungart, T.A., Petrie, H.L., Harbison, W.L. and Merkle, C.L., 1991, "A fluorescence technique for measurement of slot injected fluid concentration profiles in a turbulent boundary layer", Experiments in Fluids, Vol. 11, pp. 9-16.

Chan, W.R., Zukowski, E.E. and Kubota, T., 1993, "Experimental and numerical studies on two-dimensional gravity currents in a horizontal channel", Report. No. NIST-GCR-93-630, Center for Fire Research, National Institute of Standards and Technology, U.S. Department of Commerce, Gaithersburg, Maryland, 238 p.

Chen, J.C., 1980, "Studies on gravitational spreading currents", Report No. KH-R-40, W.M. Keck Laboratory of Hydraulics and Water Resources, Division of Engineering and Applied Science, California Institute of Technology, Pasadena, California, 436 p.

Chobotov, M.V., Zukoski, E.E. Kubota, T., 1987, "Gravity currents with heat transfer effects", Report No. NBS-GRC-87-522, Center for Fire Research, National Bureau of Standards, U.S. Department of Commerce, Gaithersburg, Maryland, 158 p.

Coleman, H.W., Hodge, B.K. and Taylor, R.P., 1984, "A re-evaluation of Schlichting's surface roughness experiment", Journal of Fluids Engineering, Vol. 106, pp. 60-65.

Daugherty, R.L., Franzini, J.B. and Finnemore, E.J., 1985, Fluid mechanics with engineering applications, Eighth edition, McGraw-Hill, Inc., New York, New York, 598 p.

Davies, M.E. and Singh, S., 1985, "The Phase II trials: A data set on the effects of obstructions", Journal of Hazardous Materials, Vol. 11, pp. 301-323.

Didden, N. and Maxworthy, T., 1982, "The viscous spreading of plane and axisymmetric gravity currents", Journal of Fluid Mechanics, Vol. 121, pp. 27-42.

Donne, M.D. and Meyer, L., 1977, "Turbulent convective heat transfer from rough surfaces with two-dimensional rectangular ribs", International Journal of Heat and Mass Transfer, Vol. 20, pp. 583-620.

Duijm, N.J., Jones, S.J., Martin, D. and Webber, D.M., 1995, "The effect of obstacles on dense gas clouds", Loss Prevention and Safety Promotion in the Process Industries, Volume 1, Proceedings of the 8th International Symposium, Antwerp, Belgium, June 6-9, 1995, Edited by Mewis, J.J., Pasman, H.J. and De Rademaeker, E.E., pp. 185-196.

Ellison, T.H. and Turner, J.S., 1959, "Turbulent entrainment in stratified flows", Journal of Fluid Mechanics, Vol. 6, pp. 423-448.

Ermak, D.L. and Chan, S.T., 1985, "A study of heavy gas effects on the atmospheric dispersion of dense gases", Report No. UCRL-92494, Lawrence Livermore National Laboratory.

Fauske, H.K. and Epstein, M., 1989, "Hazardous vapor clouds: Release type, aerosol formation and mitigation", Sixth International Symposium on Loss Prevention and Safety Promotion in the Process Industries, European Federation of Chemical Engineering, Oslo, Norway, June 19-22, 1989, Paper No. 69, Vol. II, 15 p.

Gad-el-Hak, M., 1988, "Visualization techniques for unsteady flows: An overview", Journal of Fluids Engineering, Vol. 110, pp. 231-243.

Gröbelbauer, H.P., Fanneløp, T.K. and Britter, R.E., 1993, "The propagation of intrusion fronts of high density ratios", Journal of Fluid Mechanics, Vol. 250, pp. 669-687.

Guilbault, G.G., 1973, Practical fluorescence: Theory, methods and techniques, Marcel Dekker, Inc., New York, New York, 664 p.

Guldemond, C.P., 1986, "The behaviour of denser than air ammonia in the presence of obstacles - Wind tunnel experiments", Plant/Operations Progress, Vol. 5, No. 2.

Havens, J.A., Spicer, T.O., Walker, H. and Williams, T., 1995, "Validation of mathematical models using wind-tunnel data sets for dense gas dispersion in the presence of obstacles", Loss Prevention and Safety Promotion in the Process Industries, Volume 1, Proceedings of the 8th International Symposium, Antwerp, Belgium, June 6-9, 1995, Edited by Mewis, J.J., Pasman, H.J. and De Rademaeker, E.E., pp. 171-184.

Havens, J.A. and Spicer, T.O., 1985, "Development of an atmospheric dispersion model for heavier-than-air gas mixtures", U.S. Coast Guard Report No. CG-D-22-85.

Hesselink, L., 1988, "Digital image processing in flow visualization", Annual Review of Fluid Mechanics, Vol. 20, pp. 421-485.

Hoot, T.G. and Meroney, R.N., 1974, "The behaviour of negatively buoyant stack gases", Proceedings of the 67th Annual Meeting of APCA, Denver, CO, Paper 74-210, 20 p.

Houcine, I., Vivier, H., Plasari, R. and Villermaux, J., 1996, "Planar laser induced fluorescence technique for measurements of concentration fields in continuous stirred tank reactors", Experiments in Fluids, Vol. 22, pp. 95-102.

Huppert, H.E., 1982, "The propagation of two-dimensional and axisymmetric viscous gravity currents over a rigid horizontal surface", Journal of Fluid Mechanics, Vol. 121, pp. 43-58.

Huppert, H.E. and Simpson, J.E., 1980, "The slumping of gravity currents", Journal of Fluid Mechanics, Vol. 99, Part 4, pp. 785-799.

Karasso, P.S. and Mungal, M.G., 1997, "PLIF measurements in aqueous flows using the ND : YAG laser", Experiments in Fluids, Vol. 23, pp 382-387.

Keulegan, G.H., 1949, "Interfacial instability and mixing in stratified flows", Journal of Research of the National Bureau of Standards, U.S. Department of Commerce, Gaithersburg, Maryland, Vol. 43, 487 p.

Keulegan, G.H., 1957, "An experimental study of the motion of saline water from locks into fresh water channels", NBS Report No. 5168, National Bureau of Standards, U.S. Department of Commerce, Gaithersburg, Maryland, 76 p.

Keulegan, G.H., 1958, "The motion of saline fronts in still water", Report No. 5831, National Bureau of Standards, U.S. Department of Commerce, Gaithersburg, Maryland, 66 p.

Koochesfahani, M.M. and Dimotakis, P.E., 1985, "Laser-induced fluorescence measurements of mixed fluid concentration in a liquid plane shear layer", American Institute of Aeronautics and Astronautics Journal, Vol. 23, No. 11, pp. 1700-1707.

Krogstad, P.A. and Pettersen, R.M., 1986, "Wind-tunnel modelling of a release of a heavy gas near a building", Atmospheric Environment, Vol. 20, No. 5, pp. 867-878.

Lane-Serff, G.F., Beal, L.M. and Hadfield, T.D., 1995, "Gravity current flows over obstacles", Journal of Fluid Mechanics, Vol. 292, pp.39-53.

Lenoir, E.M. and Davenport, J.A., 1992, "A survey of vapor cloud explosions: Second update", 26th Annual Loss Prevention Symposium, American Institute of Chemical Engineers, New Orleans, Louisiana, March 29 - April 2, Paper No. 74d, 29 p.

McQuaid, J., 1982, "Future direction of dense-gas dispersion research", Journal of Hazardous Materials, Vol. 6, pp. 231-247.

Meroney, R.N., 1982, "Wind-tunnel experiments on dense gas dispersion", Journal of Hazardous Materials, Vol. 6, pp. 85-106.

Meroney, R.N., 1985, "Guideline for fluid modelling of liquefied natural gas cloud dispersion: Instruction Guide", Vol. I and II, Report No. CER84-85RNM-50A.

Meroney, R.N., 1986, "Guideline for fluid modelling of liquefied natural gas cloud dispersion: Technical Support Document, Report No. CER84-85RNM-50B.

Middleton, G.V., 1966, "Experiments on density and turbidity currents: Motion of the head", Canadian Journal of Earth Science, Vol. 3, pp. 523-546.

Mills, A.F. and Hang, X., 1983, "On the skin friction coefficient for a fully rough flat plate", Journal of Fluids Engineering, Vol. 105, pp. 364-365.

Nash, J.D., Jirka, G.H. and Chen, D., 1995, "Large scale planar laser induced fluorescence in turbulent density-stratified flows", Experiments in Fluids, Vol. 19, pp. 297-304.

Neff, D.E. and Meroney, R.N., 1986, " LNG vapor barrier and obstacle evaluation: Wind tunnel and pre-field test results", Colorado State University, Ft. Collins, Colorado, Report No. CER86-87DEN-RNM8, 44 p.

Nikuradse, J., 1933, "Stromungsgesetze in rauhen Rohren", VDI Forshungsheft, No. 361. Translated as NACA TM, No. 1292 (1950).

Perry, A.E., Schofield, W.H. and Joubert, P.N., 1969, "Rough-wall turbulent boundary layers", Journal of Fluid Mechanics, Volume 37, Part 2, pp. 383-413.

Peters, W.D., Cogswell, S.R. and Venart, J.E.S., 1996, "Dense gas simulation flows over rough surfaces", Journal of Hazardous Materials, Vol. 46, pp.215-223.

Peters, W.D., Cogswell, S.R. and Venart, J.E.S., 1997, "Mixing in gravity current heads flowing over rough surfaces", Developments in Laser Techniques and Fluid Mechanics, Eds. R.J. Adrian et al., Springer, Berlin, Chapter III, pp. 325-339.

Peters, W.D. and Venart, J.E.S., 1992, "Experimental study of stack gas flows using laser-induced dye fluorescence", Sixth International Symposium on the Application of Laser Techniques to Fluid Mechanics, Lisbon, Portugal, July 20-23, Paper No. 31.3, pp. 31.3.1-31.3.4.

Petersen, R.L., 1987, "Surface roughness effects on heavier-than-air gas diffusion", American Petroleum Institute, Health and Environmental Sciences Department, Washington, D.C., API Publication No. 4459, 44 p.

Petersen, R.L., and Ratcliff, M.A., 1989, "Effect of homogeneous and heterogeneous surface roughness on heavier-than-air gas dispersion", American Petroleum Institute, Health and Environmental Sciences Department, Washington, D.C., API Publication No. 4491, 354 p.

Puttock, J.S., Blackmore, D.R., and Colenbrander, G.W., 1982, "Field experiments on dense gas dispersion", Journal of Hazardous Materials, Vol. 6, pp. 13-42.

Roberts, P.T., Puttock, J.S. and Blewitt, D.N., 1990, "Gravity spreading and surface roughness effects in the dispersion of dense gas plumes", American Institute of Chemical Engineers 1990 Health and Safety Symposium, Session IIB: Modelling of Aerosol Clouds, Orlando, Florida, March 18-22, 16 p.

Rottman, J.W., Simpson, J.E., Hunt, J.C.R. and Britter, R.E., 1985, "Unsteady gravity current flows over obstacles: Some observations and analysis related to the Phase II trials", Journal of Hazardous Materials, Vol. 11, pp. 325-340.

Schlichting, H., 1979, Boundary Layer Theory, McGraw-Hill, New York, NY, pp. 619.

Schmidt, W., 1911, "Zer mechanik der boen", Z. Meteorol, Vol. 28, pp. 355-362.

Shlien, D.J., 1988, "Instantaneous concentration field measurement technique from flow visualization photographs", Experiments in Fluids, Vol. 6, pp. 541-546.

Simpson, J.E., 1972, "Effects of the lower boundary on the head of a gravity current," Journal of Fluid Mechanics, Vol. 53, Part 4, pp. 759-768.

Simpson, J.E., 1986, "Mixing at the front of a gravity current", Acta Mechanica, Vol. 63, pp. 245-253.

Simpson, J.E., 1987, Gravity currents: In the environment and the laboratory, Ellis Horwood Limited, West Sussex, United Kingdom, 244 p.

Simpson, J.E., and Britter, R.E., 1979, "The dynamics of the head of a gravity current advancing over a horizontal surface", Journal of Fluid Mechanics, Vol. 94, Part 3, pp. 477-495.

Simpson, J.E., and Britter, R.E., 1980, "A laboratory model of an atmospheric mesofront", Quarterly Journal of the Royal Meteorological Society, Vol. 106, pp. 485-500.

Snyder, W.H., 1981, "Guidelines for fluid modelling of atmospheric diffusion", U.S. Environmental Protection Agency, Report EPA-600/8-81-009, 185 p.

Sollows, K.F., Venart, J.E.S., Dutcher, C.R., and Sousa, A.C.M., 1990, "Photobleaching flow visualization", Fifth International Symposium on the Application of Laser Techniques to Fluid Mechanics, Lisbon, Portugal, July 9-12, Paper No. 9.4.

Steckler, K.D., Baum, H.R., and Quintiere, J.G., 1986, "Salt water modeling of fire induced flows in multicompartment enclosures", Twenty-First Symposium (International) on Combustion, The Combustion Institute, pp. 143-149.

Sumathipala, U.K., Aydemir, N.U., Hadjisophocleous, G., Gray, R. and Venart, J.E.S., 1992, "Cargo responses in cylindrical shipboard tanks to practical fire exposures: Models and experiment", 1st European Thermal-Sciences and 3rd U.K. National Heat Transfer Conference, University of Birmingham, United Kingdom, September 16-18.

Turner, J.S., 1973, Buoyancy effects in fluids, Cambridge University Press, London, United Kingdom, 367 p.

van Cruyningen, I., Lozano, A. and Hanson, R.K., 1990, "Quantitative imaging of concentration by planar laser-induced fluorescence", Experiments in Fluids, Vol. 10, pp. 41-49.

Venart, J.E.S., Rutledge, G.A., Sumathipala, and Sollows, K., 1992, "To BLEVE or not to BLEVE: Anatomy of a boiling liquid expanding vapour explosion", American Institute of Chemical Engineers Loss Prevention, New Orleans, LA., March/April, 1992.

von Kármán, 1940, "The engineer grapples with nonlinear problems", Bulletin of the American Mathematical Society, Vol. 46, pp. 615-683.

Walker, D.A., 1987, "A fluorescence technique for measurement of concentration in mixing fluids", Journal of Physics, E, Scientific Instruments, Vol. 20, pp. 217-224.

Westblom, U. and Svanberg, S., 1985, "Imaging measurements of flow velocities using laser-induced fluorescence", Physica Scripta, Vol. 31, pp. 402-405.

Wilkinson, D.L. and Wood, I.R., 1972, "Some observations on the motion of the head of a density current", Journal of Hydraulic Research, Vol. 10, No. 3, pp. 305-324.

Wilson, D.J., 1991, "Accounting for peak concentrations in atmospheric dispersion for worst case hazard assessments", International Conference and Workshop on Modeling and Mitigating the Consequences of Accidental Releases of Hazardous Materials, American Institute of Chemical Engineers, New Orleans, Louisiana., May 20-24, pp. 385-401.

Winant, C.D. and Bratkovich, A., 1977, "Structure and mixing within the frontal region of a density current", 6th Australasian Hydraulics and Fluid Mechanics Conference, Adelaide, Australia, December 5-9, pp. 9-12.

Yih, C.S., 1965, Dynamics of nonhomogeneous fluids, MacMillan, 1965.

Yoda, M. and Fiedler, H.E., 1996, "The round jet in a uniform counterflow: flow visualization and mean concentration measurements", Experiments in Fluids, Vol. 21, pp. 427-436.

Zukoski, E.E. and Kubota, T., 1988, "Experimental study of environment and heat transfer in a room fire", Center for Fire Research, National Institute of Standards and Technology, U.S. Department of Commerce, Gaithersburg, Maryland, Report Number NIST-GCR-88-554, 26 p.